3 Thermodynamics and Phase Diagrams

Arthur D. Pelton, Centre de Recherche en Calcul Thermochimique (CRCT), École Polytechnique de Montréal, Montréal, Canada

3.1 Introduction

An understanding of phase diagrams is fundamental and essential to the study of materials science, and an understanding of thermodynamics is fundamental to an understanding of phase diagrams. Knowledge of the equilibrium state of a system under a given set of conditions is the starting point in the description of many phenomena and processes.

A phase diagram is a graphical representation of the values of the thermodynamic variables when equilibrium is established among the phases of a system. Materials scientists are most familiar with phase diagrams that involve temperature, T, and composition as variables. Examples are T-composition phase diagrams for binary systems such as **Figure 1** for the Fe–Mo system, isothermal phase diagram sections of ternary systems such as **Figure 2** for the Zn–Mg–Al system, and isoplethal (constant composition) sections of ternary and higher order systems such as **Figures 3**a and **4**.

However, many useful phase diagrams can be drawn that involve variables other than T and composition. The diagram in **Figure 5** shows the phases present at equilibrium in the Fe–Ni–O_2 system at 1200 °C as the equilibrium oxygen partial pressure (i.e. chemical potential) is varied. The x-axis of this diagram is the overall molar metal ratio in the system. The phase diagram in **Figure 6** shows the equilibrium phases present when an equimolar Fe–Cr alloy is equilibrated at 925 °C with a gas phase of varying O_2 and S_2 partial pressures. For systems at high pressure, P–T phase diagrams such as the diagram for the one-component Al_2SiO_5 system in **Figure 7**a show the fields of stability of the various allotropes. When the pressure in **Figure 7**a is replaced by the volume of the system as the y-axis, the "corresponding" V–T phase diagram of **Figure 7**b results. The enthalpy of the system can also be a variable in a phase diagram. In the phase diagram in **Figure 3**b, the y-axis of **Figure 3**a has been replaced by the molar enthalpy difference $(h_T - h_{25})$ between the system at 25 °C and a temperature T. This is the heat that must be supplied or removed to heat or cool the system adiabatically between 25 °C and T.

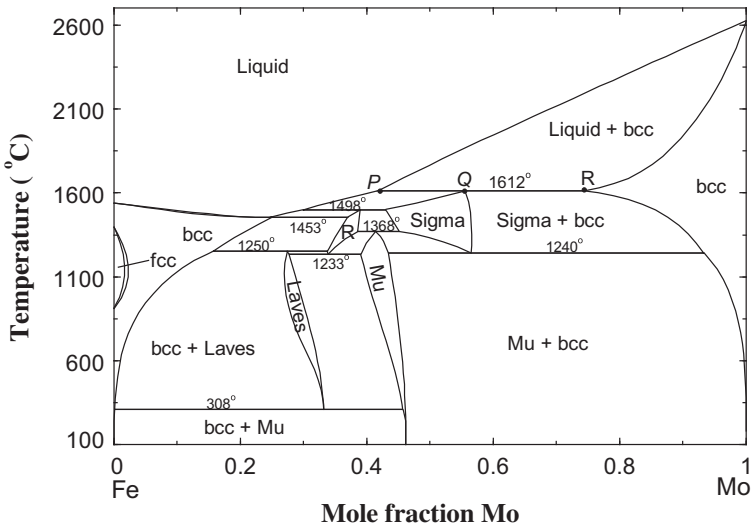

Figure 1 Temperature-composition phase diagram at $P = 1$ bar of the Fe–Mo system (see FactSage).

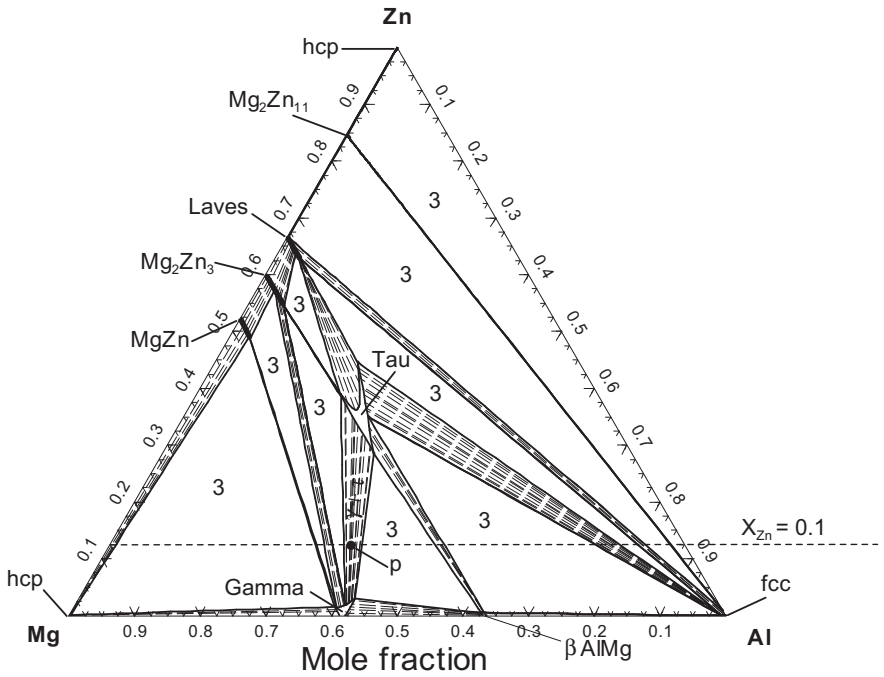

Figure 2 Isothermal section at 25 °C and $P = 1$ bar of the Zn–Mg–Al system (see FactSage).

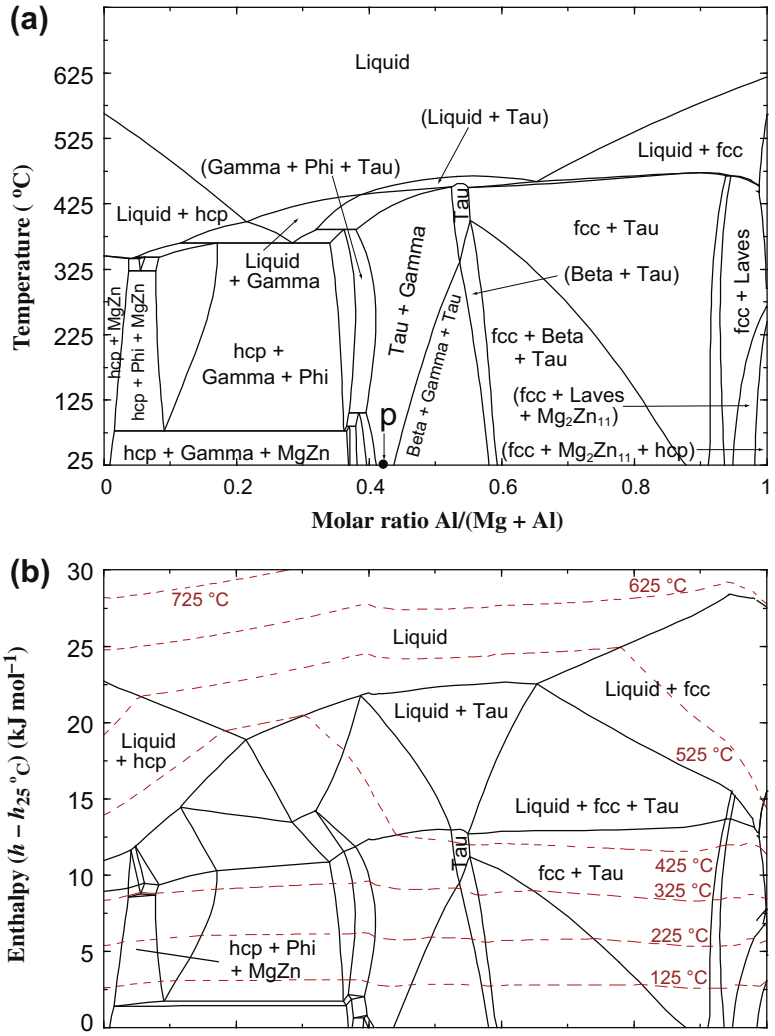

Figure 3 Isoplethal phase diagram section at $X_{Zn} = 0.1$ and $P = 1$ bar of the Zn–Mg–Al system. (a) Temperature *vs* composition; (b) Enthalpy *vs* composition (see FactSage). (For color version of this figure, the reader is referred to the online version of this book.)

The phase diagrams shown in **Figures 1–7** are only a small sampling of the many possible types of phase diagram sections. These diagrams and several other useful types of phase diagrams will be discussed in this chapter. Although these diagrams appear to have very different geometries, it will be shown that actually they all obey exactly the same geometrical rules.

The theme of this chapter is the relationship between phase diagrams and thermodynamics. To understand phase diagrams properly, it has always been necessary to understand their thermodynamic basis. However, in recent years, the relationship between thermodynamics and phase diagrams has taken on a new and important practical dimension. With the development of large evaluated databases

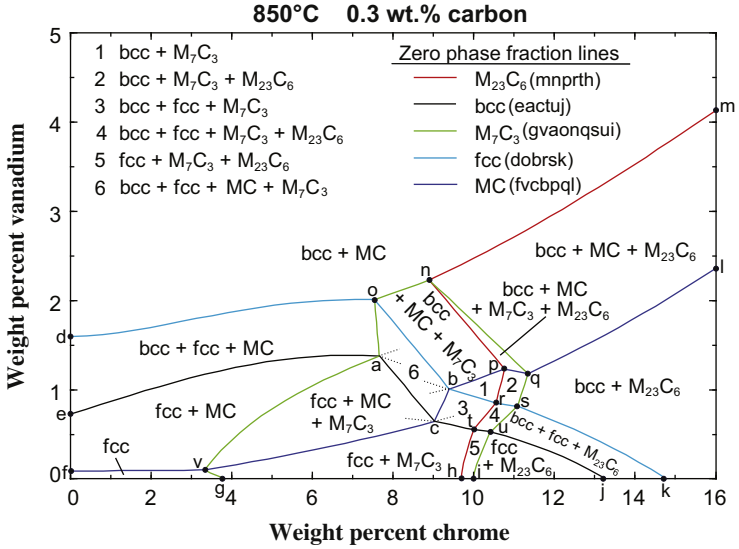

Figure 4 Phase diagram section of the Fe–Cr–V–C system at 850 °C, 0.3 wt.% C and $P = 1$ bar (see FactSage; SGTE). (For color version of this figure, the reader is referred to the online version of this book.)

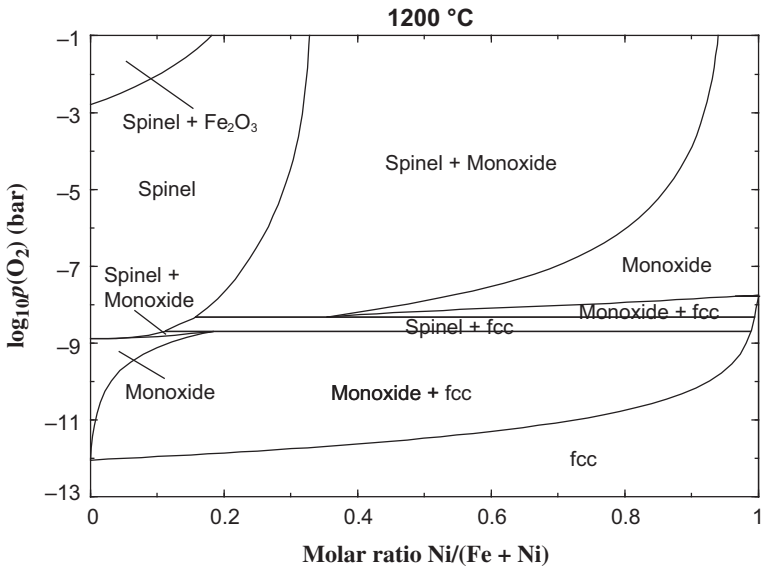

Figure 5 Phase diagram of the Fe–Ni–O_2 system at 1200 °C showing equilibrium oxygen pressure *vs* overall metal ratio (see FactSage).

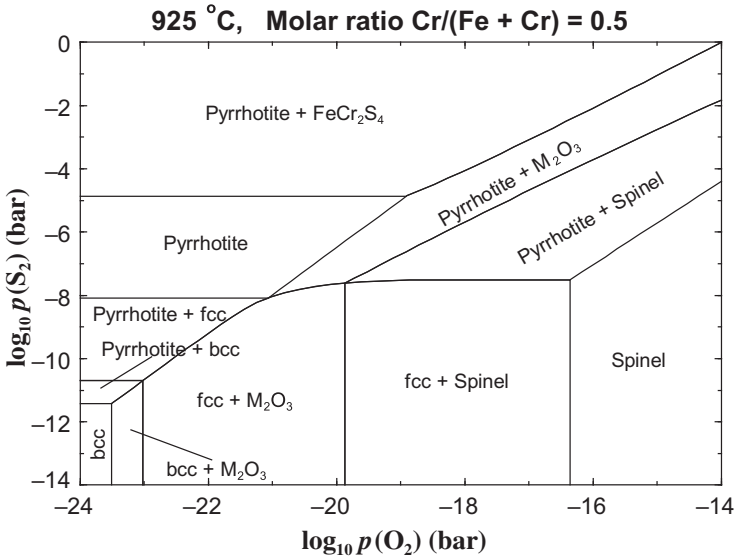

Figure 6 Phase diagram of the Fe–Cr–S_2–O_2 system at 925 °C showing equilibrium S_2 and O_2 partial pressures at constant molar ratio Cr/(Cr + Fe) = 0.5 (see FactSage).

of the thermodynamic properties of thousands of compounds and solutions, and of software to calculate the conditions for chemical equilibrium (by minimizing the Gibbs energy), it is possible to rapidly calculate and plot desired phase diagram sections of multicomponent systems. Most of the phase diagrams shown in this chapter were calculated thermodynamically with the FactSage software and databases (see FactSage in the list of websites at the end of this chapter).

Several large integrated thermodynamic database computing systems have been developed in recent years (see list of websites at the end of this chapter). The databases of these systems have been prepared by the following procedure. For every compound and solution phase of a system, an appropriate model is first developed giving the thermodynamic properties as functions of *T*, *P* and composition. Next, all available thermodynamic and phase equilibrium data from the literature for the entire system are simultaneously optimized to obtain one set of critically evaluated, self-consistent parameters of the models for all phases in two-component, three-component and, if data are available, higher order subsystems. Finally, the models are used to estimate the properties of multicomponent solutions from the databases of parameters of the lower order subsystems. The Gibbs energy minimization software then accesses the databases and, for given sets of conditions (*T*, *P*, composition…), calculates the compositions and amounts of all phases at equilibrium. By calculating the equilibrium state as *T*, composition, *P*, etc. are varied systematically, the software generates the phase diagram. As mentioned above, although the phase diagram sections shown in **Figures 1–7** are seemingly quite different topologically, they actually obey the same simple rules of construction and hence, can all be calculated by the same algorithm.

Section 3.2 provides a review of the fundamentals of thermodynamics as required for the interpretation and calculation of phase diagrams of all types. In Section 3.3, the Gibbs Phase Rule is developed in a general form suitable for the understanding of phase diagrams involving a wide range of variables including chemical potentials, enthalpy, volume, etc. Section 3.4 begins with a review of the

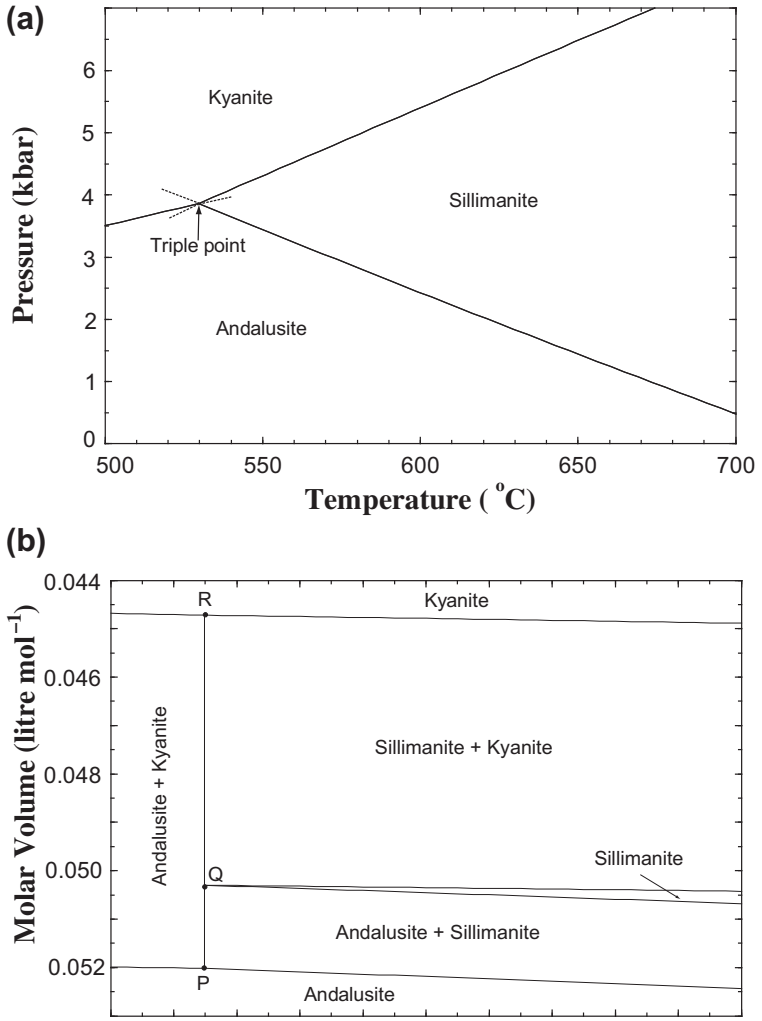

Figure 7 (a) P–T and (b) V–T phase diagrams of Al_2SiO_5 (see FactSage).

thermodynamics of solutions and continues with a discussion of the thermodynamic origin of binary T-composition phase diagrams, presented in the classical manner involving common tangents to curves of Gibbs energy. A thorough discussion of all features of T-composition phase diagrams of binary systems is presented in Section 3.5, with particular stress on the relationship between the phase diagram and the thermodynamic properties of the phases. A similar discussion of T-composition phase diagrams of ternary systems is given in Section 3.6. Isothermal and isoplethal sections as well as polythermal projections are discussed.

Readers conversant in binary and ternary T-composition diagrams may wish to skip Sections 3.4–3.6 and pass directly to Section 3.7, where the geometry of general phase diagram sections is developed. In this section, the following are presented: the general rules of construction of phase diagram sections; the

proper choice of axis variables and constants required to give a single-valued phase diagram section with each point of the diagram representing a unique equilibrium state; and a general algorithm for calculating all such phase diagram sections.

Section 3.8 outlines the techniques used to develop large thermodynamic databases through evaluation and modeling. Section 3.9 treats the calculation of equilibrium and nonequilibrium cooling paths of multicomponent systems. In Section 3.10, order/disorder transitions and their representation on phase diagrams are discussed.

3.2 Thermodynamics

This section is intended to provide a review of the fundamentals of thermodynamics as required for the interpretation and calculation of phase diagrams. The development of the thermodynamics of phase diagrams will be continued in succeeding sections.

3.2.1 The First and Second Laws of Thermodynamics

If the thermodynamic *system* under consideration is permitted to exchange both energy and mass with its *surroundings*, the system is said to be *open*. If energy but not mass may be exchanged, the system is said to be *closed*. The state of a system is defined by in*tensive properties*, such as temperature and pressure, which are independent of the mass of the system, and by *extensive properties*, such as volume and internal energy, which vary directly as the mass of the system.

3.2.1.1 Nomenclature

Extensive thermodynamic properties will be represented by upper-case symbols. For example, $G =$ Gibbs energy in joules (J). Molar properties will be represented by lower-case symbols. For example, $g = G/n =$ molar Gibbs energy in joules per mole (J mol^{-1}), where n is the total number of moles in the system.

3.2.1.2 The First Law

The *internal energy* of a system, U, is the total thermal and chemical bond energy stored in the system. It is an extensive state property.

Consider a closed system undergoing a change of state that involves an exchange of heat, dQ, and work, dW, with its surroundings. Since energy must be conserved:

$$dU_n = dQ + dW \tag{1}$$

This is the First Law. The convention is adopted whereby energy passing from the surroundings to the system is positive. The subscript on dU_n indicates that the system is closed (constant number of moles.)

It must be stressed that dQ and dW are not changes in state properties. For a system passing from a given initial state to a given final state, dU_n is independent of the process path since it is the change of a state property; however dQ and dW are, in general, path-dependent.

3.2.1.3 The Second Law

For a rigorous and complete development of the Second Law, the reader is referred to standard texts on thermodynamics. The *entropy* of a system, S, is an extensive state property which is given by Boltzmann's equation as:

$$S = k_B \ln t \tag{2}$$

where k_B is the Boltzmann's constant and t is the multiplicity of the system. Somewhat loosely, t is the number of possible equivalent microstates in a macrostate, that is, the number of quantum states of the system that are accessible under the applicable conditions of energy, volume, etc. For example, for a system that can be described by a set of single-particle energy levels, t is the number of ways of distributing the particles over the energy levels, keeping the total internal energy constant. At low temperatures, most of the particles will be in or near the ground state. Hence, t and S will be small. As the temperature, and hence, U, increases, more energy levels become occupied. Consequently, t and S increase. For solutions, an additional contribution to t arises from the number of different possible ways of distributing the atoms or molecules over the lattice or quasilattice sites (Section 3.4.1.5). Again somewhat loosely, S can be said to be a measure of the disorder of a system.

During any spontaneous process, the total entropy of the universe will increase for the simple reason that disorder is more probable than order. That is, for any spontaneous process,

$$dS_{total} = (dS + dS_{surr}) \geq 0 \tag{3}$$

where dS and dS_{surr} are the entropy changes of the system and surroundings, respectively. The existence of a state property S, which satisfies Eqn 3 is the essence of the Second Law.

Equation 3 is a necessary condition for a process to occur. However, even if Eqn 3 is satisfied, the process may not actually be observed if there are kinetic barriers to its occurrence. That is, the Second Law says nothing about the rate of a process, which can vary from extremely rapid to infinitely slow.

It should be noted that the entropy change of the system, dS, can be negative for a spontaneous process as long as the sum $(dS + dS_{surr})$ is positive. For example, during the solidification of a liquid, the entropy change of the system is negative in going from the liquid to the more ordered solid state. Nevertheless, a liquid below its melting point will freeze spontaneously because the entropy change of the surroundings is sufficiently positive due to the transfer of heat from the system to the surroundings. It should also be stressed that in passing from a given initial state to a given final state, the entropy change of the system dS is independent of the process path since it is the change of a state property. However, dS_{surr} is path-dependent.

3.2.1.4 The Fundamental Equation of Thermodynamics

Consider an open system at equilibrium with its surroundings and at internal equilibrium. That is, no spontaneous irreversible processes are taking place. Suppose that a change of state occurs in which S, V (volume) and n_i (number of moles of component i in the system) change by dS, dV and dn_i. Such a change of state occurring at equilibrium is called a *reversible* process, and the corresponding heat and work terms are dQ_{rev} and dW_{rev}. We may then write

$$dU = (\partial U/\partial S)_{v,n}\, dS + (\partial U/\partial V)_{s,n} dV + \sum \mu_i dn_i \tag{4}$$

where

$$\mu_i = (\partial U/\partial n_i)_{s,v,n_{j\neq i}} \tag{5}$$

μ_i is the chemical potential of component i which will be discussed in Section 3.2.7.

The absolute temperature is given as

$$T = (\partial U/\partial S)_{v,n} \tag{6}$$

We expect that temperature should be defined such that heat flows spontaneously from high to low T. To show that T as given by Eqn 6 is, in fact, such a thermal potential, consider two closed systems, isolated from their surroundings but in thermal contact with each other, exchanging only heat at constant volume. Let the temperatures of the systems be T_1 and T_2 and let $T_1 > T_2$. Suppose that heat flows from system 1 to system 2. Then $dU_2 = -dU_1 > 0$. Therefore, from Eqn 6,

$$dS = dS_1 + dS_2 = dU_1/T_1 + dU_2/T_2 > 0 \tag{7}$$

That is, the flow of heat from high to low temperature results in an increase in total entropy and hence, from the Second Law, is spontaneous.

The second term in Eqn 4 is clearly $(-P\,dV)$, the work of reversible expansion. From Eqn 6, the first term in Eqn 4 is equal to $T\,dS$, and this is then the reversible heat:

$$T\,dS = dQ_{rev} \tag{8}$$

That is, in the particular case of a process that occurs reversibly, (dQ_{rev}/T) is path-independent since it is equal to the change of a state property dS. Equation 8 is actually the definition of entropy in the classical development of the Second Law.

Equation 4 may now be written as

$$dU = T\,dS - P\,dV + \sum \mu_i\ dn_i \tag{9}$$

Equation 9, which results from combining the First and Second Laws, is called the *fundamental equation* of thermodynamics. We have assumed that the only work term is the reversible work of expansion (sometimes called "PV work"). In general, in this chapter, this will be the case. If other types of work occur, then non-PV terms, $dW_{rev(non\text{-}PV)}$, must be added to Eqn 9. For example, if the process is occurring in a galvanic cell, then $dW_{rev(non\text{-}PV)}$ is the reversible electrical work in the external circuit. Equation 9 can thus be written more generally as:

$$dU = T\,dS - P\,dV + \sum \mu_i\ dn_i + dW_{rev(non-PV)} \tag{10}$$

3.2.2 Enthalpy

Enthalpy, H, is an extensive state property defined as:

$$H = U + PV \tag{11}$$

Consider a closed system undergoing a change of state, which may involve irreversible processes (such as chemical reactions). Although the overall process may be irreversible, we shall assume that any work of expansion is approximately reversible (that is, the external and internal pressures are equal) and that there is no work other than work of expansion. Then, from Eqn 1:

$$\mathrm{d}U_{\mathrm{n}} = \mathrm{d}Q - P\,\mathrm{d}V \tag{12}$$

From Eqns 11 and 12, it follows that:

$$\mathrm{d}H_{\mathrm{n}} = \mathrm{d}Q + V\,\mathrm{d}P \tag{13}$$

Furthermore, if the pressure remains constant throughout the process, then

$$\mathrm{d}H_{\mathrm{p}} = \mathrm{d}Q_{\mathrm{p}} \tag{14}$$

Integrating both sides of Eqn 14 gives

$$\Delta H_{\mathrm{p}} = Q_{\mathrm{p}} \tag{15}$$

That is, the enthalpy change of a closed system in passing from an initial to a final state at constant pressure is equal to the heat exchanged with the surroundings. Hence, for a process occurring at constant pressure, the heat is path-independent since it is equal to the change of a state property. This is an important result. As an example, suppose that the initial state of a system consists of 1.0 mol of C and 1.0 mol of O_2 at 298.15 K at 1.0 bar pressure and the final state is 1 mol of CO_2 at the same temperature and pressure. The enthalpy change of this reaction is

$$\mathrm{C} + \mathrm{O_2} = \mathrm{CO_2} \quad \Delta H^{\mathrm{o}}_{298.15} = -393.52 \ \ \mathrm{kJ} \tag{16}$$

(where the superscript on $\Delta H^{\mathrm{o}}_{298.15}$ indicates the "standard state" reaction involving pure solid graphite, CO_2 and O_2 at 1.0 bar pressure). Hence, an exothermic heat of −393.52 kJ will be observed, independent of the reaction path, provided only that the pressure remains constant throughout the process. For instance, during the combustion reaction, the reactants and products may attain high and unknown temperatures. However, once the CO_2 product has cooled back to 298.15 K, the total heat that has been exchanged with the surroundings will be −393.52 kJ independent of the intermediate temperatures.

In **Figure 8** the standard molar enthalpy of Fe is shown as a function of temperature. The y-axis, $(h^{\mathrm{o}}_T - h^{\mathrm{o}}_{298.15})$, is the heat required to heat 1 mol of Fe from 298.15 K to a temperature T at constant pressure. The slope of the curve is the molar heat capacity at constant pressure:

$$c_{\mathrm{p}} = (\mathrm{d}h/\mathrm{d}T)_{\mathrm{p}} \tag{17}$$

From Eqn 17, we obtain the following expression for the heat required to heat 1 mol of a substance from a temperature T_1 to a temperature T_2 at constant P (assuming no phase changes in the interval):

$$(h_{T_2} - h_{T_1}) = \int_{T_1}^{T_2} c_{\mathrm{p}}\mathrm{d}T \tag{18}$$

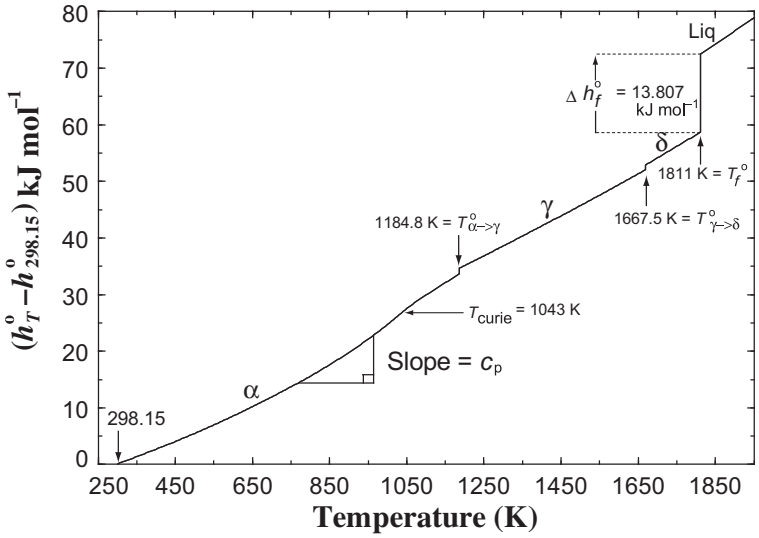

Figure 8 Standard molar enthalpy of Fe (see FactSage).

The enthalpy curve can be measured by the technique of drop calorimetry, or the heat capacity can be measured directly by adiabatic calorimetry.

The standard equilibrium temperature of fusion (melting) of Fe is 1811 K as shown in **Figure 8**. The fusion reaction is a *first-order phase change* since it occurs at constant temperature. The standard molar enthalpy of fusion Δh°_f is 13.807 kJ mol^{-1} as shown in **Figure 8**. It can also be seen in **Figure 8** that Fe undergoes two other first-order phase changes, the first from α (bcc) to γ (fcc) Fe at $T^{\circ}_{\alpha\to\gamma} = 1184.8$ K and the second from γ to δ (bcc) at 1667.5 K. The enthalpy changes are, respectively, 1.013 and 0.826 kJ mol^{-1}. The Curie temperature, $T_{curie} = 1045$ K, which is also shown in **Figure 8**, will be discussed in Section 3.10.

3.2.3 Gibbs Energy

The Gibbs energy (also called the Gibbs free energy, or simply, the free energy), G, is defined as

$$G = H - TS \tag{19}$$

As given in Section 3.2.2, we consider a closed system and assume that the only work term is the work of expansion and that this is reversible. From Eqns 13 and 19,

$$dG_n = dQ + V\,dP - T\,dS - S\,dT \tag{20}$$

Consequently, for a process occurring at constant T and P in a closed system,

$$dG_{T,P,n} = dQ_P - T\,dS = dH_P - T\,dS \tag{21}$$

Consider the case where the "surroundings" are simply a heat reservoir at a temperature equal to the temperature T of the system. That is, no irreversible processes occur in the

surroundings, which receive only a reversible transfer of heat ($-dQ$) at constant temperature. Therefore, from Eqn 8,

$$dS_{surr} = -dQ/T \tag{22}$$

Substituting into Eqn 21 and using Eqn 3 yields

$$dG_{T,P,n} = -T\,dS_{surr} - T\,dS = -T\,dS_{total} \leq 0 \tag{23}$$

Equation 23 may be considered to be a special form of the Second Law for a process occurring in a closed system at constant T and P. From Eqn 23, such a process will be spontaneous if dG is negative.

For our purposes in this chapter, Eqn 23 is the most useful form of the Second Law.

An objection might be raised that Eqn 23 applies only when the surroundings are at the same temperature T as the system. However, if the surroundings are at a different temperature, we simply postulate a hypothetical heat reservoir, which is at the same temperature as the system, and which lies between the system and surroundings, and we consider the irreversible transfer of heat between the reservoir and the real surroundings as a second separate process.

Substituting Eqns 8 and 22 into Eqn 23 gives

$$dG_{T,P,n} = (dQ - dQ_{rev}) \leq 0 \tag{24}$$

In Eqn 24, dQ is the heat of the actual process, while dQ_{rev} is the heat that would be observed were the process occurring reversibly. If the actual process is reversible, that is, if the system is at equilibrium, then $dQ = dQ_{rev}$ and $dG = 0$.

As an example, consider the fusion of Fe in **Figure 8**. At $T_f^o = 1811$ K, solid and liquid are in equilibrium. That is, at this temperature, melting is a reversible process. Therefore, at 1811 K:

$$dg_f^o = dh_f^o - T ds_f^o = 0 \tag{25}$$

Therefore, the molar entropy of fusion at 1811 K is given by

$$\Delta s_f^o = \left(\Delta h_f^o / T\right) \quad \text{when} \quad T = T_f^o \tag{26}$$

Equation 26 applies only at the equilibrium melting point. At temperatures below and above this temperature, the liquid and solid are not in equilibrium. Above the melting point, $\Delta g_f^o < 0$ and melting is a spontaneous process (liquid more stable than solid). Below the melting point, $\Delta g_f^o > 0$ and the reverse process (solidification) is spontaneous. As the temperature deviates progressively further from the equilibrium melting point, the magnitude of Δg_f^o, that is, the magnitude of the driving force, increases. We shall return to this subject in Section 3.4.2.

3.2.4 Chemical Equilibrium

Consider first the question of whether silica fibers in an aluminum matrix at 500 °C will react to form mullite, $Al_6Si_2O_{13}$:

$$13/_2\ SiO_2 + 6Al = 9/_2\ Si + Al_6Si_2O_{13} \tag{27}$$

If the reaction proceeds with the formation of $d\xi$ moles of mullite, then from the stoichiometry of the reaction, $dn_{Si} = (9/2)\, d\xi$, $dn_{Al} = -6\, d\xi$, and $dn_{SiO_2} = -13/2\, d\xi$. Since the four substances are essentially immiscible at 500 °C, their Gibbs energies are equal to their standard molar Gibbs energies, g_i^o (also known as the standard chemical potentials μ_i^o as defined in Section 3.2.7), the standard state of a solid or liquid compound being the pure compound at $P = 1.0$ bar. The Gibbs energy of the system then varies as

$$dG/d\xi = g^o_{Al_6Si_2O_{13}} + 9/_2\, g^o_{Si} - 13/_2\, g^o_{SiO_2} - 6g^o_{Al} = \Delta G^o = -830 \text{ kJ} \tag{28}$$

where ΔG^o is called the standard Gibbs energy change of the reaction (Eqn 27) at 500 °C.

Since $\Delta G^\circ < 0$, the formation of mullite entails a decrease in G. Hence, the reaction will proceed spontaneously so as to minimize G. Equilibrium will never be attained and the reaction will proceed to completion.

3.2.4.1 Equilibria Involving a Gaseous Phase

An *ideal gas* mixture is one that obeys the ideal gas equation of state:

$$PV = nRT \tag{29}$$

where n is the total number of moles. Further, the partial pressure of each gaseous species in the mixture is given by

$$p_i V = n_i RT \tag{30}$$

where $n = \Sigma n_i$ and $P = \Sigma p_i$ (Dalton's Law for ideal gases). R is the ideal gas constant. The *standard state* of an ideal gaseous compound is the pure compound at a pressure of 1.0 bar. It can easily be shown that the partial molar Gibbs energy g_i (also called the chemical potential μ_i as defined in Section 3.2.7) of a species in an ideal gas mixture is given in terms of its standard molar Gibbs energy, g_i^o (also called the standard chemical potential μ_i^o) by

$$g_i = g_i^o + RT \ln p_i \tag{31}$$

The final term in Eqn 31 is entropic. As a gas expands at constant temperature, its entropy increases.

Consider a gaseous mixture of H_2, S_2 and H_2S with partial pressures p_{H_2}, p_{S_2} and p_{H_2S}. The gases can react according to

$$2H_2 + S_2 = 2H_2S \tag{32}$$

If the reaction (Eqn 32) proceeds to the right with the formation of $2d\xi$ moles of H_2S, then the Gibbs energy of the system varies as

$$\begin{aligned} dG/d\xi &= 2g_{H_2S} - 2g_{H_2} - g_{S_2} \\ &= \left(2g^o_{H_2S} - 2g^o_{H_2} - g^o_{S_2}\right) + RT\left(2\ln p_{H_2S} - 2\ln p_{H_2} - \ln p_{S_2}\right) \\ &= \Delta G^o + RT \ln\left(p^2_{H_2S}\ p^{-2}_{H_2}\, p^{-1}_{S_2}\right) \\ &= \Delta G \end{aligned} \tag{33}$$

ΔG, which is the Gibbs energy change of the reaction (Eqn 32), is thus a function of the partial pressures. If $\Delta G < 0$, then the reaction will proceed to the right, so as to minimize G. In a closed system, as the reaction continues with the production of H_2S, p_{H_2S} will increase while p_{H_2} and p_{S_2} will decrease. As a result, ΔG will become progressively less negative. Eventually, an equilibrium state will be reached when $dG/d\xi = \Delta G = 0$.

For the equilibrium state, therefore,

$$\begin{aligned} \Delta G^{o} &= -RT \ln\ K \\ &= -RT \ln\left(p_{H_2S}^{2}\ p_{H_2}^{-2}\ p_{S_2}^{-1}\right)_{\text{equilibrium}} \end{aligned} \tag{34}$$

where K, the "equilibrium constant" of the reaction, is the one unique value of the ratio $(p_{H_2S}^{2}\ p_{H_2}^{-2}\ p_{S_2}^{-1})$ for which the system will be in equilibrium at the temperature T.

If the initial partial pressures are such that $\Delta G > 0$, then the reaction (Eqn 32) will proceed to the left in order to minimize G until the equilibrium condition of Eqn 34 is attained.

As a further example, consider the possible precipitation of graphite from a gaseous mixture of CO and CO_2. The reaction is

$$2CO = C + CO_2 \tag{35}$$

Proceeding as above, we can write:

$$\begin{aligned} dG/d\xi &= g_C + g_{CO_2} - 2g_{CO} \\ &= \left(g_C^{o} + g_{CO_2}^{o} - 2g_{CO}^{o}\right) + RT \ln\left(p_{CO_2} p_{CO}^{-2}\right) \\ &= \Delta G^{o} + RT \ln\left(p_{CO_2} p_{CO}^{-2}\right) \\ &= \Delta G = -RT \ln K + RT \ln\left(p_{CO_2} p_{CO}^{-2}\right) \end{aligned} \tag{36}$$

If $(p_{CO_2} p_{CO}^{-2})$ is less than the equilibrium constant K, then precipitation of graphite will occur in order to decrease G.

Real situations are, of course, generally more complex. To treat the deposition of solid Si from a vapor of SiI_4, for example, we must consider the formation of gaseous I_2, I and SiI_2, so that three independent reaction equations must be written:

$$SiI_4(g) = Si(sol) + 2I_2(g) \tag{37}$$

$$SiI_4(g) = SiI_2(g) + I_2(g) \tag{38}$$

$$I_2(g) = 2I(g) \tag{39}$$

The equilibrium state, however, is still that which minimizes the total Gibbs energy of the system. This is equivalent to satisfying simultaneously the equilibrium constants of the reactions shown in Eqns 37–39.

Equilibria involving reactants and products that are solid or liquid solutions will be discussed in Section 3.4.1.4.

3.2.4.2 Predominance Diagrams

Predominance diagrams are a particularly simple type of phase diagram, which have many applications in the fields of hot corrosion, chemical vapor deposition, etc. Furthermore, their construction clearly illustrates the principles of Gibbs energy minimization.

A predominance diagram for the Cu–SO_2–O_2 system at 700 °C is shown in **Figure 9**. The axes are the logarithms of the partial pressures of SO_2 and O_2 in the gas phase. The diagram is divided into areas or domains of stability of the various solid compounds of Cu, S and O. For example, at point Z, where $p_{SO_2} = 10^{-2}$ and $p_{O_2} = 10^{-7}$ bar, the stable phase is Cu_2O. The conditions for coexistence of two and three solid phases are indicated, respectively, by the lines and triple points on the diagram. For example, along the line separating the Cu_2O and $CuSO_4$ domains, the equilibrium constant $K = p_{SO_2}^{-2} p_{O_2}^{-3/2}$ of the following reaction is satisfied:

$$Cu_2O + 2SO_2 + 3/2\, O_2 = 2CuSO_4 \tag{40}$$

Hence, along this line,

$$\log K = -\Delta G^{o}/RT = -2 \log p_{SO_2} - 3/2 \log p_{O_2} \tag{41}$$

This line is thus straight with slope $(-3/2)/2 = -3/4$.

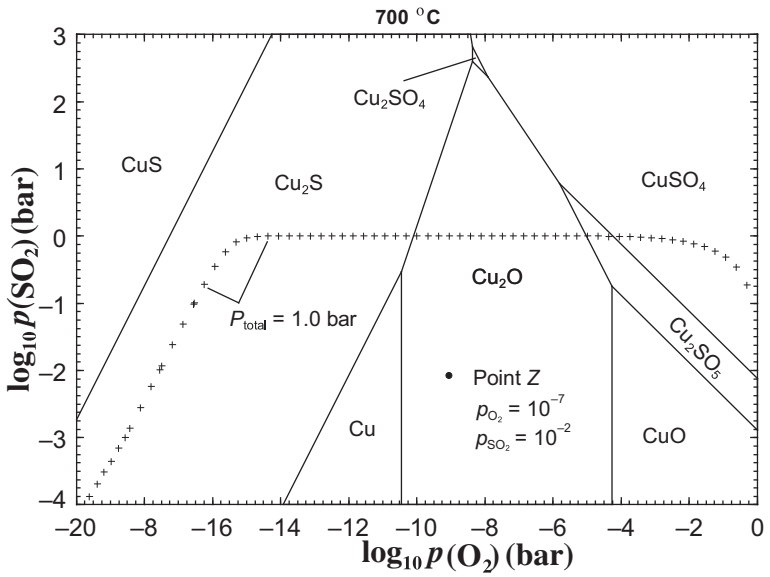

Figure 9 "Predominance" phase diagram of the Cu–SO_2–O_2 system at 700 °C showing the solid phases at equilibrium as a function of the equilibrium SO_2 and O_2 partial pressures (see FactSage).

We can construct **Figure 9** following the procedure of Bale et al. (1986). We formulate a reaction for the formation of each solid phase, always from 1 mol of Cu, and involving the gaseous species whose pressures are used as the axes (SO_2 and O_2 in this example):

$$Cu + 1/2\ O_2 = CuO \qquad \Delta G = \Delta G^o + RT \ln\ p_{O_2}^{-1/2} \tag{42}$$

$$Cu + 1/4\ O_2 = 1/2\ Cu_2O \qquad \Delta G = \Delta G^o + RT \ln\ p_{O_2}^{-1/4} \tag{43}$$

$$Cu + SO_2 = CuS + O_2 \qquad \Delta G = \Delta G^o + RT \ln\left(p_{O_2} p_{SO_2}^{-1}\right) \tag{44}$$

$$Cu + SO_2 + O_2 = CuSO_4 \qquad \Delta G = \Delta G^o + RT \ln\left(p_{SO_2}^{-1} p_{O_2}^{-1}\right) \tag{45}$$

and similarly for the formation of Cu_2S, Cu_2SO_4 and Cu_2SO_5.

The values of ΔG^o are obtained from tables of thermodynamic properties. For any given values of p_{SO_2} and p_{O_2}, ΔG for each formation reaction can then be calculated. The stable compound is simply the one with the most negative ΔG. If all the ΔG values are positive, then pure Cu is the stable compound.

By reformulating Eqns 42–45 in terms of, for example, S_2 and O_2 rather than SO_2 and O_2, a predominance diagram with log p_{S_2} and log p_{O_2} as axes can be constructed. Logarithms of ratios or products of partial pressures can also be used as axes.

Along the curve shown by the crosses in **Figure 9**, the total pressure is 1.0 bar. That is, the gas consists not only of SO_2 and O_2, but of other species such as S_2 whose equilibrium partial pressures can be calculated. Above this line, the total pressure is >1.0 bar even though the sum of the partial pressures of SO_2 and O_2 may be <1.0 bar.

A similar phase diagram of $RT \ln p_{O_2}$ vs T for the Cu–O_2 system is shown in **Figure 10**. For the formation reaction,

$$4Cu + O_2 = 2Cu_2O \tag{46}$$

we can write

$$\Delta G^o = -RT \ln K = RT \ln\left(p_{O_2}\right)_{\text{equilibrium}} = \Delta H^o - T\Delta S^o \tag{47}$$

The line between the Cu and Cu_2O domains in **Figure 10** is thus a plot of the standard Gibbs energy of formation of Cu_2O versus T. The temperatures indicated by the symbols M and $\boxed{M}$ are the melting points of Cu and Cu_2O, respectively. This line is thus simply a line taken from the well-known *Ellingham diagram or* ΔG^o vs T diagram for the formation of oxides. However, by drawing vertical lines at the melting points of Cu and Cu_2O as shown in **Figure 10**, we convert the Ellingham diagram to a phase diagram. Stability domains for Cu(sol), Cu(liq), Cu_2O(sol), Cu_2O(liq) and CuO(sol) are shown as functions of T and of the imposed equilibrium p_{O_2}. The lines and triple points indicate conditions for two- and three-phase equilibria.

3.2.5 Measuring Gibbs Energy, Enthalpy and Entropy

3.2.5.1 Measuring Gibbs Energy Change

In general, the Gibbs energy change of a process can be determined by performing measurements under equilibrium conditions. For example, consider the reaction shown in Eqn 35. Experimentally,

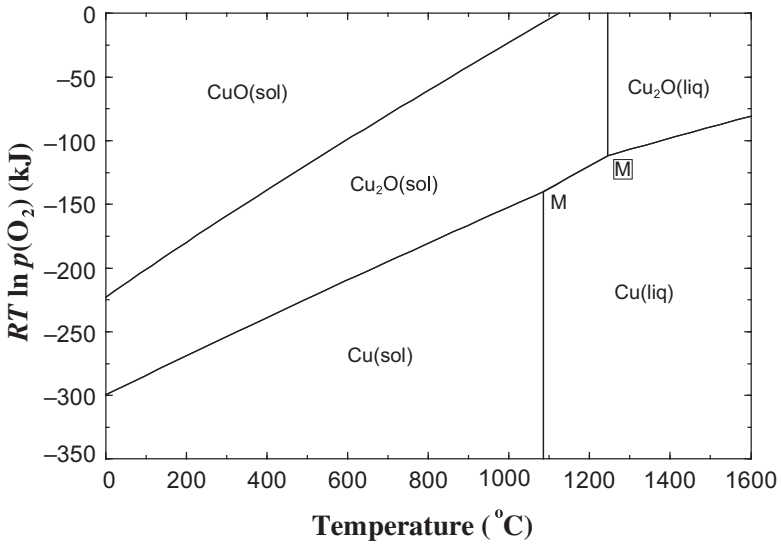

Figure 10 Predominance phase diagram (also known as a Gibbs energy—*T* diagram or an Ellingham diagram) for the $Cu–O_2$ system. Points M and $\boxed{M}$ are are the melting points of Cu and Cu_2O respectively (see FactSage).

equilibrium is first established between solid C and the gas phase and the equilibrium constant is then found by measuring the partial pressures of CO and CO_2. Equation 36 is then used to calculate ΔG^{o}.

Another common technique of establishing equilibrium is by means of an electrochemical cell. A galvanic cell is designed, so that a reaction (the cell reaction) can occur only with the passage of an electric current through an external circuit. An external voltage is applied which is equal in magnitude but opposite in sign to the cell potential, E (volts), such that no current flows. The system is then at equilibrium. With the passage of dz coulombs through the external circuit, Edz joules of work are performed. Since the process occurs at equilibrium, this is the reversible non-PV work, $dW_{rev(non\text{-}PV)}$. Substituting Eqn 11 in Eqn 19, differentiating, and substituting Eqn 10 gives:

$$dG = V\,dP - S\,dT + \sum \mu_i\,dn_i + dW_{rev(non-PV)} \tag{48}$$

For a closed system at constant T and P,

$$dG_{T,P,n} = dW_{rev(non-PV)} \tag{49}$$

If the cell reaction is formulated such that the advancement of the reaction by $d\xi$ moles is associated with the passage of dz coulombs through the external circuit, then from Eqn 49,

$$\Delta G\,d\xi = -E\,dz \tag{50}$$

Hence,

$$\Delta G = -FE \tag{51}$$

where ΔG is the Gibbs energy change of the cell reaction, $F = \mathrm{d}z/\mathrm{d}\xi = 96,500\ \mathrm{C\ mol^{-1}}$ is the Faraday constant, which is the number of coulombs in a mole of electrons, and the negative sign follows the usual electrochemical sign convention. Hence, by measuring the open-circuit voltage, E, one can determine ΔG of the cell reaction.

3.2.5.2 Measuring Enthalpy Change

The enthalpy change, ΔH, of a process may be measured directly by calorimetry. Alternatively, if ΔG is measured by an equilibration technique as in Section 3.2.5.1, then ΔH can be determined from the measured temperature dependence of ΔG. From Eqn 48, for a process in a closed system with no non-PV work at constant pressure,

$$(\mathrm{d}G/\mathrm{d}T)_{\mathrm{P,n}} = -S \tag{52}$$

Substitution of Eqn 19 into Eqn 52 gives

$$(\mathrm{d}(G/T)/\mathrm{d}(1/T))_{\mathrm{P,n}} = H \tag{53}$$

Equations 52 and 53 apply to both the initial and final states of a process. Hence,

$$(\mathrm{d}(\Delta G)/\mathrm{d}T)_{\mathrm{P,n}} = -\Delta S \tag{54}$$

$$(\mathrm{d}(\Delta G/T)\mathrm{d}(1/T))_{\mathrm{P,n}} = \Delta H \tag{55}$$

Equations 52–55 are forms of the *Gibbs–Helmholtz equation.*

3.2.5.3 Measuring Entropy

As is the case with the enthalpy, ΔS of a process can be determined from the measured temperature dependence of ΔG by means of Eqn 54. This is known as the "second law method" of measuring entropy.

Another method of measuring entropy involves the *Third Law* of thermodynamics, which states that the entropy of a perfect crystal of a pure substance at internal equilibrium at a temperature of 0 K is zero. This follows from Eqn 2 and the concept of entropy as disorder. For a perfectly ordered system at absolute zero, $t = 1$ and $S = 0$.

Let us first derive an expression for the change in entropy as a substance is heated. Combining Eqns 52 and 53 gives:

$$(\mathrm{d}H/\mathrm{d}T)_{\mathrm{P,n}} = T(\mathrm{d}S/\mathrm{d}T)_{\mathrm{P,n}} \tag{56}$$

Substituting Eqn 18 into Eqn 56 and integrating, then gives the following expression for the entropy change as 1 mol of a substance is heated at constant P from T_1 to T_2:

$$(s_{\mathrm{T_2}} - s_{\mathrm{T_1}}) = \int_{\mathrm{T_1}}^{\mathrm{T_2}} (c_{\mathrm{p}}/T)\mathrm{d}T \tag{57}$$

The similarity to Eqn 18 is evident, and a plot of $(s_{\mathrm{T_2}} - s_{\mathrm{T_1}})$ versus T is similar in appearance to **Figure 8**.

Setting $T_1 = 0$ in Eqn 57 and using the Third Law gives

$$s_{T_2} = \int_0^{T_2} (c_P/T)\,dT \tag{58}$$

Hence, if c_P has been measured down to temperatures sufficiently close to 0 K, Eqn 58 can be used to calculate the absolute entropy. This is known as the "third law method" of measuring entropy.

3.2.5.4 Zero Entropy and Zero Enthalpy

The third law method permits the measurement of the absolute entropy of a substance, whereas the second law method permits the measurement only of entropy changes, ΔS.

The Third Law is not a convention. It provides a natural zero for entropy. On the other hand, no such natural zero exists for the enthalpy since there is no simple natural zero for the internal energy. However, by convention, the absolute enthalpy of a pure element in its stable state at $P = 1.0$ bar and $T = 298.15$ K is usually set to zero. Therefore, the absolute enthalpy of a compound is, by convention, equal to its standard enthalpy of formation from the pure elements in their stable standard states at 298.15 K.

3.2.6 Auxiliary Functions

It was shown in Section 3.2.3 that Eqn 23 is a special form of the Second Law for a process occurring at constant T and P. Other special forms of the Second Law can be derived in a similar manner.

It follows directly from Eqns 3, 12 and 22, for a process at constant V and S, that

$$dU_{V,S,n} = -T\,dS_{total} \leq 0 \tag{59}$$

Similarly, from Eqns 3, 13 and 22,

$$dH_{P,S,n} = -T\,dS_{total} \leq 0 \tag{60}$$

Equations 59 and 60 are not of direct practical use since there is no simple means of maintaining the entropy of a system constant during a change of state. A more useful function is the *Helmholtz energy*, A, defined as:

$$A = U - TS \tag{61}$$

From Eqns 12 and 40,

$$dA_n = dQ - P\,dV - T\,dS - S\,dT \tag{62}$$

Then, from Eqns 3 and 22, for processes at constant T and V,

$$dA_{T,V,n} = -T\,dS_{total} \leq 0 \tag{63}$$

Equations 23, 59, 60 and 63 are special forms of the Second Law for closed systems. In this regard, H, A and G are sometimes called *auxiliary functions*. If we consider open systems, then many other auxiliary functions can be defined as will be shown in Section 3.2.8.2.

In Section 3.2.3, the very important result was derived that the equilibrium state of a system corresponds to a minimum of the Gibbs energy G. This is used as the basis of nearly all algorithms for calculating chemical equilibria and phase diagrams. An objection might be raised that Eqn 23 only applies at constant T and P. What if equilibrium were approached at constant T and V for instance? Should we not then minimize A as in Eqn 63? The response is that the restrictions on Eqns 23 and 63 only apply to the paths followed during the approach to equilibrium. However, for a system at an equilibrium temperature, pressure and volume, it clearly does not matter along which hypothetical path the approach to equilibrium was calculated. The reason that most algorithms minimize G rather than other auxiliary functions is simply that it is generally easiest and most convenient to express thermodynamic properties in terms of the independent variables T, P and n_i.

3.2.7 The Chemical Potential

The chemical potential was defined in Eqn 5. However, this equation is not particularly useful directly since it is difficult to see how S can be held constant.

Substituting Eqn 11 into Eqn 19, differentiating and substituting Eqn 9 gives

$$\mathrm{d}G = V\,\mathrm{d}P - S\,\mathrm{d}T + \sum \mu_i \mathrm{d}n_i \tag{64}$$

from which it can be seen that μ_i is also given by

$$\mu_i = (\partial G/\partial n_i)_{\mathrm{T,P,n}_{j\neq i}} \tag{65}$$

Differentiating Eqn 11 with substitution of Eqn 9 gives

$$\mathrm{d}H = T\,\mathrm{d}S + V\,\mathrm{d}P + \sum \mu_i \mathrm{d}n_i \tag{66}$$

whence

$$\mu_i = (\partial H/\partial n_i)_{\mathrm{T,V,n}_{j\neq i}} \tag{67}$$

Similarly it can be shown that

$$\mu_i = (\partial A/\partial n_i)_{\mathrm{T,V,n}_{j\neq i}} \tag{68}$$

Among these equations for μ_i, the most useful is Eqn 65. The chemical potential of a component i of a system is given by the increase in Gibbs energy as the component is added to the system at constant T and P while keeping the numbers of moles of all other components of the system constant.

The chemical potentials of its components are intensive properties of a system; for a system at a given T, P and composition, the chemical potentials are independent of the mass of the system. That is, with reference to Eqn 65, adding $\mathrm{d}n_i$ moles of component i to a solution of a fixed composition will result in a change in Gibbs energy dG, which is independent of the total mass of the solution.

The reason that this property is called a chemical potential is illustrated by the following thought experiment. Imagine two systems, I and II, at the same temperature and pressure and separated by a membrane that permits the passage of only one component, say component 1. The chemical potentials of component 1 in systems I and II are $\mu_1^{\mathrm{I}} = \partial G^{\mathrm{I}}/\partial n_1^{\mathrm{I}}$ and $\mu_1^{\mathrm{II}} = \partial G^{\mathrm{II}}/\partial n_1^{\mathrm{II}}$. Component 1 is

transferred across the membrane with $dn_1^{I} = -dn_1^{II}$. The change in the total Gibbs energy accompanying this transfer is then:

$$dG = d\left(G^{I} + dG^{II}\right) = -\left(\mu_1^{I} - \mu_1^{II}\right)dn_1^{II} \tag{69}$$

If $\mu_1^{I} > \mu_1^{II}$, then $d(G^{I} + dG^{II})$ is negative when dn_1^{II} is positive. That is, the total Gibbs energy is decreased by a transfer of component 1 from system I to system II. Hence, component 1 is transferred spontaneously from a system of higher μ_1 to a system of lower μ_1. For this reason, μ_1 is called the chemical potential of component 1.

Similarly, by using the appropriate auxiliary functions, it can be shown that μ_i is the potential for the transfer of component i at constant T and V, at constant S and V, etc.

An important principle of phase equilibrium can now be stated. *When two or more phases are in equilibrium, the chemical potential of any component is the same in all phases*. This criterion for phase equilibrium is thus equivalent to the criterion of minimizing G. This will be discussed further in Section 3.4.2.

3.2.8 Some Other Useful Thermodynamic Equations

In this section, some other useful thermodynamic relations are derived. Consider an open system, which is initially empty. That is, initially S, V and n are all equal to zero. We now "fill up" the system by adding a previously equilibrated mixture. The addition is made at constant T, P and composition. Hence, it is also made at constant μ_i (of every component) since μ_i is an intensive property. The addition is continued until the entropy, volume and numbers of moles of the components in the system are S, V and n_i. Integrating Eqn 9 from the initial (empty) to the final state then gives:

$$U = TS - PV + \sum n_i\mu_i \tag{70}$$

It then follows that

$$H = TS + \sum n_{\mathrm{i}}\mu_{\mathrm{i}} \tag{71}$$

$$A = -PV + \sum n_{\mathrm{i}}\mu_{\mathrm{i}} \tag{72}$$

and most importantly

$$G = \sum n_i\mu_i \tag{73}$$

3.2.8.1 The Gibbs–Duhem Equation

By differentiation of Eqn 70,

$$dU = T\,dS + S\,dT - P\,dV - V\,dP + \sum n_i d\mu_i + \sum \mu_i dn_i \tag{74}$$

By comparison of Eqns 9 and 74, it follows that

$$S\,dT - V\,dP + \sum n_i d\mu_i = 0 \tag{75}$$

This is the general Gibbs–Duhem equation.

3.2.8.2 General Auxiliary Functions

It was stated in Section 3.2.6 that many auxiliary functions can be defined for open systems. Consider, for example, the auxiliary function:

$$\begin{aligned} G' &= U - (-PV) - TS - \sum_{1}^{k} n_i \mu_i \\ &= G - \sum_{1}^{k} n_i \mu_i \end{aligned} \tag{76}$$

Differentiating Eqn 76 with substitution of Eqn 64 gives

$$\mathrm{d}G' = V\,\mathrm{d}P - S\,\mathrm{d}T - \sum_{1}^{k} n_i \mathrm{d}\mu_i + \sum_{k+1}^{\mathrm{C}} \mu_i \mathrm{d}n_i \tag{77}$$

where C is the number of components in the system. It then follows that

$$\mathrm{d}G'_{\mathrm{T,P},\mu_i(1\le i\le k),\ \mathrm{n}_i(k+1\le i\le C)} \le 0 \tag{78}$$

is the criterion for a spontaneous process at constant T, P, μ_i (for $1 \le i \le k$) and n_i (for $k+1 \le i \le C$) and that equilibrium is achieved when $\mathrm{d}G' = 0$. The chemical potential of a component may be held constant, for example, by equilibration with a gas phase as, for example, by fixing the partial pressure of O_2, SO_2, etc.

Finally, it also follows that the chemical potential may be defined very generally as

$$\mu_i = (\partial G'/\partial n_i)_{\mathrm{T,P},\mu_i(1\le i\le k),\ \mathrm{n}_i(k+1\le i\le \mathrm{C})} \tag{79}$$

The discussion of the generalized auxiliary functions will be continued in Section 3.7.7.

3.3 The Gibbs Phase Rule

The geometry of all types of phase diagrams is governed by the *Gibbs Phase Rule*, which applies to any system at equilibrium:

$$F = C - P + 2 \tag{80}$$

The Phase Rule will be derived in this section in a general form along with several examples. Further examples will be presented in later sections.

In Eqn 80, C is the number of *components* in the system. This is the minimum number of substances required to describe the elemental composition of every phase present. As an example, for pure H_2O at 25 °C and 1.0 bar pressure, $C = 1$. For a gaseous mixture of H_2, O_2 and H_2O at high temperature, $C = 2$. (Although there are many species present in the gas including O_2, H_2, H_2O, O_3, etc., these species are all at equilibrium with each other. At a given T and P, it is sufficient to know the overall elemental composition in order to be able to calculate the concentration of every species. Hence, $C = 2$. C can never exceed the number of elements in the system.)

For the systems shown in **Figures 1–7**, respectively, $C = 2$, 3, 3, 4, 3, 4 and 1.

There is generally more than one way to specify the components of a system. For example, the Fe–Si–O system could also be described as the FeO–Fe_2O_3–SiO_2 system, or the FeO–SiO_2–O_2 system, etc. The formulation of a phase diagram can often be simplified by a judicious definition of the components as will be discussed in Section 3.7.5.

In Eqn 80, P is the number of *phases* present at equilibrium at a given point on the phase diagram. For example, in **Figure 1** at any point within the region labeled "Liquid + bcc", $P = 2$. At any point in the region labeled "Liquid," $P = 1$.

In Eqn 80, F is the *number of degrees of freedom* or the *variance* of the system at a given point on the phase diagram. It is the number of variables that must be specified in order to completely specify the state of the system. Let us number the components as 1, 2, 3,……, C and designate the phases as α, β, γ, ……. In most derivations of the Phase Rule, the only variables considered are T, P and the compositions of the phases. However, since we also want to treat more general phase diagrams in which chemical potentials, volumes, enthalpies, etc. can also be variables, we shall extend the list of variables as follows:

$$T, P$$
$$\left(X_1^{\alpha}, X_2^{\alpha}, \ldots X_{C-1}^{\alpha}\right), \left(X_1^{\beta}, X_2^{\beta}, \ldots X_{C-1}^{\beta}\right), \ldots$$
$$\mu_1, \mu_2, \mu_3, \ldots$$
$$V^{\alpha}, V^{\beta}, V^{\gamma}, \ldots$$
$$S^{\alpha}, S^{\beta}, S^{\gamma}, \ldots$$

where X_i^{α} is the mole fraction of component i in phase α, μ_i is the chemical potential of component i, and V^{α} and S^{α} are the volume and entropy of phase α. Alternatively, we may substitute mass fractions for mole fractions and enthalpies H^{α}, H^{β}, … for S^{α}, S^{β}, …

It must be stressed that the overall composition of the system is not a variable in the sense of the Phase Rule. The composition variables are the compositions of the individual phases.

The total number of variables is thus equal to $(2 + P(C - 1) + C + 2P)$.

(Only $(C - 1)$ independent composition variables X_i are required for each phase since the sum of the mole fractions is unity.)

At equilibrium, the chemical potential μ_i of each component i is the same in all phases (Section 3.2.7) as are T and P. μ_i is an intensive variable (Section 3.2.7), which is a function of T, P and composition. Hence,

$$\mu_i^{\alpha}\left(T, P, X_1^{\alpha}, X_2^{\alpha}, \ldots,\right) = \mu_i^{\beta}\left(T, P, X_1^{\beta}, X_2^{\beta}, \ldots,\right) = \ldots\ldots = \mu_i \tag{81}$$

This yields PC equations relating the variables. Furthermore, the volume of each phase is a function of T, P and composition, $V^{\alpha} = (T, P, X_1^{\alpha}, X_2^{\alpha}, \ldots,)$, as is the entropy of the phase (or, alternatively, the enthalpy). This yields an additional $2P$ equation relating the variables.

F is then equal to the number of variables minus the number of equations relating the variables at equilibrium:

$$F = (2 + P(C - 1) + C + 2P) - PC - 2P = C - P + 2 \tag{82}$$

Equation 80 is thereby derived.

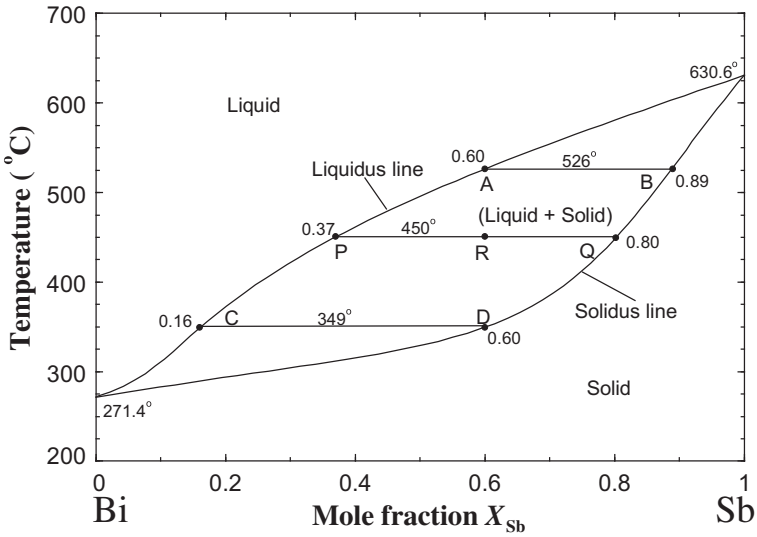

Figure 11 Temperature-composition phase diagram at $P = 1$ bar of the Bi–Sb system (see FactSage; SGTE).

3.3.1 The Phase Rule and Binary Temperature-Composition Phase Diagrams

As a first example of the application of the Phase Rule, consider the temperature-composition (T–X) phase diagram of the Bi–Sb system at a constant applied pressure of 1.0 bar in **Figure 11**. The abscissa of **Figure 11** is the composition, expressed as mole fraction of Sb, X_{Sb}. Note that $X_{Bi}=1-X_{Sb}$. Phase diagrams are also often drawn with the composition axis expressed as weight percentage.

At all compositions and temperatures in the area above the line labeled "liquidus," a single-phase liquid solution will be observed, while at all compositions and temperatures below the line labeled "solidus," there will be a single-phase solid solution. A sample at equilibrium at a temperature and overall composition between these two curves will consist of a mixture of solid and liquid phases, the compositions of which are given by the liquidus and solidus compositions at that temperature. For example, a sample of overall composition $X_{Sb} = 0.60$ at $T = 450$ °C (at point R in **Figure 11**) will consist, at equilibrium, of a mixture of a liquid of composition $X_{Sb} = 0.37$ (point P) and solid of composition $X_{Sb} = 0.80$ (point Q). The line PQ is called a *tie-line* or *conode*.

Binary temperature-composition phase diagrams are generally plotted at a fixed pressure, usually 1.0 bar. This eliminates one degree of freedom. In a binary system, $C = 2$. Hence, for binary isobaric T–X diagrams the phase rule reduces to

$$F = 3 - P \tag{83}$$

Binary T–X diagrams contain single-phase areas and two-phase areas. In the single-phase areas, $F = 3 - 1 = 2$. That is, temperature and composition can be specified independently. These regions are thus called *bivariant*. In two-phase regions, $F = 3 - 2 = 1$. If, say, T is specified, then the compositions of both phases are determined by the ends of the tie-lines. Two-phase regions are thus termed *univariant*. Note that although the overall composition can vary over a range within a two-phase region at constant T, the overall composition is not a parameter in the sense of the phase rule. Rather, it is the

compositions of the individual phases at equilibrium that are the parameters to be considered in counting the number of degrees of freedom.

As the overall composition is varied at 450 °C between points P and Q, the compositions of the liquid and solid phases remain fixed at P and Q, and only the relative proportions of the two phases change. From a simple mass balance, we can derive the *lever rule* for binary systems: (moles of liquid)/(moles of solid) = QR/PR, where QR and PR are the lengths of the line segments. Hence, at 450 °C, a sample with overall composition $X_{Sb} = 0.60$ consists of liquid and solid phases in the molar ratio $(0.80 - 0.60)/(0.60 - 0.37) = 0.87$. Were the composition axis expressed as weight percent, then the lever rule would give the weight ratio of the two phases.

Suppose that a liquid Bi–Sb solution with composition $X_{Sb} = 0.60$ is cooled very slowly from an initial temperature above 526 °C. When the temperature has decreased to the liquidus temperature 526 °C (point A), the first solid appears, with a composition at point B ($X_{Sb} = 0.89$). As the temperature is decreased further, solid continues to precipitate with the compositions of the two phases at any temperature being given by the liquidus and solidus compositions at that temperature and with their relative proportions being given by the lever rule. Solidification is complete at 349 °C, the last liquid to solidify having composition $X_{Sb} = 0.16$ (point C).

The process just described is known as *equilibrium cooling*. At any temperature during equilibrium cooling, the solid phase has a uniform (homogeneous) composition. In the preceding example, the composition of the solid phase during cooling varies along the line BQD. Hence, in order for the solid grains to have a uniform composition at any temperature, diffusion of Sb from the center to the surface of the growing grains must occur. Since solid-state diffusion is a relatively slow process, equilibrium-cooling conditions are only approached if the temperature is decreased very slowly. If a sample of composition $X_{Sb} = 0.60$ is cooled rapidly from the liquid, concentration gradients will be observed in the solid grains, with the concentration of Sb decreasing toward the surface from a maximum of $X_{Sb} = 0.89$ (point B). Furthermore, in this case, solidification will not be complete at 349 °C since at 349 °C, the average concentration of Sb in the solid grains will be greater than $X_{Sb} = 0.60$. These considerations are discussed more fully in Section 3.9 and in Chapter 7 of this volume.

At $X_{Sb} = 0$ and $X_{Sb} = 1$ in **Figure 11**, the liquidus and solidus curves meet at the equilibrium melting points, or *temperatures of fusion* of Bi and Sb, which are $T^{o}_{f(Bi)} = 271.4$ °C and $T^{o}_{f(Sb)} = 630.6$ °C. At these two points, the number of components is reduced to 1. Hence, from the Phase Rule the two-phase region becomes *invariant* ($F = 0$) and solid and liquid coexist at the same temperature.

The phase diagram is influenced by the total pressure, P. Unless otherwise stated, T–X diagrams are usually presented for P = constant = 1.0 bar. For equilibria involving only solid and liquid phases, the phase boundaries are typically shifted only by the order of a few hundredths of a degree per bar change in P. Hence, the effect of pressure upon the phase diagram is generally negligible unless the pressure is of the order of hundreds of bars. On the other hand, if gaseous phases are involved, the effect of pressure is very important. The effect of pressure will be discussed in Section 3.4.3.

3.3.1.1 Three-phase Invariants in Binary Temperature-Composition Phase Diagrams

When three phases are at equilibrium in a binary system at constant pressure, then from Eqn 83, $F = 0$. Hence, the compositions of all three phases as well as T are fixed and the system is said to be *invariant*. An example is the line PQR in **Figure 1** in the T–X diagram of the Fe–Mo system. At any overall composition of the system lying between points P and R at 1612 °C, three phases will be in equilibrium: liquid, sigma and bcc, with compositions at points P, Q and R, respectively. Several other invariants can also be seen in **Figure 1**. Binary T–X diagrams and invariant reactions will be discussed in detail in Section 3.5.

3.3.2 Other Examples of Applications of the Phase Rule

Despite its apparent simplicity, the Phase Rule is frequently misunderstood and incorrectly applied. In this section, a few additional illustrative examples of the application of the Phase Rule will be briefly presented. These examples will be elaborated upon in subsequent sections.

In the single-component Al_2SiO_5 system ($C = 1$) shown in **Figure 7**, the Phase Rule reduces to

$$F = 3 - P \tag{84}$$

Three allotropes of Al_2SiO_5 are shown in the figure. In the single-phase regions, $F = 2$; in these bivariant regions, both P and T (**Figure 7**a) or both V and T (**Figure 7**b) can be specified independently. When two phases are in equilibrium, $F = 1$. Two-phase equilibrium is, therefore, represented by the univariant lines in the P–T phase diagram in **Figure 7**a; when two phases are in equilibrium, T and P cannot be specified independently. When all three allotropes are in equilibrium, $F = 0$. Three-phase equilibrium can, thus, only occur at the invariant *triple point* (530 °C, 3859 bar) in **Figure 7**a.

The invariant triple point in **Figure 7**a becomes the invariant line PQR at $T = 530$ °C in the V–T phase diagram in **Figure 7**b. When the three phases are in equilibrium, the total molar volume of the system can lie anywhere on this line depending upon the relative amounts of the three phases present. However, the molar volumes of the individual allotropes are fixed at points P, Q and R. It is the molar volumes of the individual phases that are the system variables in the sense of the Phase Rule. Similarly, the two-phase univariant lines in **Figure 7**a become the two-phase univariant areas in **Figure 7**b. The lever rule can be applied in these regions to give the ratio of the volumes of the two phases at equilibrium.

As another example, consider the phase diagram section for the ternary ($C = 3$) Zn–Mg–Al system shown in **Figure 3**a. Since the total pressure is constant, one degree of freedom is eliminated. Consequently,

$$F = 4 - P \tag{85}$$

Although the diagram is plotted at constant 10 mol% Zn, this is a composition variable of the entire system, not of any individual phase. That is, it is not a variable in the sense of the Phase Rule, and setting it as a constant does not reduce the number of degrees of freedom. Hence, for example, the three-phase regions in **Figure 3**a are univariant ($F = 1$); at any given T, the compositions of all three phases are fixed, but the three-phase region extends over a range of temperature. Ternary temperature-composition phase diagrams will be discussed in detail in Section 3.6.

Finally, we shall examine some diagrams with chemical potentials as variables. As a first example, the phase diagram of the Fe–Ni–O_2 system in **Figure 5** is a plot of the equilibrium oxygen pressure (fixed, for example, by equilibrating the solid phases with a gas phase of fixed p_{O_2}) versus the molar ratio Ni/(Fe + Ni) at constant T and constant total hydrostatic pressure. For an ideal gas, it follows from Eqn 31 and the definition of chemical potential (Section 3.2.7) that

$$\mu_i = \mu_i^{\circ} + RT \ln\ p_i \tag{86}$$

where μ_i° is the standard-state (at $p_i = 1.0$ bar) chemical potential of the pure gas at temperature T. Hence, if T is constant, μ_i varies directly as $\ln p_i$. The y-axis in **Figure 5** thus varies directly as μ_{O_2}. Fixing T and hydrostatic pressure eliminates two degrees of freedom. Hence, $F = 3 - P$. Therefore, **Figure 5** has

the same topology as a binary T–X diagram like Figure 1, with single-phase bivariant areas, two-phase univariant areas with tie-lines, and three-phase invariant lines at fixed log p_{O_2} and fixed compositions of the three phases.

As a second example, in the isothermal predominance diagram of the Cu–SO_2–O_2 system in Figure 9, the x- and y-axis variables vary as μ_{O_2} and μ_{SO_2}. Since $C = 3$ and T is constant,

$$F = 4 - P \tag{87}$$

The diagram has a topology similar to the P–T phase diagram of a one-component system as in Figure 7a. Along the lines of the diagram, two solid phases are in equilibrium and at the triple points, three solid phases coexist. However, a gas phase is also present everywhere. Hence, at the triple points, there are really four phases present at equilibrium, while the lines represent three-phase equilibria. Hence, the diagram is consistent with Eqn 87.

It is instructive to look at Figure 9 in another way. Suppose that we fix a constant hydrostatic pressure of 1.0 bar (for example, by placing the system in a cylinder fitted with a piston). This removes one further degree of freedom, so that now $F = 3 - P$. However, as long as the total equilibrium gas pressure is <1.0 bar, there will be no gas phase present, and so the diagram is consistent with the Phase Rule. On the other hand, above the 1.0 bar curve shown by the line of crosses in Figure 9, the total gas pressure exceeds 1.0 bar. Hence, the phase diagram calculated at a total hydrostatic pressure of 1.0 bar must terminate at this curve.

The Phase Rule may be applied to the four-component isothermal Fe–Cr–S_2–O_2 phase diagram in Figure 10 in a similar way. Remember that fixing the molar ratio Cr/(Fe + Cr) equal to 0.5 does not eliminate a degree of freedom since this composition variable applies to the entire system, not to any individual phase.

3.4 Thermodynamic Origin of Binary Phase Diagrams

3.4.1 Thermodynamics of Solutions

3.4.1.1 Gibbs Energy of Mixing

Liquid gold and copper are completely miscible at all compositions. The Gibbs energy of 1 mol of liquid solution, g^{l} at 1100 °C is drawn in Figure 12 as a function of composition expressed as *mole fraction*, X_{Cu}, of copper. Note that $X_{Au} = 1 - X_{Cu}$. The curve of g^{l} varies between the standard molar Gibbs energies of pure liquid Au and Cu, g^{o}_{Au} and g^{o}_{Cu}. From Eqn 65, it follows that, for a pure component, g^{o}_i and μ^{o}_i are identical.

The function $\Delta g^{\text{l}}_{\text{m}}$ shown in Figure 12 is called the molar *Gibbs energy of mixing* of the liquid solution. It is defined as

$$\Delta g^{\text{l}}_{\text{m}} = g^{\text{l}} - \left(X_{Au}\mu^{\text{o}}_{Au} + X_{Cu}\mu^{\text{o}}_{Cu}\right) \tag{88}$$

It can be seen that $\Delta g^{\text{l}}_{\text{m}}$ is the Gibbs energy change associated with the isothermal mixing of X_{Au} moles of pure liquid Au and X_{Cu} moles of pure liquid Cu to form 1 mol of solution according to the reaction:

$$X_{Au}\text{Au(liq)} + X_{Cu}\text{Cu(liq)} = 1 \text{ mole liquid solution} \tag{89}$$

Note that for the solution to be stable, it is necessary that $\Delta g^{\text{l}}_{\text{m}}$ be negative.

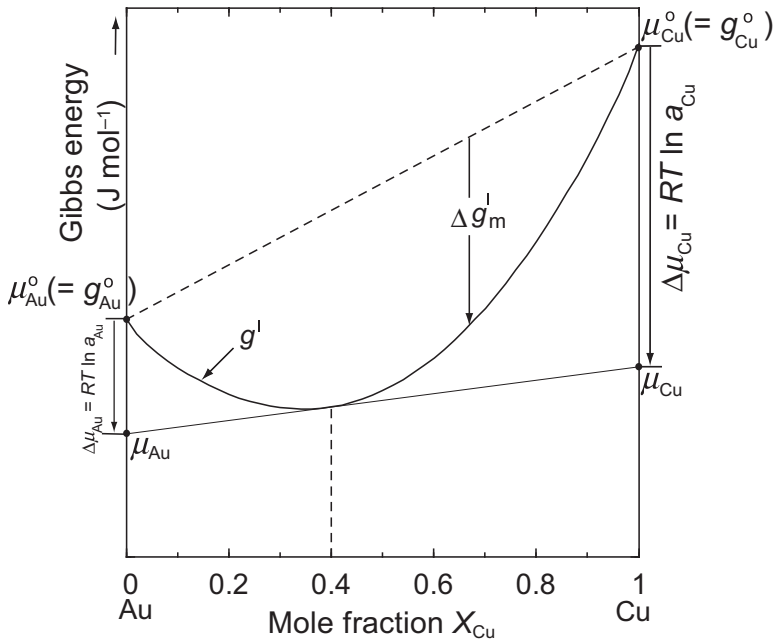

Figure 12 Molar Gibbs energy of liquid Au–Cu alloys at 1100 °C illustrating the tangent construction (see FactSage).

3.4.1.2 Tangent Construction

An important construction is illustrated in **Figure 12**. If a tangent is drawn to the curve of g^{l} at a certain composition ($X_{Cu} = 0.4$ in **Figure 12**), then the intercepts of this tangent on the axes at $X_{Au} = 1$ and $X_{Cu} = 1$ are equal to μ_{Au} and μ_{Cu}, respectively, at this composition.

To prove this, divide Eqns 64 and 73 by $(n_{Au} + n_{Cu})$ at constant T and P to obtain expressions for the molar Gibbs energy and its derivative:

$$g^{l} = X_{Au}\mu_{Au} + X_{Cu}\mu_{Cu} \tag{90}$$

and

$$dg^{l} = \mu_{Au}dX_{Au} + \mu_{Cu}dX_{Cu} \tag{91}$$

Since $dX_{Au} = -dX_{Cu}$, it can be seen that Eqns 90 and 91 are equivalent to the tangent construction shown in **Figure 12**.

These equations may also be rearranged to give the following useful expression for a binary system:

$$\mu_i = g + (1 - X_i)dg/dX_i \tag{92}$$

3.4.1.3 Relative Partial Properties

The difference between the chemical potential μ_i (also called the partial Gibbs energy g_i) of a component in solution and the chemical potential μ_i° (or g_i°) of the same component in a *standard state* is

called the *relative chemical potential* (or *relative partial Gibbs energy*), $\Delta\mu_i$ (or Δg_i). It is usual to choose, as standard state, the pure component in the same phase at the same temperature. *The activity a_i of the component relative to the chosen standard state* is then defined in terms of $\Delta\mu_i$ by the following equation, as illustrated in **Figure 12**.

$$\Delta\mu_i = \mu_i - \mu_i^{\circ} = RT \ln\ a_i \tag{93}$$

From **Figure 12**, it can be seen that

$$\Delta g_m = X_{Au}\Delta\mu_{Au} + X_{Cu}\Delta\mu_{Cu} = RT(X_{Au}\ln\ a_{Au} + X_{Cu}\ln\ a_{Cu}) \tag{94}$$

The isothermal Gibbs energy of mixing can be divided into enthalpy and entropy terms, as can be the relative chemical potentials:

$$\Delta g_m = \Delta h_m - T\Delta s_m \tag{95}$$

$$\Delta\mu_i = \Delta h_i - T\Delta s_i \tag{96}$$

where Δh_m and Δs_m are the enthalpy and entropy changes associated with the isothermal mixing reaction shown in Eqn 89. It follows from Eqns 94–96 that

$$\Delta h_m = X_{Au}\Delta h_{Au} + X_{Cu}\Delta h_{Cu} \tag{97}$$

$$\Delta s_m = X_{Au}\Delta s_{Au} + X_{Cu}\Delta s_{Cu} \tag{98}$$

and so, tangent constructions similar to that of **Figure 12** can be used to relate the *relative partial enthalpies and entropies* Δh_i and Δs_i to the *integral molar enthalpy of mixing* Δh_m and *integral molar entropy of mixing* Δs_m, respectively.

3.4.1.4 Activity

The activity of a component in a solution was defined in Eqn 93. Since a_i varies monotonically with μ_i, it follows that *when two or more phases are in equilibrium, the activity of any component is the same in all phases*, provided that the activity in every phase is expressed with respect to the same standard state.

The use of activities in calculations of chemical equilibrium conditions is illustrated by the following example. A liquid solution of Au and Cu at 1100 °C with $X_{Cu} = 0.6$ is exposed to an atmosphere, in which the oxygen partial pressure is $p_{O_2} = 10^{-3}$ bar. Will Cu_2O be formed? The reaction is

$$2Cu(liq) + 1/_2O_2(g) = Cu_2O(sol) \tag{99}$$

where the Cu(liq) is in solution. If the reaction proceeds with the formation of dn moles of Cu_2O, then 2dn moles of Cu are consumed, and the Gibbs energy of the Au–Cu solution changes by $-2(dG^{l}/dn_{Cu})\,dn$. The total Gibbs energy then varies as

$$\begin{aligned} dG/dn &= \mu^{o}_{Cu_2O} - 1/_2\,\mu_{O_2} - 2(dG^{l}/dn_{Cu}) \\ &= \mu^{o}_{Cu_2O} - 1/_2\,\mu_{O_2} - 2\mu_{Cu} \\ &= (\mu^{o}_{Cu_2O} - 1/_2\,\mu^{o}_{O_2} - 2\mu^{o}_{Cu}) - 1/_2 RT\ln\ p_{O_2} - 2\ RT\ln\ a_{Cu} \\ &= \Delta G^{o} + RT\ln\left(p_{O_2}^{-1/2}\ a_{Cu}^{-2}\right) = \Delta G \end{aligned} \tag{100}$$

where Eqns 65,86 and 93 have been used.

For reaction shown in Eqn 99 at 1100 °C, $\Delta G^{o} = -68.73$ kJ (from FactSage—see list of websites at the end of this chapter). The activity of Cu in the liquid alloy at $X_{Cu} = 0.6$ is $a_{Cu} = 0.385$ (from FactSage). Substitution into Eqn 100 with $p_{O_2} = 10^{-3}$ bar gives

$$dG/dn = \Delta G = -7.50\ \text{kJ} \tag{101}$$

Hence, under these conditions, the reaction entails a decrease in the total Gibbs energy and so the copper will be oxidized.

3.4.1.5 Ideal Raoultian Solutions

An *ideal solution* or *Raoultian solution* is usually defined as one in which the activity of a component is equal to its mole fraction:

$$a_i^{ideal} = X_i \tag{102}$$

(With a judicious choice of standard state, this definition can also encompass ideal Henrian solutions, as discussed in Section 3.5.8.)

This Raoultian definition of ideality is generally only applicable to simple substitutional solutions. There are more useful definitions for other types of solutions such as interstitial solutions, ionic solutions, solutions of defects, polymer solutions, etc. That is, the most convenient definition of ideality depends upon the solution model. Solution models are discussed in Section 3.8.2. In the present section, Eqn 102 for an ideal substitutional solution will be developed with the Au–Cu solution as example.

In the ideal substitutional solution model, it is assumed that Au and Cu atoms are nearly alike, with nearly identical radii and electronic structures. This being the case, there will be no change in bonding energy or volume upon mixing, so that the enthalpy of mixing is zero:

$$\Delta h_m^{ideal} = 0 \tag{103}$$

Furthermore, and for the same reason, the Au and Cu atoms will be randomly distributed over the lattice sites. (In the case of a liquid solution, we can think of the lattice sites as the instantaneous atomic positions.) For a random distribution of N_{Au} gold atoms and N_{Cu} copper atoms over $(N_{Au} + N_{Cu})$ sites, Boltzmann's equation (Eqn 2) can be used to calculate the *configurational entropy* of the solution. This is the entropy associated with the spatial distribution of the particles:

$$S^{config} = k_B \ln(N_{Au} + N_{Cu})!/N_{Au}!\ N_{Cu}! \tag{104}$$

The configurational entropies of pure Au and Cu are zero. Hence, the configurational entropy of mixing, ΔS_m^{config}, will be equal to S^{config}. Furthermore, because of the assumed close similarity of Au and Cu, there will be no nonconfigurational contribution to the entropy of mixing. Hence, the entropy of mixing will be equal to S^{config}. Applying Stirling's approximation, which states that $\ln N! \approx [(N \ln N)–N]$ if N is large, yields

$$\Delta S_m^{ideal} = S^{config} = -k_B\left[N_{Au}\ln\frac{N_{Au}}{N_{Au}+N_{Cu}} + N_{Cu}\ln\frac{N_{Cu}}{N_{Au}+N_{Cu}}\right] \tag{105}$$

For 1 mol of solution, $(N_{Au} + N_{Cu}) = N^o$ where N° = Avogadro's number. We also note that $(k_B N^o)$ is equal to the ideal gas constant R. Hence,

$$\Delta s_m^{ideal} = -R(X_{Au}\ln X_{Au} + X_{Cu}\ln X_{Cu}) \tag{106}$$

Therefore, since the ideal enthalpy of mixing is zero,

$$\Delta g_m^{ideal} = RT(X_{Au}\ln X_{Au} + X_{Cu}\ln X_{Cu}) \tag{107}$$

By comparing Eqns 94 and 107, we obtain

$$\Delta\mu_i^{ideal} = RT\ln a_i^{ideal} = RT\ln X_i \tag{108}$$

Hence, Eqn 102 has been demonstrated for an ideal substitutional solution.

3.4.1.6 Excess Properties

In reality, Au and Cu atoms are not identical, and so, Au–Cu solutions are not perfectly ideal. The difference between a solution property and its value in an ideal solution is called an *excess property*. The *excess Gibbs energy*, for example, is defined as

$$g^E = \Delta g_m - \Delta g_m^{ideal} \tag{109}$$

Since the ideal enthalpy of mixing is zero, the excess enthalpy is equal to the enthalpy of mixing:

$$h^E = \Delta h_m - \Delta h_m^{ideal} = \Delta h_m \tag{110}$$

Hence,

$$g^E = h^E - Ts^E = \Delta h_m - Ts^E \tag{111}$$

Excess partial properties are defined similarly:

$$\mu_i^E = \Delta\mu_i - \Delta\mu_i^{ideal} = RT\ln a_i - RT\ln X_i \tag{112}$$

$$s_i^E = \Delta s_i - \Delta s_i^{ideal} = \Delta s_i + R\ln X_i \tag{113}$$

(where μ_i^E is equivalent to g_i^E). Also,

$$\mu_i^E = h_i^E - Ts_i^E = \Delta h_i - Ts_i^E \tag{114}$$

Equations analogous to Eqns 94, 97 and 98 relate the integral and partial excess properties. For example, in Au–Cu solutions,

$$g^E = X_{Au}\ \mu_{Au}^E + X_{Cu}\ \mu_{Cu}^E \quad \text{and} \quad s^E = X_{Au}\, s_{Au}^E + X_{Cu}\, s_{Cu}^E \tag{115}$$

Tangent constructions similar to that of **Figure 12** can thus also be employed for excess properties, and an equation analogous to Eqn 92 can be written as

$$\mu_i^E = g^E + (1 - X_i)\mathrm{d}g^E/\mathrm{d}X_i \tag{116}$$

The Gibbs–Duhem Eqn 75 also applies to excess properties. At constant T and P,

$$X_{Au}\ \mathrm{d}\mu_{Au}^E + X_{Cu}\ \mathrm{d}\mu_{Cu}^E = 0 \tag{117}$$

In Au–Cu alloys, g^E is negative. That is, Δg_m is more negative than Δg_m^{ideal} and so, the solution is thermodynamically more stable than an ideal solution. We thus say that Au–Cu solutions exhibit *negative deviations from ideality*. If $g^E > 0$, then a solution is less stable than an ideal solution and is said to exhibit *positive deviations*.

3.4.1.7 Activity Coefficients

The *activity coefficient* of a component in a solution is defined as

$$\gamma_i = a_i/X_i \tag{118}$$

Hence, from Eqn 112,

$$\mu_i^E = RT \ln \gamma_i \tag{119}$$

In an ideal solution, $\gamma_i = 1$ and $\mu_i^E = 0$ for all components. If $\gamma_i < 1$, then $\mu_i^E < 0$ and from Eqn 112, $\Delta\mu_i < \Delta\mu_i^{ideal}$. That is, the component i is more stable in the solution than it would be in an ideal solution of the same composition. If $\gamma_i > 1$, then $\mu_i^E > 0$ and the driving force for the component to enter into solution is less than in the case of an ideal solution.

3.4.1.8 Multicomponent Solutions

The equations of this section were derived with a binary solution as an example. However, the equations apply equally to systems of any number of components. For instance, in a solution of components A–B–C–D…, Eqn 94 becomes

$$\Delta g_m = X_A \Delta\mu_A + X_B \Delta\mu_B + X_C \Delta\mu_C + \ldots \tag{120}$$

3.4.2 Binary Temperature-Composition Phase Diagrams

In this section, we first consider the thermodynamic origin of simple "lens-shaped" phase diagrams in binary systems with complete liquid and solid miscibility. An example of such a diagram was given in **Figure 11**. Another example is the Ge–Si phase diagram in the lowest panel of **Figure 13**. In the upper

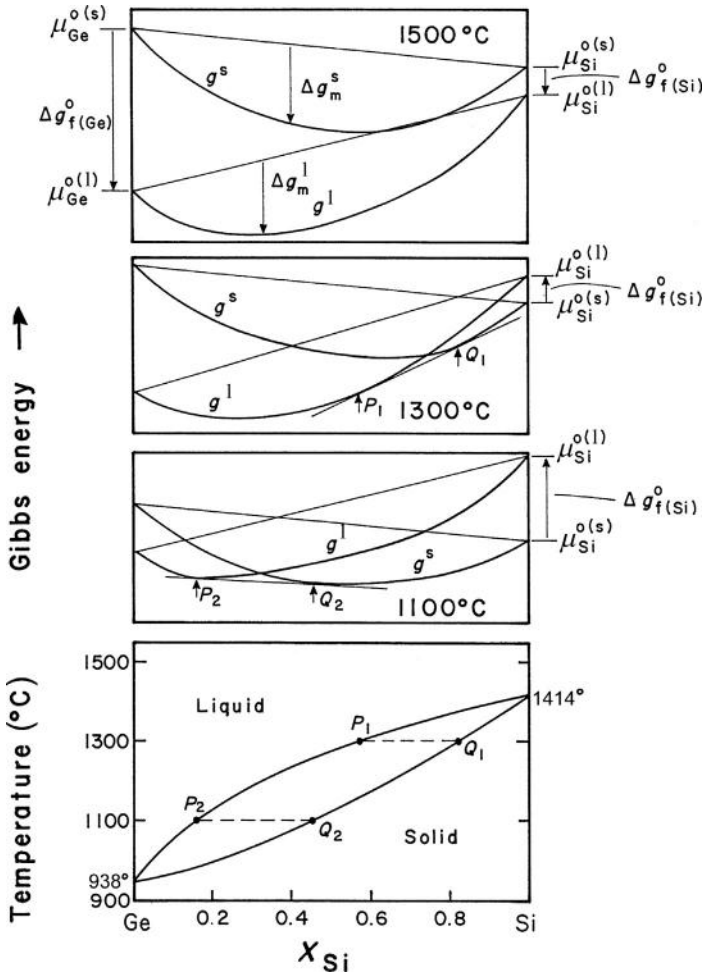

Figure 13 Ge–Si phase diagram at $P = 1$ bar (after Hansen, 1958) and Gibbs energy curves at three temperatures, illustrating the common tangent construction.

three panels of **Figure 13**, the molar Gibbs energies of the solid and liquid phases, g^{s} and g^{l} at three temperatures are shown to scale. As illustrated in the top panel, g^{s} varies with composition between the standard chemical potentials of pure solid Ge and of pure solid Si, $\mu_{Ge}^{o(s)}$ and $\mu_{Si}^{o(s)}$, while g^{l} varies between the standard chemical potentials of the pure liquid components, $\mu_{Ge}^{o(l)}$ and $\mu_{Si}^{o(l)}$. The difference between $\mu_{Ge}^{o(l)}$ and $\mu_{Ge}^{o(s)}$ is equal to the standard molar Gibbs energy of fusion (melting) of pure Ge, $\Delta g_{f\,(Ge)}^{o} = (\mu_{Ge}^{o(l)} - \mu_{Ge}^{o(s)})$. Similarly for Si, $\Delta g_{f\,(Si)}^{o} = (\mu_{Si}^{o(l)} - \mu_{Si}^{o(s)})$. The Gibbs energy of fusion of a pure component may be written as

$$\Delta g_{f}^{o} = \Delta h_{f}^{o} - T\Delta s_{f}^{o} \tag{121}$$

where Δh_{f}^{o} and Δs_{f}^{o} are the standard molar enthalpy and entropy of fusion.

Since, to a first approximation, Δh_f^o and Δs_f^o are independent of T, Δg_f^o is approximately a linear function of T. If $T > T_f^o$, then Δg_f^o is negative. If $T < T_f^o$, then Δg_f^o is positive. Hence, as seen in **Figure 13**, as T decreases, the g^s curve descends relative to g^l. At 1500 °C, $g^l < g^s$ at all compositions. Therefore, by the principle that a system always seeks the state of minimum Gibbs energy at constant T and P, the liquid phase is stable at all compositions at 1500 °C.

At 1300 °C, the curves of g^s and g^l cross. The line P_1Q_1, which is the *common tangent* to the two curves, divides the composition range into three sections. For compositions between pure Ge and P_1, a single-phase liquid is the state of minimum Gibbs energy. For compositions between Q_1 and pure Si, a single-phase solid solution is the stable state. Between P_1 and Q_1, a total Gibbs energy lying on the tangent line P_1Q_1 may be realized if the system adopts a state consisting of two phases with compositions at P_1 and Q_1 with relative proportions given by the lever rule (Section 3.3.1). Since the tangent line P_1Q_1 lies below both g^s and g^l, this two-phase state is more stable than either phase alone. Furthermore, no other line joining any point on the g^l curve to any point on the g^s curve lies below the line P_1Q_1. Hence, this line represents the true equilibrium state of the system, and the compositions P_1 and Q_1 are the liquidus and solidus compositions at 1300 °C.

As T is decreased to 1100 °C, the points of common tangency are displaced to higher concentrations of Ge. For $T < 938$ °C, $g^s < g^l$ at all compositions.

It was shown in **Figure 12** that if a tangent is drawn to a Gibbs energy curve, then the intercept of this tangent on the axis at $X_i = 1$ is equal to the chemical potential μ_i of component i. The *common tangent construction* of **Figure 13** thus ensures that the chemical potentials of Ge and Si are equal in the solid and liquid phases at equilibrium. That is,

$$\mu_{Ge}^l = \mu_{Ge}^s \tag{122}$$

$$\mu_{Si}^l = \mu_{Si}^s \tag{123}$$

This equality of chemical potentials was shown in Section 3.2.7 to be the criterion for phase equilibrium. That is, the common tangent construction simultaneously minimizes the total Gibbs energy and ensures the equality of the chemical potentials, thereby showing that these are equivalent criteria for equilibrium between phases as was discussed in Section 3.2.7.

If we rearrange Eqn 122, subtracting the Gibbs energy of fusion of pure Ge, $\Delta g_{f\ (Ge)}^o = \left(\mu_{Ge}^{o(l)} - \mu_{Ge}^{o(s)}\right)$, from each side, we obtain

$$\left(\mu_{Ge}^l - \mu_{Ge}^{o(l)}\right) - \left(\mu_{Ge}^s - \mu_{Ge}^{o(s)}\right) = -\left(\mu_{Ge}^{o(l)} - \mu_{Ge}^{o(s)}\right) \tag{124}$$

Using Eqn 93, we can write Eqn 124 as

$$\Delta\mu_{Ge}^l - \Delta\mu_{Ge}^s = -\Delta g_{f(Ge)}^o \tag{125}$$

or

$$RT \ln a_{Ge}^l - RT \ln a_{Ge}^s = -\Delta g_{f(Ge)}^o \tag{126}$$

where a_{Ge}^l is the activity of Ge (with respect to pure liquid Ge as standard state) in the liquid solution on the liquidus, and a_{Ge}^s is the activity of Ge (with respect to pure solid Ge as standard state) in the solid

solution on the solidus. Starting with Eqn 123, we can derive a similar expression for the other component:

$$RT \ln a_{Si}^{l} - RT \ln a_{Si}^{s} = -\Delta g_{f(Si)}^{o} \tag{127}$$

Equations 126 and 127 are equivalent to the common tangent construction.

It should be noted that absolute values of chemical potentials cannot be defined. Hence, the relative positions of $\mu_{Ge}^{o(l)}$ and $\mu_{Si}^{o(l)}$ in **Figure 13** are arbitrary. However, this is immaterial for the preceding discussion since displacing both $\mu_{Si}^{o(l)}$ and $\mu_{Si}^{o(s)}$ by the same arbitrary amount relative to $\mu_{Ge}^{o(l)}$ and $\mu_{Ge}^{o(s)}$ will not alter the compositions of the points of common tangency.

The shape of the two-phase (solid + liquid) "lens" on the phase diagram is determined by the Gibbs energies of fusion, Δg_f^o, of the components and by the mixing terms, Δg^s and Δg^l. In order to observe how the shape is influenced by varying Δg_f^o, let us consider a hypothetical system A–B in which Δg^s and Δg^l are ideal Raoultian (Eqn 107). Let $T_{f(A)}^o = 800$ K and $T_{f(B)}^o = 1200$ K. Furthermore, assume that the entropies of fusion of A and B are equal and temperature-independent. The enthalpies of fusion are then given from Eqn 121 by the expression $\Delta h_f^o = T_f^o \Delta s_f^o$ since $\Delta g_f^o = 0$ when $T = T_f^o$ (Section 3.2.3). Calculated phase diagrams for $\Delta s_f^o = 3,\ 10$ and 30 J mol^{-1} K^{-1} are shown in **Figure 14**. A value of $\Delta s_f^o \approx 10$ J mol^{-1} K^{-1} is typical of most metals. When the components are ionic compounds such as ionic oxides, halides, etc., Δs_f^o can be significantly larger since there are several ions per formula unit. Hence, two-phase "lenses" in binary ionic salt or oxide phase diagrams tend to be wider than those encountered in alloy systems. If we are considering vapor–liquid equilibria rather than solid–liquid equilibria, then the shape is determined by the entropy of vaporization, Δs_v^o. Since Δs_v^o is usually an order of magnitude larger than Δs_f^o, two-phase (liquid + vapor) lenses tend to be very wide. For equilibria between two solid solutions of different crystal structure, the shape is determined by the entropy of solid–solid transformation, which is usually smaller than the entropy of fusion by approximately an order of magnitude. Therefore, two-phase (solid + solid) lenses tend to be narrow.

3.4.2.1 Effect of Grain Size and Strain Energy

The foregoing phase diagram calculations have assumed that the grain size of the solid phases is sufficiently large, so that surface (interfacial) energy contributions to the Gibbs energy can be neglected. It has also been assumed that strain energy is negligible. For very fine grain sizes in the submicron range, however, the interfacial energy can be appreciable and can have an influence on the phase diagram. This effect can be important with the development of materials with grain sizes in the nanometer range.

Interfacial and strain energies increase the Gibbs energy of a phase, and hence, decrease its thermodynamic stability. In particular, the liquidus temperature of a fine-grained solid will be lowered. If a suitable estimate can be made for the grain boundary or strain energies, then this can simply be added to the Gibbs energy expression of the phase for purposes of calculating phase diagrams.

3.4.3 Binary Pressure-Composition Phase Diagrams

Let us consider liquid–vapor equilibrium in a system with complete liquid miscibility, using, as example, the Zn–Mg system. Curves of g^v and g^l can be drawn at any given T and P, as in the upper panel

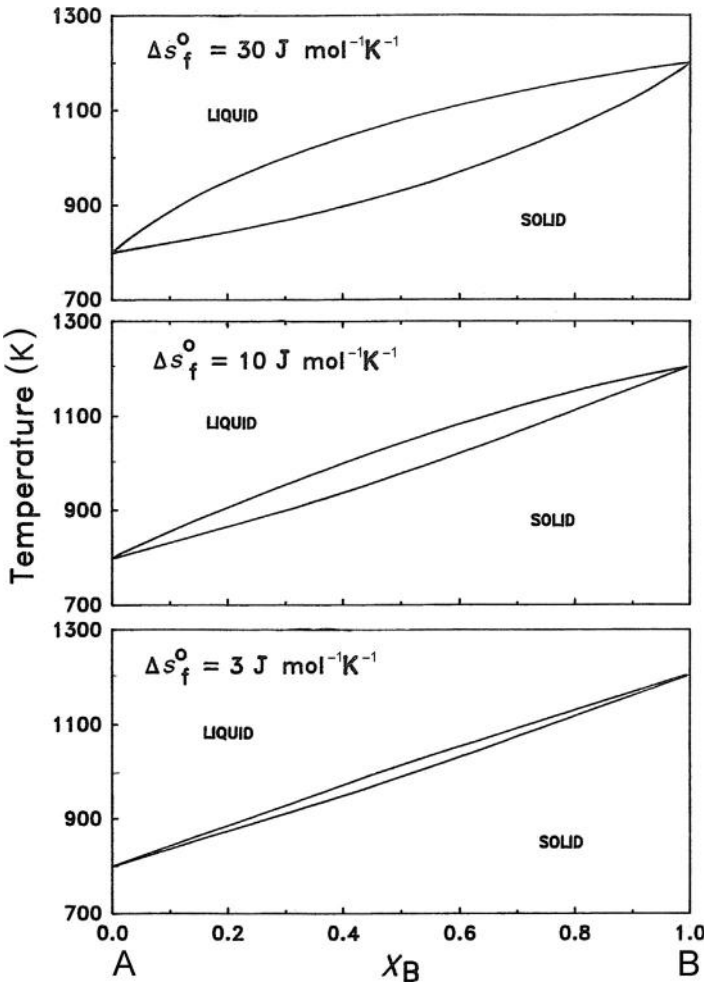

Figure 14 Phase diagram of a system A–B with ideal solid and liquid solutions. Melting points of A and B are 800 and 1200 K, respectively. Diagrams calculated for entropies of fusion $\Delta s^o_{f(A)} = \Delta s^o_{f(B)} = 3$, 10 and 30 J mol^{-1} K^{-1}.

of **Figure 15**, and the common tangent construction then gives the equilibrium vapor and liquid compositions. The phase diagram depends upon the Gibbs energies of vaporization of the pure components $\Delta g^o_{v\,(Zn)} = \left(\mu^v_{Zn} - \mu^{o(l)}_{Zn}\right)$ and $\Delta g^o_{v\,(Mg)} = \left(\mu^v_{Mg} - \mu^{o(l)}_{Mg}\right)$ as shown in **Figure 15**.

To generate the isothermal pressure-composition (P–X) phase diagram in the lower panel of **Figure 15**, we require the Gibbs energies of vaporization as functions of P. Assuming monatomic ideal vapors and assuming that pressure has negligible effect upon the Gibbs energy of the liquid, we can write, using Eqn 86:

$$\Delta g_{v(i)} = \Delta g^o_{v(i)} + RT \ln P \tag{128}$$

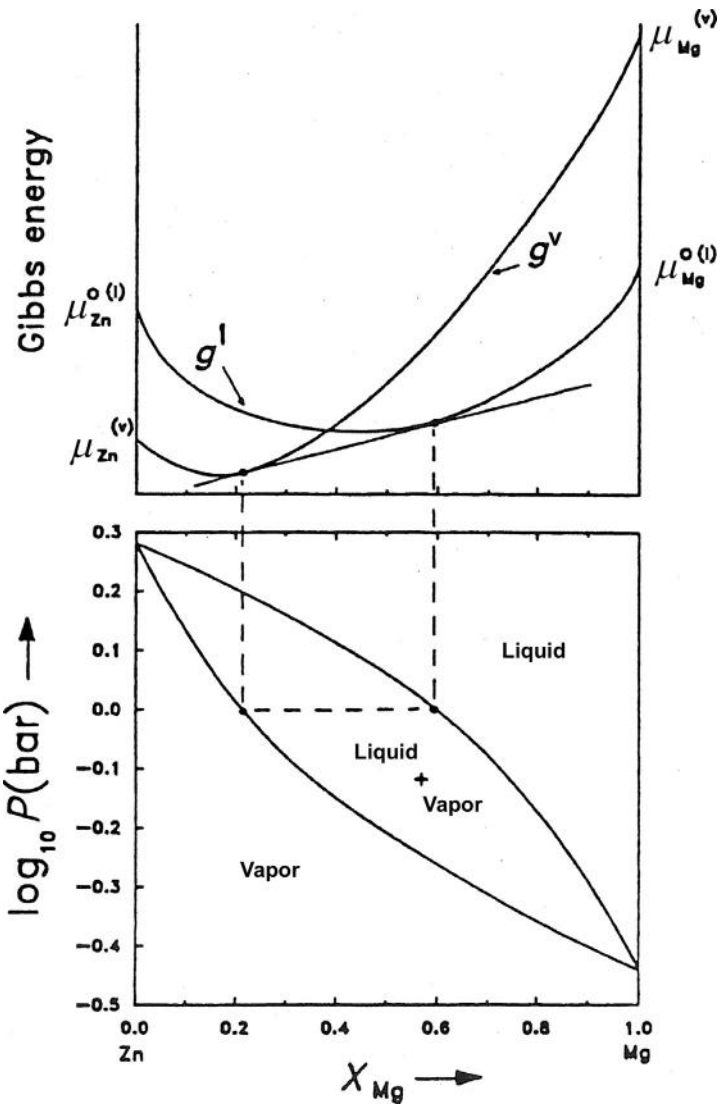

Figure 15 Pressure-composition phase diagram of the Zn–Mg system at 977 °C calculated for ideal vapor and liquid solutions. Upper panel illustrates common tangent construction at a constant pressure.

where $\Delta g^{o}_{v(i)}$ is the standard Gibbs energy of vaporization (when $P = 1.0$ bar), which is given by

$$\Delta g^{o}_{v(i)} = \Delta h^{o}_{v(i)} - T\Delta s^{o}_{v(i)} \tag{129}$$

For example, the standard enthalpy of vaporization of Zn is 115,310 J mol^{-1} at its normal boiling point of 1180 K (see FactSage). Assuming that $\Delta h^{o}_{v(Zn)}$ is independent of T, we calculate from Eqn 129

that $\Delta s^{o}_{v(Zn)} = 115310/1180 = 97.71\ \text{J mol}^{-1}\ \text{K}^{-1}$. From Eqn 128, $\Delta g_{v(Zn)}$ at any T and P is thus given by

$$\Delta g_{v(Zn)} = (115310 - 97.71\ T) + RT \ln P \tag{130}$$

A similar expression can be derived for the other component, Mg.

At constant temperature then, the curve of g^{v} in **Figure 15** descends relative to g^{l} as the pressure is lowered, and the P–X phase diagram is generated by the common tangent construction. The diagram at 977 °C in **Figure 15** was calculated under the assumption of ideal liquid and vapor mixing ($g^{E(l)} = 0,\ g^{E(v)} = 0$).

P–X phase diagrams involving liquid–solid and solid–solid equilibria can be calculated in a similar manner through the following general equation, which follows from Eqn 64 and which gives the effect of pressure upon the Gibbs energy change for the transformation of 1 mol of pure component i from an α-phase to a β-phase at constant T:

$$\Delta g_{(i)\alpha\rightarrow\beta} = \Delta g^{o}_{(i)\alpha\rightarrow\beta} + \int_{P=1}^{P} \left(v_i^{\beta} - v_i^{\alpha}\right) dP \tag{131}$$

where $\Delta g^{o}_{(i)\alpha\rightarrow\beta}$ is the standard ($P = 1.0$ bar) Gibbs energy of transformation, and v_i^{β} and v_i^{α} are the molar volumes.

3.5 Binary Temperature-Composition Phase Diagrams

3.5.1 Systems with Complete Solid and Liquid Miscibility

Examples of phase diagrams of such systems were given in **Figures 11 and 13** and discussed in Sections 3.3.1 and 3.4.2.

3.5.2 Minima and Maxima in Two-Phase Regions

As discussed in Section 3.4.1.6, the Gibbs energy of mixing Δg_m may be expressed as the sum of an ideal term Δg_m^{ideal} and an excess term g^{E}. As shown in Section 3.4.2, if the solid and liquid phases are both ideal, or close to ideal, a "lens-shaped" two-phase region results. However, in most systems, even approximately ideal behavior is the exception rather than the rule.

Curves of g^{s} and g^{l} for a hypothetical system A–B are shown schematically in **Figure 16** at a constant temperature (below the melting points of pure A and B) such that the solid state is the stable state for both pure components. However, in this system, $g^{E(l)} < g^{E(s)}$ so that g^{s} presents a flatter curve than does g^{l} and there exists a central composition region in which $g^{l} < g^{s}$. Hence, there are two common tangent lines, P_1Q_1 and P_2Q_2. Such a situation gives rise to a phase diagram with a minimum in the two-phase region as observed in the quasibinary Na_2CO_3–K_2CO_3 system shown in **Figure 17**. At a composition and temperature corresponding to the minimum point, liquid and solid of the same composition exist in equilibrium.

A two-phase region with a minimum point as shown in **Figure 17** may be thought of as a two-phase "lens" which has been "pushed down" by virtue of the fact that the liquid is relatively more stable than the solid. Thermodynamically, this relative stability is expressed as $g^{E(l)} < g^{E(s)}$.

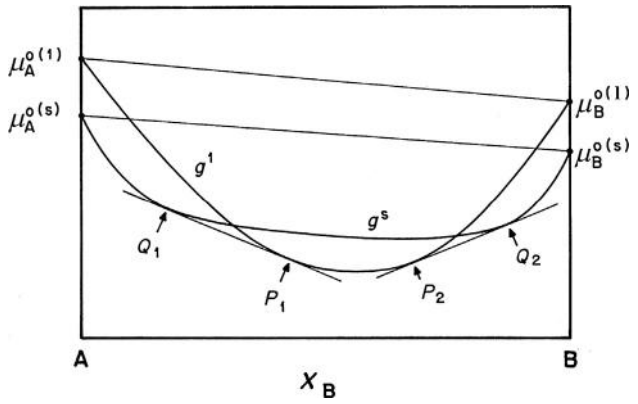

Figure 16 Isothermal Gibbs energy curves for solid and liquid phases in a system A–B, in which $g^{E(l)} < g^{E(s)}$. A phase diagram of the type of **Figure 17** results.

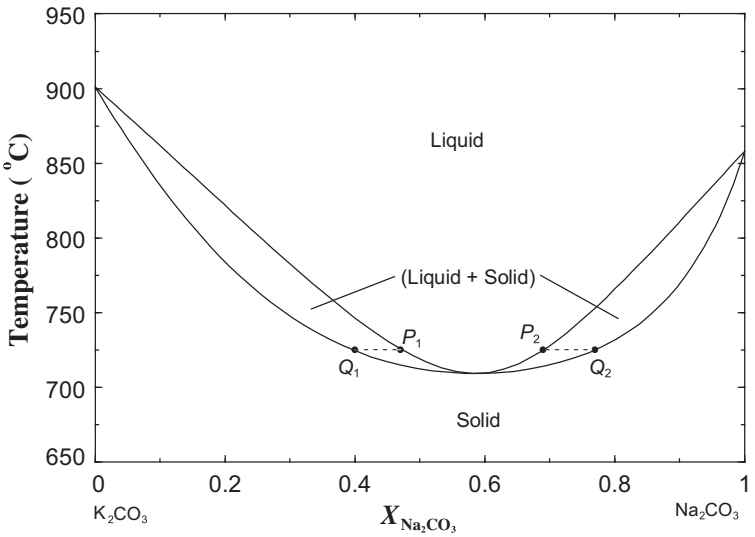

Figure 17 Temperature-composition phase diagram of the K_2CO_3–Na_2CO_3 system at $P = 1$ bar (see FactSage).

Conversely, if $g^{E(l)} > g^{E(s)}$ to a sufficient extent, then a two-phase region with a maximum will result. Such maxima in (liquid + solid) or (solid + solid) two-phase regions are nearly always associated with the existence of an intermediate phase, as will be discussed in Section 3.5.7.

3.5.3 Miscibility Gaps

If $g^E > 0$, then the solution is thermodynamically less stable than an ideal solution. This can result from a large difference in size of the component atoms, ions or molecules; or from differences in bond types, valencies, electronic structure; or from many other factors.

In the Au–Ni system, g^{E} is positive in the solid phase. In the top panel of **Figure 18**, $g^{E(s)}$ is plotted at 1200 K (Hultgren et al., 1973) and the ideal Gibbs energy of mixing, Δg_m^{ideal}, is also plotted at 1200 K. The sum of these two terms is the Gibbs energy of mixing of the solid solution, Δg_m^{s}, which is plotted at 1200 K as well as at other temperatures in the central panel of **Figure 18**. Now, from Eqn 107, Δg_m^{ideal} is always negative and varies directly with T, whereas g^{E} generally varies less rapidly with temperature. As a result, the sum $\Delta g_m^{s} = \Delta g_m^{ideal} + g^{E}$ becomes less negative as T decreases. However, the limiting slopes to the Δg_m^{ideal} curve at $X_{Au} = 1$ and $X_{Ni} = 1$ are both infinite, whereas the limiting slopes of g^{E} are always finite (Henry's Law). Hence, Δg_m^{s} will always be negative as $X_{Au} \to 1$ and $X_{Ni} \to 1$, no matter how low the temperature. As a result, below a certain temperature, the curve of Δg_m^{s} will exhibit two negative "humps." Common tangent lines P_1Q_1, P_2Q_2, P_3Q_3 to the two humps at different temperatures define the ends of tie-lines of a two-phase solid–solid *miscibility gap* in the Au–Ni phase diagram, which is shown in the lower panel in **Figure 18** (Hultgren et al., 1973). The peak of the gap occurs at the *critical* or *consolute* temperature and composition, T_c and X_c.

An example of a miscibility gap in a liquid phase will be given in **Figure 21**.

When $g^{E(s)}$ is positive for the solid phase in a system, it is usually also the case that $g^{E(l)} < g^{(s)}$ since the unfavorable factors (such as a difference in atomic dimensions), which cause $g^{E(s)}$ to be positive, will have less of an effect upon $g^{E(l)}$ in the liquid phase owing to the greater flexibility of the liquid structure to accommodate different atomic sizes, valencies, etc. Hence, a solid–solid miscibility gap is often associated with a minimum in the two-phase (solid + liquid) region, as is the case in the Au–Ni system.

Below the critical temperature, the curve of Δg_m^{s} exhibits two inflection points, indicated by the letter *s* in **Figure 18**. These are known as the *spinodal points.* On the phase diagram, their locus traces out the *spinodal curve*. The spinodal curve is not part of the equilibrium phase diagram, but it is important in the kinetics of phase separation, as discussed in Chapter 8 of this volume.

3.5.4 Simple Eutectic Systems

The more positive g^{E} is in a system, the higher is T_c and the wider is the miscibility gap at any temperature. Suppose that $g^{E(s)}$ is so positive that T_c is higher than the minimum in the (solid + liquid) region. The result will be a phase diagram such as that of the Ag–Cu system shown in **Figure 19**. The upper panel of **Figure 19** shows the Gibbs energy curves at 850 °C. The two common tangents define two two-phase regions. As the temperature is decreased below 850 °C, the g^{s} curve descends relative to g^{l} and the two points of tangency P_1 and P_2 approach each other until, at $T = 780$ °C, P_1 and P_2 become coincident at the composition E. That is, at $T = 780$ °C, there is just one common tangent line contacting the two portions of the g^{s} curve at compositions A and B and contacting the g^{l} curve at E. This temperature is known as the *eutectic temperature*, T_E, and the composition E is the *eutectic composition*. For temperatures below T_E, g^{l} lies completely above the common tangent to the two portions of the g^{s} curve and so, for $T < T_E$, a solid–solid miscibility gap is observed. The phase boundaries of this two-phase region are called the *solvus* lines. The word eutectic is from the Greek for "to melt well," since the eutectic composition E is a minimum melting temperature.

This description of the thermodynamic origin of simple eutectic phase diagrams is strictly correct only if the pure solid components A and B have the same crystal structure. Otherwise, a curve for g^{s}, which is continuous at all compositions, cannot be drawn. In this case, each terminal solid solution (α and β) must have its own Gibbs energy curve (g^{α} and g^{β}), and these curves do not join up with each other. However, a simple eutectic phase diagram as shown in **Figure 19** still results.

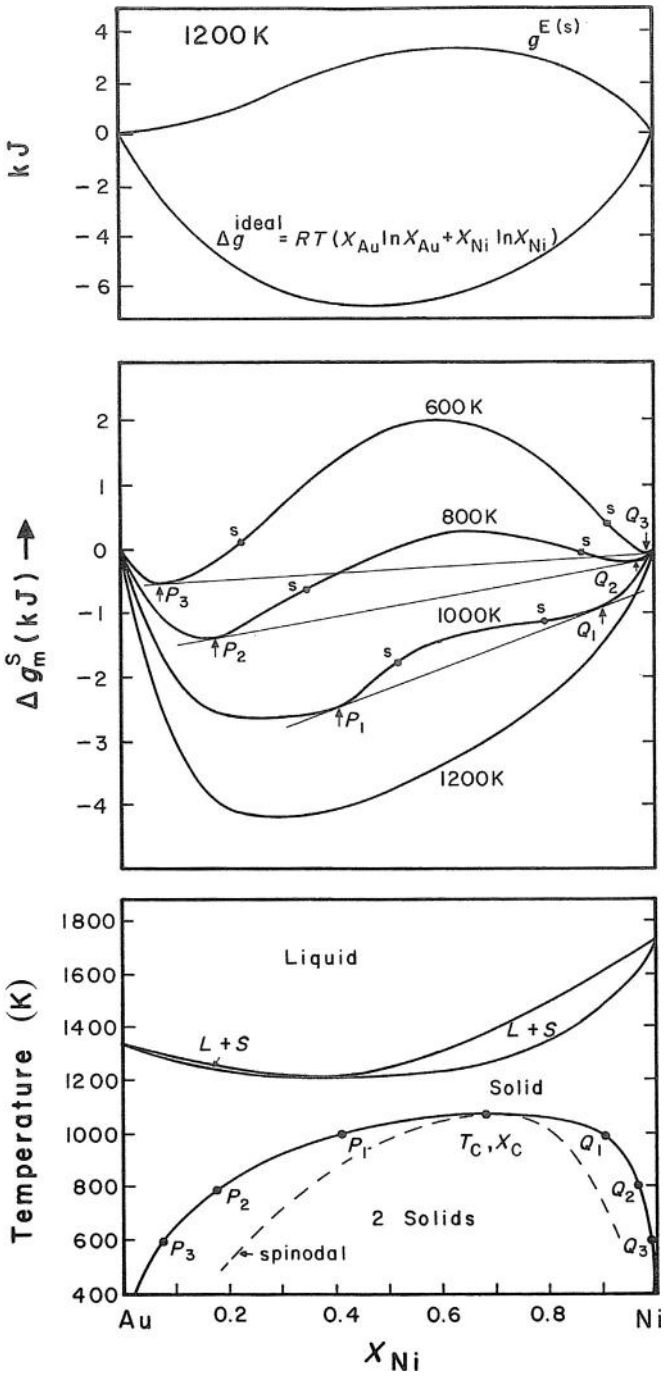

Figure 18 Phase diagram (after Hultgren et al., 1973) and Gibbs energy curves of solid solutions for the Au–Ni system at $P = 1$ bar. Letter *s* indicates spinodal points.

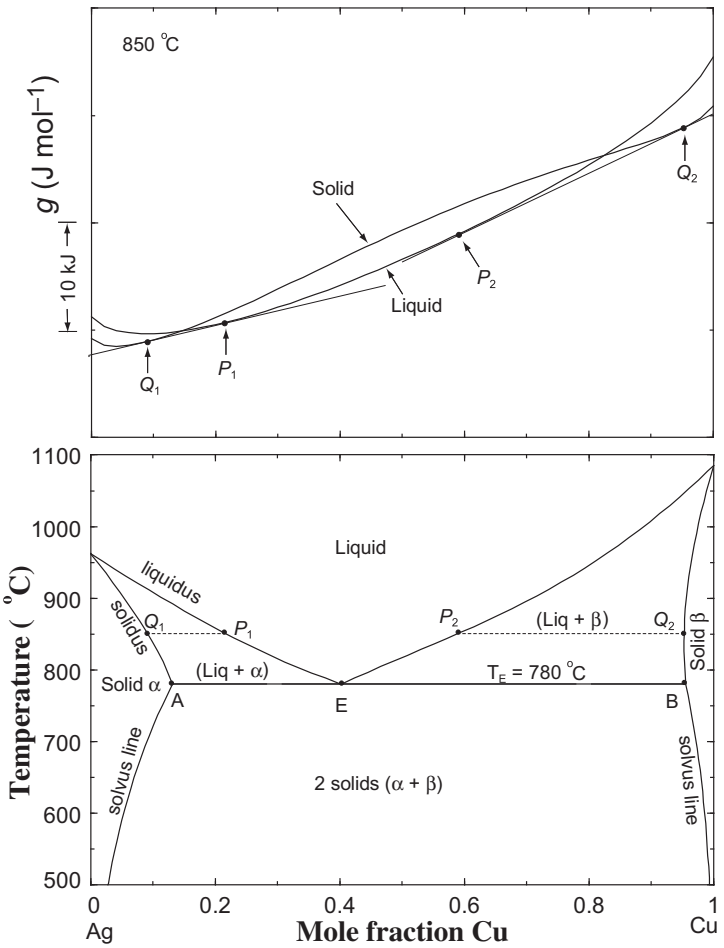

Figure 19 Temperature-composition phase diagram at $P = 1$ bar and Gibbs energy curves at 850 °C for the Ag–Cu system. Solid Ag and Cu have the same (fcc) crystal structure (see FactSage; SGTE).

Suppose a liquid Ag–Cu solution of composition $X_{Cu} = 0.22$ (composition P_1) is cooled from the liquid state very slowly under equilibrium conditions. At 850 °C, the first solid appears with composition Q_1. As T decreases further, solidification continues with the liquid composition following the liquidus curve from P_1 to E and the composition of the solid phase following the solidus curve from Q_1 to A. The relative proportions of the two phases at any T are given by the lever rule (Section 3.3.1). At a temperature just above T_E, two phases are observed: a solid of composition A and a liquid of composition E. At a temperature just below T_E, two solids with compositions A and B are observed. Therefore, at T_E, during cooling, the following *binary eutectic reaction* occurs:

$$\text{liquid} \rightarrow \alpha(\text{solid}) + \beta(\text{solid}) \tag{132}$$

Under equilibrium conditions, the temperature will remain constant at $T = T_E$ until all the liquid has solidified, and during the reaction, the compositions of the three phases will remain fixed at A, B and E.

For this reason, the eutectic reaction is called an *invariant* reaction as was discussed in Section 3.3.1.1. More on eutectic solidification may be found in Chapter 7 of this volume.

3.5.5 Regular Solution Theory

Many years ago, Van Laar (1908) showed that the thermodynamic origin of a great many of the observed features of binary phase diagrams can be illustrated at least qualitatively by simple regular solution theory. A simple *regular solution* of components A and B is one for which,

$$g^{\mathrm{E}} = X_{\mathrm{A}}X_{\mathrm{B}}(\omega - \eta T) \tag{133}$$

where ω and η are parameters independent of temperature and composition. Substituting Eqn 133 into Eqn 116 yields, for the partial properties:

$$\mu_{\mathrm{A}}^{\mathrm{E}} = X_{\mathrm{B}}^2(\omega - \eta T), \quad \mu_{\mathrm{B}}^{\mathrm{E}} = X_{\mathrm{A}}^2(\omega - \eta T) \tag{134}$$

Several liquid and solid solutions conform approximately to regular solution behavior, particularly if g^{E} is small. Examples may be found for alloys, molecular solutions, and ionic solutions such as molten salts and oxides, among others. (The very low values of g^{E} observed for gaseous solutions generally conform very closely to Eqn 133.)

To understand why this should be so, we need only a very simple model. Suppose that the atoms or molecules of the components A and B mix substitutionally. If the atomic (or molecular) sizes and electronic structures of A and B are similar, then the distribution will be nearly random, and the configurational entropy will be nearly ideal as in Eqn 106. That is,

$$g^{\mathrm{E}} = \Delta h_{\mathrm{m}} - Ts^{\mathrm{E(non\text{-}config)}} \tag{135}$$

Assuming that the bond energies $\varepsilon_{\mathrm{AA}}$, $\varepsilon_{\mathrm{BB}}$ and $\varepsilon_{\mathrm{AB}}$ of first-nearest-neighbor pairs are independent of temperature and composition and that the average nearest-neighbor coordination number, Z, is also constant, we calculate the enthalpy of mixing resulting from the change in the total energy of first-nearest-neighbor pair bonds as follows.

In 1 mol of solution, there are $(N^{\circ}Z/2)$ nearest-neighbor pair bonds, where N° is Avogadro's number. Since the distribution is assumed to be random, the probability that a given bond is an A–A bond is equal to X_{A}^2. The probabilities of B–B and A–B bonds are, respectively, X_{B}^2 and $2X_{\mathrm{A}}X_{\mathrm{B}}$. The contribution to the molar enthalpy of mixing resulting from the change in total energy of first-nearest-neighbor bonds is then equal to the sum of the energies of the first-nearest-neighbor bonds in 1 mol of solution minus the energy of the A–A bonds in X_{A} moles of pure A and the energy of the B–B bonds in X_{B} moles of pure B:

$$\begin{aligned}\Delta h^{\mathrm{FNN}} &= (N^{\mathrm{o}}Z/2)\left(X_{\mathrm{A}}^2\varepsilon_{\mathrm{AA}} + X_{\mathrm{B}}^2\varepsilon_{\mathrm{BB}} + 2X_{\mathrm{A}}X_{\mathrm{B}}\varepsilon_{\mathrm{AB}}\right) - (N^{\mathrm{o}}Z/2)(X_{\mathrm{A}}\varepsilon_{\mathrm{AA}} + X_{\mathrm{B}}\varepsilon_{\mathrm{BB}}) \\ &= (N^{\mathrm{o}}Z)[\varepsilon_{\mathrm{AA}} - (\varepsilon_{\mathrm{AA}} + \varepsilon_{\mathrm{BB}})/2]X_{\mathrm{A}}X_{\mathrm{B}} \\ &= C_1X_{\mathrm{A}}X_{\mathrm{B}}\end{aligned} \tag{136}$$

where C_1 is a constant.

With exactly the same assumptions and arguments, we can derive equations for the enthalpy of mixing contributions resulting from the change in total energy of second-nearest-neighbor, Δh^{SNN},

third-nearest-neighbor, Δh^{TNN}, etc. pair bonds. These are clearly all of the same form, $C_i X_A X_B$. If we now assume that the actual observed enthalpy of mixing Δh_m, results mainly from these changes in the total energy of all pair bonds, then

$$\Delta h_m = \omega X_A X_B \tag{137}$$

where $\omega = C_1 + C_2 + C_3 + \ldots\ldots$

If we now define σ_{AA}, σ_{BB}, and σ_{AB} as the vibrational entropies of pair bonds and follow an identical argument to that just presented for the pair bond energies, we obtain

$$s^{E(\text{non-config})} = (N^o Z/2)[\sigma_{AB} - (\sigma_{AA} + \sigma_{BB}/2)] = \eta X_A X_B \tag{138}$$

Equation 133 has thus been derived. If A–B bonds are stronger than A–A and B–B bonds, then $(\varepsilon_{AA} - \sigma_{AB}T) < [(\varepsilon_{AA} - \sigma_{AA}T)/2 + (\varepsilon_{BB} - \sigma_{BB}T)/2]$, so that $(\omega - \eta T) < 0$ and $g^E < 0$. That is, the solution is rendered more stable. If the A–B bonds are relatively weaker, then the solution is rendered less stable, $(\omega - \eta T) > 0$ and $g^E > 0$.

Simple nonpolar molecular solutions and simple ionic solutions such as molten salts often exhibit approximately regular behavior. The assumption of additivity of the energy of pair bonds is probably reasonably realistic for van der Waals or coulombic forces. For metallic alloys, the concept of a pair bond is, at best, vague, and metallic solutions tend to exhibit larger deviations from regular behavior.

In several solutions, it is found that $|\eta T| \langle |\omega|$ in Eqn 133. That is, $g^E \approx \Delta h_m = \omega X_A X_B$, and so to a first approximation, g^E is independent of T. This is more often the case in nonmetallic solutions than in metallic solutions.

3.5.5.1 Thermodynamic Origin of Simple Phase Diagrams Illustrated by Regular Solution Theory

Figure 20 shows several phase diagrams calculated for a hypothetical system A–B containing a solid and a liquid phase with melting points of $T^o_{f(A)} = 800$ K and $T^o_{f(B)} = 1200$ K and with entropies of fusion of both A and B set to 10 J mol^{-1} K^{-1} which is a typical value for metals. The solid and liquid phases are both regular with temperature-independent excess Gibbs energies

$$g^{E(s)} = \omega^s X_A X_B \quad \text{and} \quad g^{E(l)} = \omega^l X_A X_B \tag{139}$$

The parameters ω^s and ω^l have been varied systematically to generate the various panels of Figure 20.

In panel (n), both phases are ideal. Panels (l)–(r) exhibit minima or maxima depending upon the sign and magnitude of $(g^{E(l)} - g^{E(s)})$, as has been discussed in Section 3.5.2. In panel (h), the liquid is ideal but positive deviations in the solid give rise to a solid–solid miscibility gap as discussed in Section 3.5.4. On passing from panel (h) to panel (c), an increase in $g^{E(s)}$ results in a widening of the miscibility gap, so that the solubilities of A in solid B and of B in solid A decrease. Panels (a)–(c) illustrate that negative deviations in the liquid cause a relative stabilization of the liquid with resultant lowering of the eutectic temperature. Panels (d) and (e) are discussed in Section 3.5.6.

3.5.6 Immiscibility—Monotectics

In Figure 20e, positive deviations in the liquid have given rise to a *liquid–liquid miscibility* gap. The quasibinary CaO–SiO_2 system, shown in Figure 21, exhibits such a feature. Suppose that a liquid of

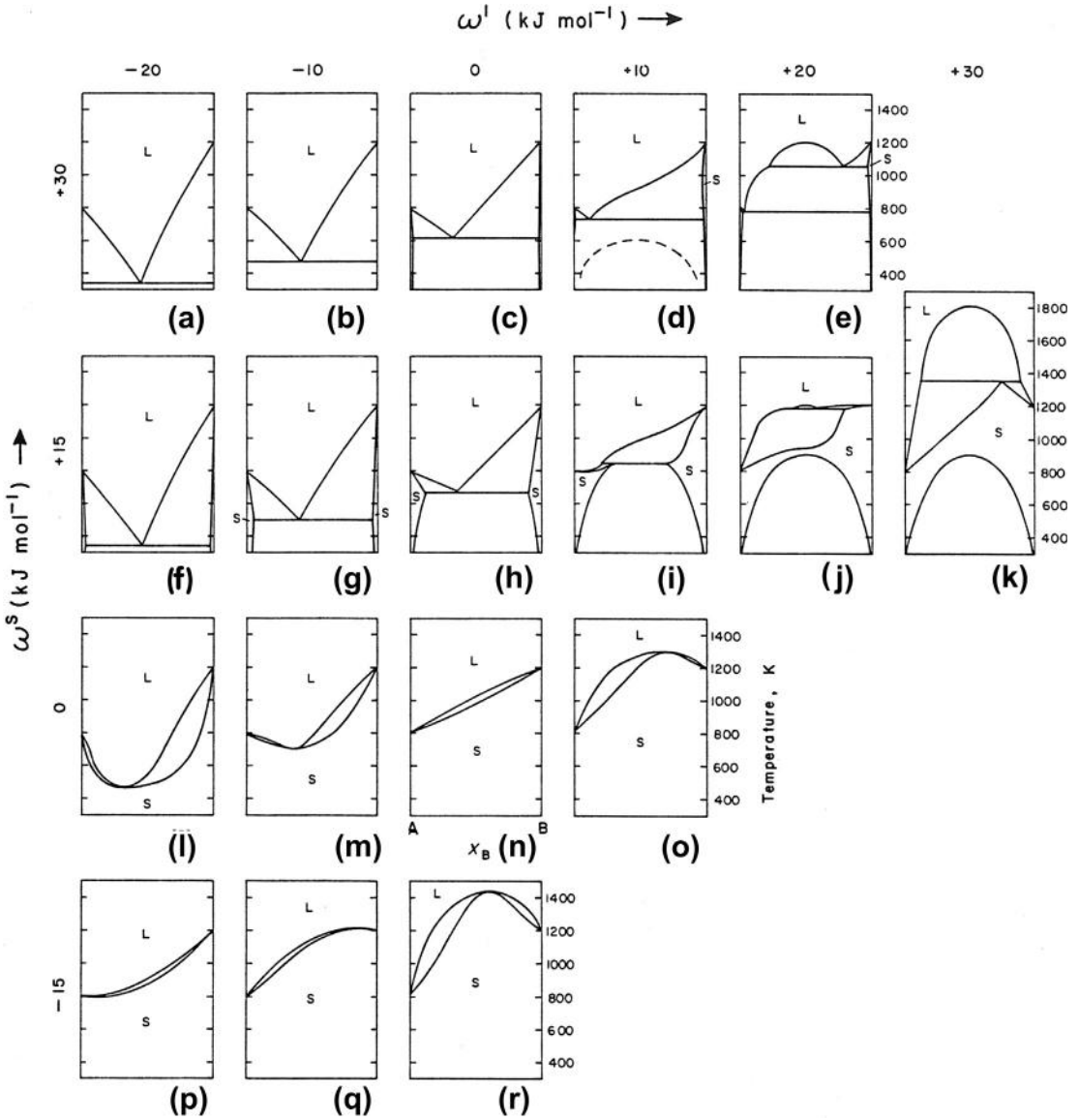

Figure 20 Topological changes in the phase diagram for a system A–B with regular solid and liquid phases brought about by systematic changes in the regular solution parameters ω^s and ω^l. Melting points of pure A and B are 800 K and 1200 K, respectively. Entropies of fusion of both A and B are 10.0 J mol^{-1} K^{-1} (Pelton and Thompson, 1975). Dashed curve in panel (d) is a metastable liquid miscibility gap.

composition $X_{SiO_2} = 0.8$ is cooled slowly from high temperatures. At $T = 1830\ ^\circ C$, the miscibility gap boundary is crossed and a second liquid layer appears with a composition of $X_{SiO_2} = 0.96$. As the temperature is lowered further, the composition of each liquid phase follows its respective phase boundary until, at 1689 °C, the SiO_2-rich liquid has a composition of $X_{SiO_2} = 0.988$ (point B), and in

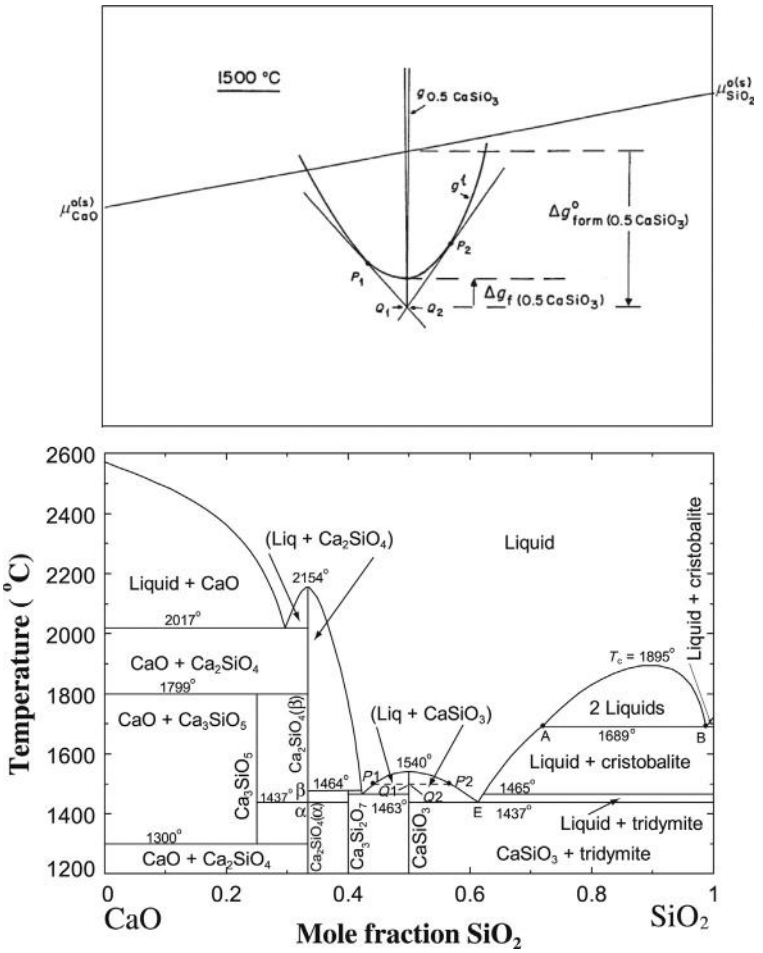

Figure 21 CaO–SiO_2 phase diagram at $P = 1$ bar and Gibbs energy curves at 1500 °C illustrating Gibbs energies of fusion and formation of the compound $CaSiO_3$ (see FactSage).(Reprinted with permission from Pelton, 2001a). The temperature difference between the peritectic at 1464 °C and the eutectic at 1463 °C has been exaggerated for the sake of clarity.

the CaO-rich liquid $X_{SiO_2} = 0.72$ (point A). At any temperature, the relative amounts of the two phases are given by the lever rule.

At 1689 °C, the following invariant *binary monotectic reaction* occurs upon cooling:

$$\text{Liquid B} \rightarrow \text{Liquid A} + SiO_2(\text{solid}) \tag{140}$$

The temperature remains constant at 1689 °C and the compositions of the phases remain constant until all of liquid B is consumed. Cooling then continues with precipitation of solid SiO_2 with the equilibrium liquid composition following the liquidus from point *A* to the eutectic *E*.

Returning to **Figure 20**, we see in panel (d) that the positive deviations in the liquid in this case are not large enough to produce immiscibility, but they do result in a flattening of the liquidus, which indicates a "tendency to immiscibility." If the nucleation of the solid phases can be suppressed by

sufficiently rapid cooling, then a *metastable liquid–liquid miscibility gap* is observed as shown in Figure 20d. For example, in the Na_2O–SiO_2 system, the flattened (or "S-shaped") SiO_2-liquidus heralds the existence of a metastable miscibility gap of importance in glass technology.

3.5.7 Intermediate Phases

The phase diagram of the Ag–Mg system (Hultgren et al., 1973) is shown in Figure 22d. An intermetallic phase, β′, is seen centered approximately about the composition $X_{Mg} = 0.5$. The Gibbs energy curve at 1050 K for such an intermetallic phase has the form shown schematically in Figure 22a. The curve $g^{\beta'}$ rises quite rapidly on either side of its minimum, which occurs near $X_{Mg} = 0.5$. As a result, the single-phase β′ region appears on the phase diagram only over a limited composition range. This form of the Gibbs energy curve results from the fact that when $X_{Ag} \approx X_{Mg}$, a particularly stable crystal structure exists in which Ag and Mg atoms preferentially occupy different sites. The two common tangents P_1Q_1 and P_2Q_2 give rise to a maximum in the two-phase (β′ + liquid) region of the phase diagram. (Although the maximum is observed very near $X_{Mg} = 0.5$, there is no thermodynamic reason for the maximum to occur exactly at this composition.)

Another intermetallic phase, the ε phase, is also observed in the Ag–Mg system (Figure 22d). The phase is associated with a *peritectic* invariant *ABC* at 744 K. The Gibbs energy curves are shown schematically at the peritectic temperature in Figure 22c. One common tangent line can be drawn to g^{l}, $g^{\beta'}$ and g^{ε} at 744 K.

Suppose that a liquid alloy of composition $X_{Mg} = 0.7$ is cooled very slowly from the liquid state. At a temperature just above 744 K, a liquid phase of composition C and a β′ phase of composition A are observed at equilibrium. At a temperature just below 744 K, the two phases at equilibrium are β′ of composition A and ε of composition B. The following invariant *binary peritectic reaction* thus occurs upon cooling:

$$\text{Liquid} + \beta' \text{ (solid)} \rightarrow \varepsilon \text{ (solid)} \tag{141}$$

This reaction occurs isothermally at 744 K with all three phases at fixed compositions (at points A, B and C). For an alloy with overall composition between points A and B, the reaction proceeds until all the liquid has been consumed. In the case of an alloy with overall composition between B and C, the β′ phase will be the first to be completely consumed.

Peritectic reactions occur upon cooling generally with formation of the product solid (ε in this example) on the surface of the reactant solid (β′), thereby forming a coating which can reduce or prevent further contact between the reactant solid and liquid. Further reaction may thus be greatly retarded, so that equilibrium conditions can only be achieved by extremely slow cooling.

The Gibbs energy curve for the ε phase, g^{ε}, in Figure 22c rises more rapidly on either side of its minimum than does the Gibbs energy $g^{\beta'}$ of the β′ phase. Consequently, the width of the single-phase region over which the ε phase exists (sometimes called its *range of stoichiometry* or *homogeneity range*) is narrower than that of the β′ phase.

In the upper panel of Figure 21 for the CaO–SiO_2 system, Gibbs energy curves at 1500 °C for the liquid and $CaSiO_3$ phases are shown schematically. $g_{0.5(CaSiO_3)}$ rises extremely rapidly on either side of its minimum. (We write $g_{0.5(CaSiO_3)}$ for 0.5 moles of the compound in order to normalize to a basis of 1 mol of components CaO and SiO_2.) As a result, the points of tangency Q_1 and Q_2 of the common tangents P_1Q_1 and P_2Q_2 nearly (although not exactly) coincide. Hence, the range of stoichiometry of the $CaSiO_3$ phase is very narrow (although never zero). The two-phase regions labeled

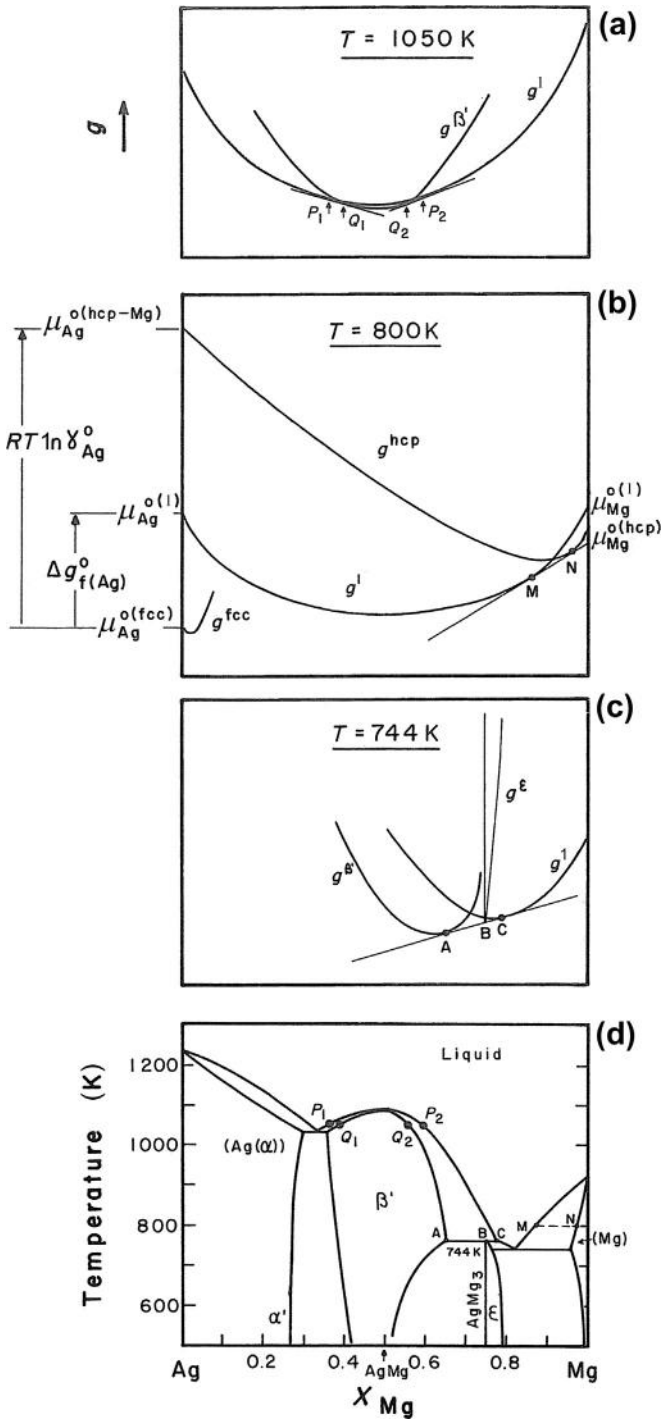

Figure 22 Ag–Mg phase diagram at $P = 1$ bar (after Hultgren et al., 1973) and Gibbs energy curves at three temperatures.

(liquid + $CaSiO_3$) in **Figure 21** are the two sides of a two-phase region that passes through a maximum at 1540 °C just as the (β′ + liquid) region passes through a maximum in **Figure 22**d. Because the $CaSiO_3$ single-phase region is extremely narrow (although always of finite width), we refer to $CaSiO_3$ as a *stoichiometric compound*. Any deviation in composition from the stoichiometric 1:1 ratio of CaO to SiO_2 results in a very large increase in its Gibbs energy.

The ε phase in **Figure 22** is based on the stoichiometry $AgMg_3$. The Gibbs energy curve (**Figure 22**c) rises extremely rapidly on the Ag side of the minimum, but somewhat less steeply on the Mg side. As a result, Ag is virtually insoluble in $AgMg_3$, while Mg is sparingly soluble. Such a phase with a narrow range of homogeneity is often called a *nonstoichiometric compound*. At low temperatures, the β′ phase exhibits a relatively narrow range of stoichiometry about the 1:1 AgMg composition and can properly be called a *compound*. However, at higher temperatures, it is debatable whether a phase with such a wide range of composition should be called a *compound*.

From **Figure 21**, it can be seen that if stoichiometric $CaSiO_3$ is heated, it will melt isothermally at 1540 °C to form a liquid of the same composition. Such a compound is called *congruently melting* or simply a *congruent compound*. The compound Ca_2SiO_4 in **Figure 21** is also congruently melting. The β′ phase in **Figure 22** is also congruently melting at the composition of the liquidus/solidus maximum.

It should be noted with regard to congruent melting that the limiting slopes dT/dX of both branches of the liquidus at the congruent melting point (that is, at the maximum of the two-phase region) are zero since we are dealing with a maximum in a two-phase region (similar to the minimum in the two-phase region in **Figure 17**).

The $AgMg_3$ (ε) compound in **Figure 22** is said to *melt incongruently*. If solid $AgMg_3$ is heated, it will melt isothermally at 744 K by the reverse of the peritectic reaction as shown in Eqn 141, to form a liquid of composition C and another solid phase, β′, of composition A.

Another example of an *incongruently melting compound* is $Ca_3Si_2O_7$ in **Figure 21**, which melts incongruently (or peritectically) to form liquid and Ca_2SiO_4 at the peritectic temperature of 1464 °C.

An incongruently melting compound is always associated with a peritectic. However, the converse is not necessarily true. A peritectic is not always associated with an intermediate phase. See, for example, **Figure 20**i.

For purposes of phase diagram calculations involving stoichiometric compounds such as $CaSiO_3$, we may, to a good approximation, consider the Gibbs energy curve, $g_{0.5(CaSiO_3)}$, in the upper panel of **Figure 21** to have zero width. All that is then required is the value of $g_{0.5(CaSiO_3)}$ at the minimum. This value is usually expressed in terms of the *Gibbs energy of fusion* of the compound, $\Delta g_{f(0.5CaSiO_3)}$ or of the *Gibbs energy of formation* $\Delta g_{form(0.5CaSiO_3)}$ of the compound from the pure solid components CaO and SiO_2 according to the reaction: 0.5 CaO (sol) + 0.5 SiO_2(sol) = 0.5 $CaSiO_3$(sol). Both these quantities are interpreted graphically in **Figure 21**.

3.5.8 Limited Mutual Solubility—Ideal Henrian Solutions

In Section 3.5.4, the region of two solids in the Ag–Cu phase diagram of **Figure 19** was described as a miscibility gap. That is, only one continuous g^s curve was assumed. If, somehow, the appearance of the liquid phase could be suppressed, the two solvus lines in **Figure 19**, when projected upward, would meet at a critical point, above which one continuous solid solution would exist at all compositions.

Such a description is justifiable only if the pure solid components have the same crystal structure, as is the case for Ag and Cu. However, consider the Ag–Mg system (**Figure 22**), in which the terminal (Ag) solid solution is face-centered-cubic (fcc) and the terminal (Mg) solid solution is

hexagonal-close-packed (hcp). In this case, one continuous curve for g^s cannot be drawn. Each solid phase must have its own separate Gibbs energy curve, as shown schematically in **Figure 22**b at 800 K. In this figure, $\mu_{Mg}^{o(hcp)}$ and $\mu_{Ag}^{o(fcc)}$ are the standard molar Gibbs energies of pure hcp Mg and pure fcc Ag, while $\mu_{Ag}^{o(hcp\text{-}Mg)}$ is the standard molar Gibbs energy of pure (hypothetical) hcp Ag in the hcp-Mg phase.

Since the solubility of Ag in the hcp-Mg phase is limited, we can, to a good approximation, describe it as a *Henrian ideal solution*. That is, when a solution is sufficiently dilute in one component, we can approximate $\mu_{solute}^{E} = RT\ln\ \gamma_{solute}$ by its value in an infinitely dilute solution. That is, if X_{solute} is small, we set $\gamma_{solute} = \gamma_{solute}^{o}$, where γ_{solute}^{o} is the *Henrian activity coefficient* at $X_{solute} = 0$. Thus, for sufficiently dilute solutions, we assume that γ_{solute} is independent of composition. Physically, this means that in a very dilute solution, there is negligible interaction among solute particles because they are so far apart. Hence, each additional solute particle added to the solution makes the same contribution to the excess Gibbs energy of the solution and so $\mu_{solute}^{E} = dG^{E}/dn_{solute} = \text{constant}$.

From the Gibbs–Duhem Eqn 117, if $d\mu_{solute}^{E} = 0$, then $d\mu_{solvent}^{E} = 0$. Hence, in a Henrian solution, $\gamma_{solvent}$ is also constant and equal to its value in an infinitely dilute solution. That is, $\gamma_{solvent} = 1$ and the solvent behaves ideally. In summary, then, for dilute solutions ($X_{solvent} \approx 1$), *Henry's Law* applies

$$\begin{aligned} &\gamma_{solvent} \approx 1 \\ &\gamma_{solute} \approx \gamma_{solute}^{o} = \text{constant} \end{aligned} \tag{142}$$

(Care must be exercised for solutions other than simple substitutional solutions. Henry's Law applies only if the ideal activity is defined correctly for the applicable solution model. Solution models are discussed in Section 3.8.2.)

Henrian activity coefficients can usually be expressed as functions of temperature:

$$RT\ln\gamma_i^{o} = a - bT \tag{143}$$

where a and b are constants. If data are limited, it can further be assumed that $b \approx 0$, so that $RT\ln\gamma_i^{o} \approx \text{constant}$.

Treating the hcp-Mg phase in the Ag–Mg system (**Figure 22**b) as a Henrian solution, we write

$$\begin{aligned} g^{hcp} &= \left(X_{Ag}\mu_{Ag}^{o(fcc)} + X_{Mg}\mu_{Mg}^{o(hcp)}\right) + RT\left(X_{Ag}\ln\ a_{Ag} + X_{Mg}\ln\ a_{Mg}\right) \\ &= \left(X_{Ag}\mu_{Ag}^{o(fcc)} + X_{Mg}\mu_{Mg}^{o(hcp)}\right) + RT\left(X_{Ag}\ln\left(\gamma_{Ag}^{o}X_{Ag}\right) + X_{Mg}\ln\ X_{Mg}\right) \end{aligned} \tag{144}$$

where a_{Ag} and γ_{Ag}^{o} are the activity and activity coefficient of silver with respect to pure fcc silver as standard state. Let us now combine terms as follows:

$$g^{hcp} = \left[X_{Ag}\left(\mu_{Ag}^{o(fcc)} + RT\ln\gamma_{Ag}^{o}\right) + X_{Mg}\mu_{Mg}^{o(hcp)}\right] + RT\left(X_{Ag}\ln X_{Ag} + X_{Mg}\ln X_{Mg}\right) \tag{145}$$

Since γ_{Ag}^{o} is independent of composition, let us define

$$\mu_{Ag}^{o(hcp\text{-}Mg)} = \mu_{Ag}^{o(fcc)} + RT\ln\ \gamma_{Ag}^{o} \tag{146}$$

From Eqns 145 and 146, it can be seen that, relative to $\mu_{Mg}^{o(hcp)}$ and to the hypothetical standard state, $\mu_{Ag}^{o(hcp\text{-}Mg)}$ defined in this way, the hcp solution is ideal. Equations 145 and 146 are illustrated in **Figure 22**b. It can be seen that as γ_{Ag}^{o} becomes larger, the point of tangency N moves to higher Mg concentrations. That is, as $\left(\mu_{Ag}^{o(hcp\text{-}Mg)} - \mu_{Ag}^{o(fcc)}\right)$ becomes more positive, the solubility of Ag in hcp-Mg decreases.

It must be stressed that $\mu_{Ag}^{o(hcp\text{-}Mg)}$, as defined by Eqn 146, is solvent-dependent. That is, $\mu_{Ag}^{o(hcp\text{-}Mg)}$ is not the same as, for example, $\mu_{Ag}^{o(hcp\text{-}Cd)}$ for Ag in dilute hcp-Cd solutions. However, for purposes of developing consistent thermodynamic databases for multicomponent solution phases, it is generally considered advantageous to select a set of values for the chemical potentials of pure elements and compounds in metastable or unstable crystal structures, such as $\mu_{Ag}^{o(hcp)}$, which are independent of the solvent. Such values may be obtained (1) from measurements at high pressures if the structure is stable at high pressure, (2) as averages of the values for several solvents, or (3) from first-principles quantum mechanical or molecular dynamics calculations. Tables (Dinsdale, 1991) of such values for many elements in metastable or unstable states have been prepared and agreed upon by the international community working in the field of phase diagram evaluation and thermodynamic database optimization (Section 3.8). The use of such solvent-independent values, of course, means that even in dilute solutions, nonzero excess Gibbs energy terms are usually required.

3.5.9 Geometry of Binary Temperature-Composition Phase Diagrams

In Section 3.3.1.1, it was shown that when three phases are at equilibrium in a binary system at constant pressure, the system is invariant ($F = 0$). There are two general types of three-phase *invariants* in binary phase diagrams. These are the *eutectic-type* and *peritectic-type* invariants as illustrated in **Figure 23**. Let the three phases concerned be called α, β and γ, with β as the central phase as shown in **Figure 23**. The phases α, β and γ can be solid, liquid or gaseous. At a eutectic-type invariant, the following invariant reaction occurs isothermally as the system is cooled:

$$\beta \rightarrow \alpha + \gamma \tag{147}$$

while at a peritectic-type invariant, the invariant reaction upon cooling is

$$\alpha + \gamma \rightarrow \beta \tag{148}$$

Some examples of eutectic-type invariants are (1) *eutectics* (**Figure 19**), in which α = solid$_1$, β = liquid, γ = solid$_2$; the eutectic reaction is liq $\rightarrow$ s$_1$ + s$_2$; (2) *monotectics* (**Figure 21**), in which α = liquid$_1$, β = liquid$_2$, γ = solid; the monotectic reaction is liq$_2$ $\rightarrow$ liq$_1$, +s; (3) *eutectoids*, in which α = solid$_1$, β = solid$_2$, γ = solid$_3$; the eutectoid reaction is s$_2$ $\rightarrow$ s$_1$ + s$_3$; (4) *catatectics*, in which α = liquid, β = solid$_1$, γ = solid$_2$; the catatectic reaction is s$_1$ $\rightarrow$ liq + s$_2$.

Some examples of peritectic-type invariants are: (1) *peritectics* (**Figure 22**), in which α = liquid, β = solid$_1$, γ = solid$_2$. The peritectic reaction is liq + s$_2$ $\rightarrow$ s$_1$; (2) *syntectics* (**Figure 20**k), in which α = liquid$_1$, β = solid, γ = liquid$_2$. The syntectic reaction is liq$_1$ + liq$_2$ $\rightarrow$ s. (3) *peritectoids*, in which α = solid$_1$, β = solid$_2$, γ = solid$_3$. The peritectoid reaction is s$_1$ + s$_3$ $\rightarrow$ s$_2$.

An important rule of construction, which applies to invariants in binary phase diagrams is illustrated in **Figure 23**. This *extension rule* states that at an invariant, the extension of a boundary of a two-phase

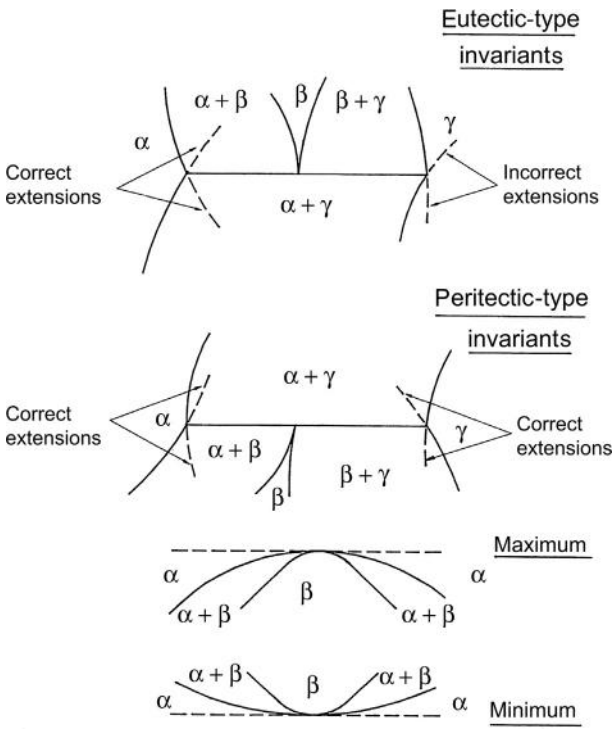

Figure 23 Geometrical units of binary phase diagrams, illustrating rules of construction.

region must pass into the adjacent two-phase region and not into a single-phase region. Examples of both correct and incorrect constructions are given in **Figure 23**. To understand why the "incorrect extension" shown is not correct, consider that the $(\alpha + \gamma)/\gamma$ phase boundary line indicates the composition of the γ phase in equilibrium with the α phase, as determined by the common tangent to the Gibbs energy curves. Since there is no reason for the Gibbs energy curves or their derivatives to change discontinuously at the invariant temperature, the extension of the $(\alpha + \gamma)/\gamma$ phase boundary also represents the stable phase boundary under equilibrium conditions. Hence, for this line to extend into a region labeled as single-phase γ is incorrect. This extension rule is a particular case of the general Schreinemakers' rule (Sections 3.7.4 and 3.7.7.1).

Two-phase regions in binary phase diagrams can terminate (1) on the pure component axes (at $X_A = 1$ or $X_B = 1$) at a transformation point of pure A or B; (2) at a critical point of a miscibility gap; (3) at an invariant. Two-phase regions can also exhibit maxima or minima. In this case, both phase boundaries must pass through their maximum or minimum at the same point as shown in **Figure 23**.

All the *geometrical units* of construction of binary phase diagrams have now been discussed. The phase diagram of a binary alloy system will usually exhibit several of these units. As an example, the Fe–Mo phase diagram was shown in **Figure 1**. The invariants in this system are peritectics at 1612, 1498 and 1453 °C; eutectoids at 1240, 1233 and 308 °C; and peritectoids at 1368 and 1250 °C. The two-phase (liquid + bcc) region passes through a minimum at $X_{Mo} = 0.2$.

Between 910 °C and 1390 °C is a two-phase ($\alpha + \gamma$) *γ-loop*. Pure Fe adopts the fcc γ structure between these two temperatures but exists as the bcc α phase at higher and lower temperatures. Mo, on the other hand, is more soluble in the bcc than in the fcc structure. That is, $\mu_{Mo}^{o(bcc\text{-}Fe)} < \mu_{Mo}^{o(fcc\text{-}Fe)}$, as discussed in Section 3.5.8. Therefore, small additions of Mo stabilize the bcc structure.

In the $CaO–SiO_2$ phase diagram (**Figure 21**), we observe eutectics at 1437, 1463 and 2017 °C; a monotectic at 1689 °C; and a peritectic at 1464 °C. The compound Ca_3SiO_5 dissociates upon heating to CaO and Ca_2SiO_4 by a peritectoid reaction at 1799 °C and dissociates upon cooling to CaO and Ca_2SiO_4 by a eutectoid reaction at 1300 °C. Maxima are observed at 2154 and 1540 °C. At 1465 °C, there is an invariant associated with the tridymite → cristobalite transition of SiO_2. This is either a peritectic or a catatectic depending upon the relative solubility of CaO in tridymite and cristobalite. However, these solubilities are very small and unknown. At 1437 °C, Ca_2SiO_4 undergoes an allotropic transformation. This gives rise to two invariants, one involving $Ca_2SiO_4(\alpha)$, $Ca_2SiO_4(\beta)$ and Ca_3SiO_5, and the other $Ca_2SiO_4(\alpha)$, $Ca_2SiO_4(\beta)$ and $Ca_3Si_2O_7$. Since the compounds are all essentially stoichiometric, these two invariants are observed at almost exactly the same temperature of 1437 °C and it is not possible to distinguish whether they are of the eutectoid or peritectoid type.

3.6 Ternary Temperature-Composition Phase Diagrams

3.6.1 The Ternary Composition Triangle

In a ternary system with components A–B–C, the sum of the mole fractions is unity, $(X_A + X_B + X_C) = 1$. Hence, there are two independent composition variables. A representation of composition, symmetrical with respect to all three components, may be obtained with the equilateral "composition triangle" as shown in **Figure 24** for the Bi–Sn–Cd system. Compositions at the corners of the triangle correspond to the pure components. Compositions along the edges of the triangle correspond to the three binary subsystems Bi–Sn, Sn–Cd and Cd–Bi. Lines of constant mole fraction X_{Bi} are parallel to the Sn–Cd edge, while lines of constant X_{Sn} and X_{Cd} are parallel to the Cd–Bi and Bi–Sn edges, respectively. For example, at point *a* in **Figure 24**, $X_{Bi} = 0.05$, $X_{Sn} = 0.45$ and $X_{Cd} = 0.50$.

Similar equilateral composition triangles can be drawn with coordinates in terms of weight percentage of the three components.

3.6.2 Ternary Space Model

A ternary temperature-composition phase diagram at constant total pressure may be plotted as a three-dimensional "space model" within a right triangular prism with the equilateral composition triangle as base and temperature as vertical axis. Such a space model for a simple eutectic ternary system A–B–C is illustrated in **Figure 25**. On the three vertical faces of the prism are found the phase diagrams of the three binary subsystems, A–B, B–C and C–A which, in this example, are all simple eutectic binary systems. The binary eutectic points are e_1, e_2 and e_3. Within the prism, we see three *liquidus surfaces* descending from the melting points of pure A, B and C. Compositions on these surfaces correspond to compositions of liquid in equilibrium with A-, B- and C-rich solid phases.

In a ternary system at constant pressure, the Gibbs Phase Rule, Eqn 80, becomes

$$F = 4 - P \tag{149}$$

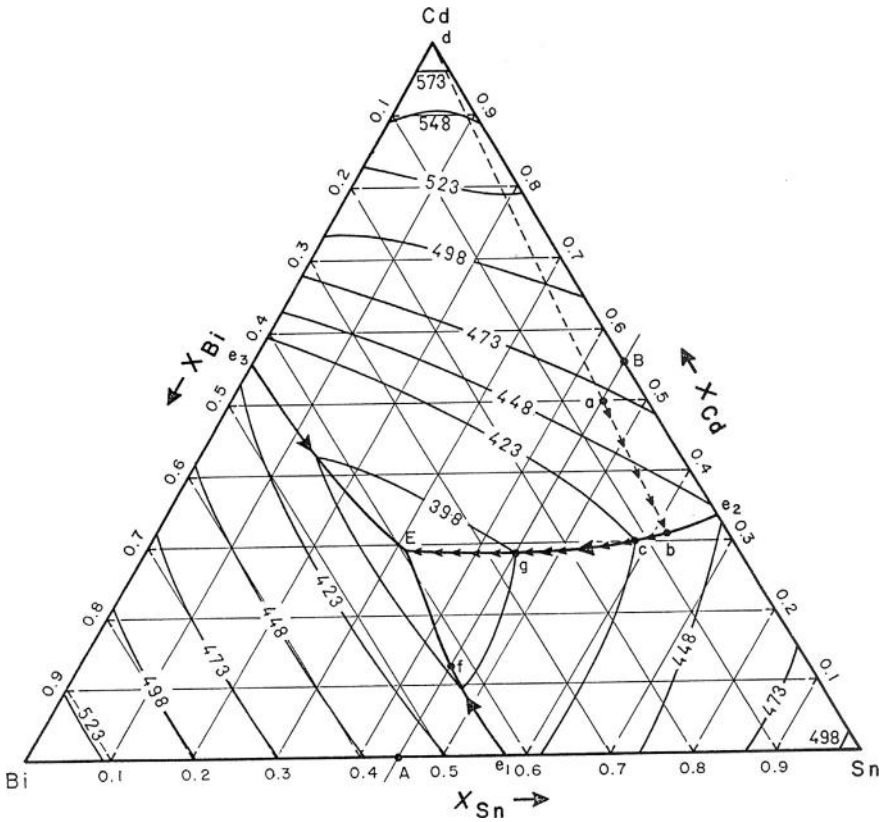

Figure 24 Projection of the liquidus surface of the Bi–Sn–Cd system onto the ternary composition triangle (after Bray et al., 1961–1962). Small arrows show the crystallization path of an alloy of overall composition at point *a* ($P = 1$ bar).

When the liquid and one solid phase are in equilibrium, $P = 2$. Hence, $F = 2$ and the system is bivariant. A ternary liquidus is thus a two-dimensional surface. We may choose two variables, say T, and one composition coordinate of the liquid, but then the other liquid composition coordinate and the composition of the solid are fixed.

The A- and B-liquidus surfaces in **Figure 25** intersect along the line e_1E. Liquids with compositions along this line are therefore in equilibrium with A-rich and B-rich solid phases simultaneously. That is, $P = 3$ and so, $F = 1$. Such "valleys" are thus called *univariant lines*. The three univariant lines meet at the *ternary eutectic point E* at which $P = 4$ and $F = 0$. This is an invariant point since the temperature and the compositions of all four phases in equilibrium are fixed.

3.6.3 Polythermal Projections of Liquidus Surfaces

A two-dimensional representation of the ternary liquidus surface may be obtained as an orthogonal projection upon the base composition triangle. Such a *polythermal projection* of the liquidus of the Bi–Sn–Cd system (Bray et al., 1961–1962) is shown in **Figure 24**. This is a simple eutectic ternary system with a space model like that shown in **Figure 25**. The constant temperature lines on **Figure 24**

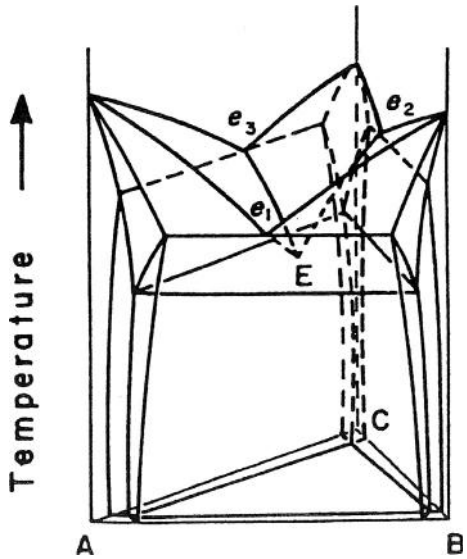

Figure 25 Perspective view of ternary space model of a simple eutectic ternary system. e_1, e_2 and e_3 are the binary eutectics and E is the ternary eutectic. The base of the prism is the equilateral composition triangle (pressure = constant).

are called *liquidus isotherms*. The univariant valleys are shown as heavier lines. By convention, the large arrows indicate the directions of decreasing temperature along these lines.

Let us consider the sequence of events occurring during the equilibrium cooling from the liquid of an alloy of overall composition *a* in **Figure 24**. Point *a* lies within the field of *primary crystallization* of Cd. That is, it lies within the composition region in **Figure 24**, in which Cd-rich solid will be the first solid to precipitate upon cooling. As the liquid alloy is cooled, the Cd-liquidus surface is reached at $T \approx 465$ K (slightly below the 473 K isotherm). A solid Cd-rich phase begins to precipitate at this temperature. Now, in this particular system, Bi and Sn are nearly insoluble in solid Cd, so that the solid phase is virtually pure Cd. (Note that this fact cannot be deduced from **Figure 24** alone.) Therefore, as solidification proceeds, the liquid becomes depleted in Cd, but the ratio X_{Sn}/X_{Bi} in the liquid remains constant. Hence, the composition path followed by the liquid (its *crystallization path*) is a straight line passing through point *a* and projecting to the Cd-corner of the triangle. This crystallization path is shown in **Figure 24** as the line *ab*.

In the general case in which a solid solution rather than a pure component or stoichiometric compound is precipitating, the crystallization path will not be a straight line. However, for equilibrium cooling, a straight line joining a point on the crystallization path at any T to the overall composition point *a* will extend through the composition, on the solidus surface, of the solid phase in equilibrium with the liquid at that temperature. That is, the compositions of the two equilibrium phases and the overall system composition always lie on the same tie-line as is required by mass balance considerations.

When the composition of the liquid has reached point *b* in **Figure 24** at $T \approx 435$ K, the relative proportions of the solid Cd and liquid phases at equilibrium are given by the *lever rule* applied to the *tie-line dab*: (moles of liquid)/(moles of Cd) = *da*/*db*, where *da* and *ab* are the lengths of the line segments. Upon further cooling, the liquid composition follows the univariant valley from *b* to *E* while Cd- and

Sn-rich solids coprecipitate as a binary eutectic mixture. When the liquidus composition attains the ternary eutectic composition E at $T \approx 380$ K, the invariant *ternary eutectic reaction* occurs:

$$\text{liquid} \rightarrow s_1 + s_2 + s_3 \tag{150}$$

where s_1, s_2 and s_3 are the three solid phases and where the compositions of all four phases (as well as T) remain fixed until all liquid has solidified.

In order to illustrate several of the features of polythermal projections of liquidus surfaces, a projection of the liquidus surface of a hypothetical system A–B–C is shown in **Figure 26**. For the sake of simplicity, isotherms are not shown; only the univariant lines are shown, with arrows to show the directions of decreasing temperature. The binary subsystems A–B and C–A are simple eutectic systems, while the binary subsystem B–C contains one congruently melting binary phase, ε, and one incongruently melting binary phase, δ, as shown in the insert in **Figure 26**. The letters *e* and *p* indicate binary eutectic and peritectic points. The δ and ε phases are called *binary compounds* since they have compositions within a binary subsystem. Two *ternary compounds*, η and ζ, with compositions within the ternary triangle, as indicated in **Figure 26**, are also found in this system. All compounds, as well as pure solid A, B and C (the α, β and γ phases), are assumed to be stoichiometric (i.e. there is no solid solubility). The fields of primary crystallization of all the solids are indicated in parentheses in **Figure 26**. The composition of the ε phase lies within its field since it is a congruently melting compound, while the composition of the

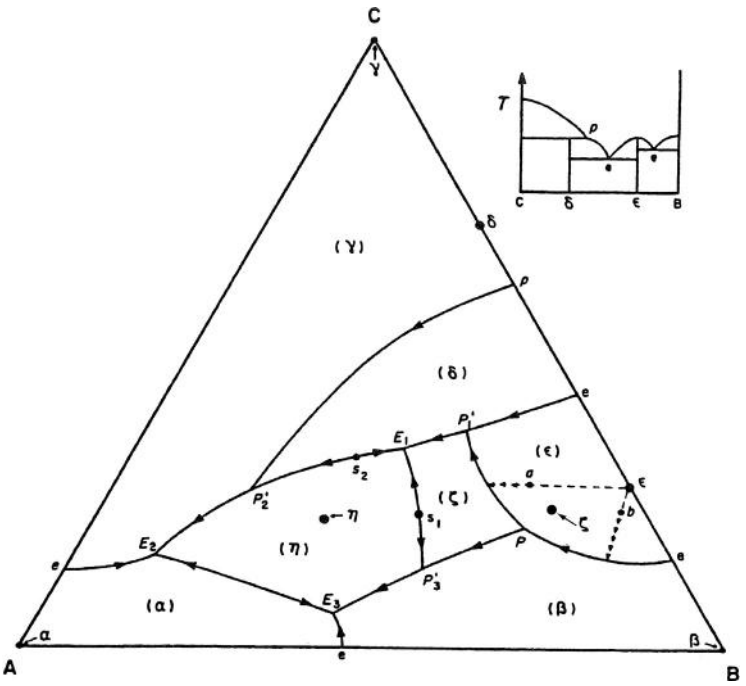

Figure 26 Projection of the liquidus surface of a system A–B–C. The binary subsystems A–B and C–A are simple eutectic systems. The binary phase diagram B–C is shown in the insert. All solid phases are assumed pure stoichiometric components or compounds. Small arrows show the initial parts of the crystallization paths of alloys of compositions at points *a* and *b*.

δ phase lies outside of its field since it is an incongruently melting compound. Similarly for the ternary compounds, η is a congruently melting compound while ζ is incongruently melting. For the congruent compound η, the highest temperature on the η liquidus occurs at the composition of η.

The univariant lines meet at a number of *ternary eutectics E* (three arrows converging on the point), a *ternary peritectic P* (one arrow entering, two arrows leaving the point), and several *ternary quasi-peritectics P′* (two arrows entering, one arrow leaving). Two *saddle points s* are also shown. These are points of maximum T along the univariant line but of minimum T on the liquidus surface along a section joining the compositions of the two solids. For example, s_1 is a maximum point along the univariant $E_1P'_3$, but is a minimum point on the liquidus along the straight line $\zeta s_1 \eta$.

Let us consider the events occurring during equilibrium cooling from the liquid of an alloy of overall composition *a* in **Figure 26**. The primary crystallization product will be the ε phase. Since this is a pure stoichiometric solid, the crystallization path of the liquid will be along a straight line passing through *a* and extending to the composition of ε as shown in the figure.

Solidification of ε continues until the liquid attains a composition on the univariant valley. Thereafter, the liquid composition descends along the valley toward the point P'_1 in coexistence with ε and ζ. At point P'_1, the invariant *ternary quasi-peritectic reaction* occurs isothermally:

$$\text{liquid} + \varepsilon \;\rightarrow\; \delta + \zeta \tag{151}$$

Since there are two reactants, there are two possible outcomes: (1) the liquid is completely consumed before the ε phase and solidification will be complete at the point P'_1; (2) ε is completely consumed before the liquid and solidification will continue with decreasing T along the univariant line P_1E_1 with coprecipitation of δ and ζ until, at E_1, the liquid will solidify eutectically (liquid $\rightarrow$ δ + ζ + η). To determine whether outcome (1) or (2) occurs, we use the mass balance criterion that, for three-phase equilibrium, the overall composition *a* must always lie within the *tie-triangle* formed by the compositions of the three phases. Now, the triangle joining the compositions of δ, ε and ζ, does not contain the point *a*, but the triangle joining the compositions of δ, ζ and liquid at P'_1 does contain the point *a*. Hence, outcome (2) occurs.

An alloy of overall composition *b* in **Figure 26** solidifies with ε as primary crystallization product until the liquid composition contacts the univariant line. Thereafter, coprecipitation of ε and β occurs with the liquid composition following the univariant valley until the liquid reaches the peritectic composition *P*. The invariant *ternary peritectic reaction* then occurs isothermally:

$$\text{liquid} + \varepsilon + \beta \;\rightarrow\; \zeta \tag{152}$$

Since there are three reactants, there are three possible outcomes: (1) the liquid is consumed before either ε or β and solidification terminates at *P*; (2) ε is consumed first and solidification then continues along the path PP'_3; or (3) β is consumed first and solidification continues along the path PP'_1. Which outcome actually occurs depends on whether the overall composition *b* lies within the tie-triangle (1) εβζ, (2) βζ*P*, or (3) εζ*P*. In the example shown, outcome (1) will occur.

A polythermal projection of the liquidus surface of the Zn–Mg–Al system is shown in **Figure 27**. There are 11 primary crystallization fields of nine binary solid solutions (with limited solubility of the third component) and of two ternary solid solutions. There are three ternary eutectic points, three saddle points, three ternary peritectic points and five ternary quasi-peritectic points.

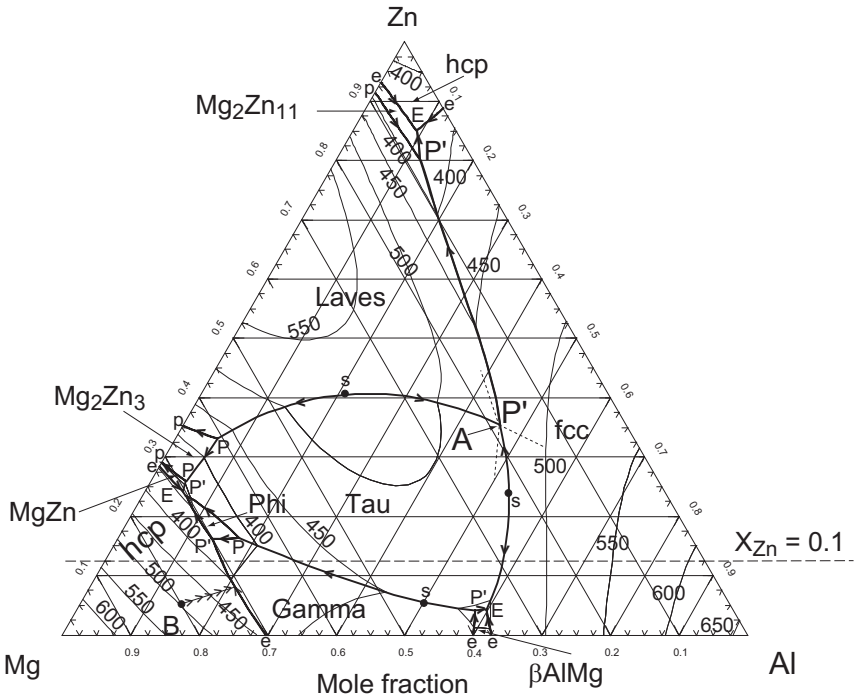

Figure 27 Polythermal projection of the liquidus surface of the Zn–Mg–Al system at $P = 1$ bar (see FactSage).

3.6.4 Ternary Isothermal Sections

Polythermal projections of the liquidus surface do not provide information on the compositions of the solid phases at equilibrium. However, this information can be presented at any one temperature on an *isothermal section* such as that shown for the Bi–Sn–Cd system at 423 K in **Figure 28**. This phase diagram is a constant temperature slice through the space model of **Figure 25**.

The liquidus lines bordering the one-phase liquid region of **Figure 28** are identical to the 423 K isotherms of the projection in **Figure 24**. Point *c* in **Figure 28** is point *c* on the univariant line in **Figure 24**. An alloy with overall composition in the one-phase liquid region of **Figure 28** at 423 K will consist of a single liquid phase. If the overall composition lies within one of the two-phase regions, then the compositions of the two phases are given by the ends of the *tie-line* that passes through the overall composition. For example, a sample with overall composition *p* in **Figure 28** will consist of a liquid of composition *q* on the liquidus and a solid Bi-rich alloy of composition *r* on the solidus. The relative proportions of the two phases are given by the lever rule:

$$(\text{moles of liquid})/(\text{moles of solid}) = pr/pq, \quad \text{where } pr \text{ and } pq \text{ are the lengths of the tie-line segments.}$$

In the case of solid Cd, the solid phase is nearly pure Cd, so all tie-lines of the (Cd + liquid) region converge nearly to the corner of the triangle. In the case of the Bi- and Sn-rich solids, some solid solubility is observed. (The actual extent of this solubility is exaggerated in **Figure 28** for the sake of clarity of presentation.) Alloys with overall compositions rich enough in Bi or Sn to lie within the

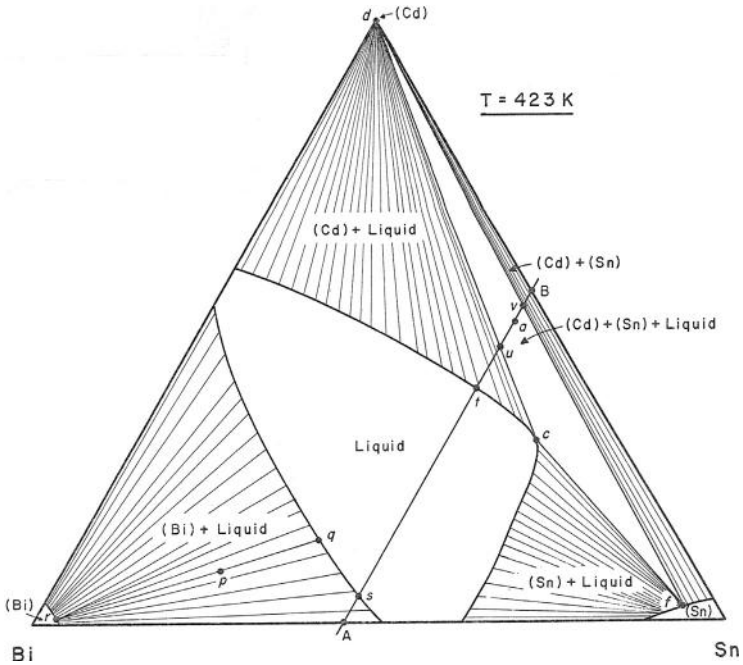

Figure 28 Isothermal section of the Bi–Sn–Cd system at 423 K at $P = 1$ bar (after Bray et al., 1961–1962). Extents of solid solubility in Bi and Sn have been exaggerated for clarity of presentation.

single-phase (Sn) or (Bi) regions of **Figure 28** will consist at 423 K of single-phase solid solutions. Alloys with overall compositions at 423 K in the two-phase (Cd + Sn) region will consist of two solid phases.

Alloys with overall compositions within the three-phase triangle *dcf* will, at 423 K, consist of three phases: Cd- and Sn-rich solids with compositions at *d* and *f* and liquid of composition *c*. To understand this better, consider an alloy of composition *a* in **Figure 28**, which is the same composition as the point *a* in **Figure 24**. In Section 3.6.3, we saw that when an alloy of this composition is cooled, the liquid follows the path *ab in* **Figure 24** with primary precipitation of Cd and then follows the univariant line with coprecipitation of Cd and Sn, so that at 423 K, the liquid is at the composition point *c*, and two solid phases are in equilibrium with the liquid.

3.6.4.1 Topology of Ternary Isothermal Sections

At constant temperature, the Gibbs energy of each phase in a ternary system is represented as a function of composition by a surface plotted in a right triangular prism with Gibbs energy as vertical axis and the composition triangle as base. Just as the compositions of phases at equilibrium in binary systems are determined by the points of contact of a common tangent line to their isothermal Gibbs energy curves (**Figure 13**), so the compositions of phases at equilibrium in a ternary system are given by the points of contact of a common tangent plane to their isothermal Gibbs energy surfaces (or, equivalently as discussed in Section 3.4.2, by minimizing the total Gibbs energy of the system). A common tangent plane can contact two Gibbs energy surfaces at an infinite number of pairs of points, thereby generating an infinite number of tie-lines within a two-phase region on an isothermal section. A common tangent

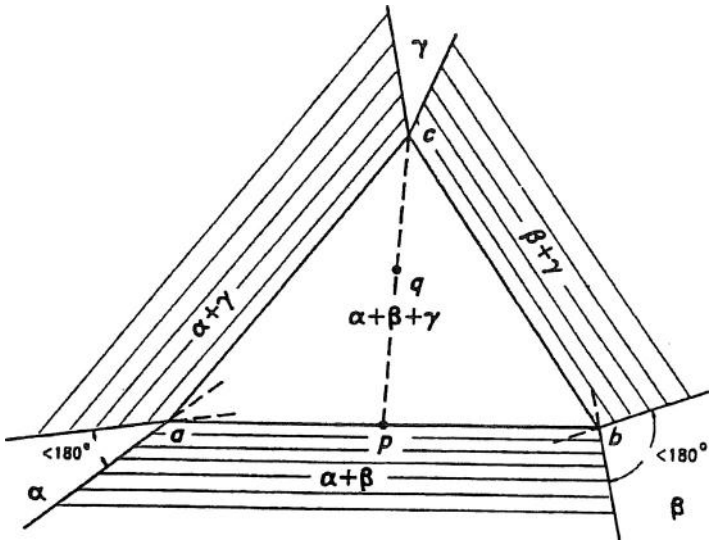

Figure 29 A tie-triangle in a ternary isothermal (and isobaric) section illustrating the lever rule and the extension rule (Schreinemakers' rule).

plane to three Gibbs energy surfaces contacts each surface at a unique point, thereby generating a three-phase tie-triangle.

Hence, the principal topological units of construction of an isothermal ternary phase diagram are three-phase ($\alpha + \beta + \gamma$) tie-triangles as in **Figure 29** with their accompanying two-phase and single-phase areas. Each corner of the tie-triangle contacts a single-phase region, and from each edge of the triangle, there extends a two-phase region. The edge of the triangle is a limiting tie-line of the two-phase region.

For overall compositions within the tie-triangle, the compositions of the three phases at equilibrium are fixed at the corners of the triangle. The relative proportions of the three phases are given by the *lever rule of tie-triangles*, which can be derived from mass balance considerations. At an overall composition q in **Figure 29**, for example, the relative proportion of the γ phase is given by projecting a straight line from the γ corner of the triangle (point c) through the overall composition q to the opposite side of the triangle, point p. Then, (moles of γ)/(total moles) = qp/cp if compositions are expressed as mole fractions, or (weight of γ)/(total weight) = qp/cp if compositions are in weight percent.

Isothermal ternary phase diagrams are generally composed of a number of these topological units. An example for the Zn–Mg–Al system at 25 °C is shown in **Figure 2**. At 25 °C, hcp-Mg, hcp-Zn and Mg_2Zn_{11} are nearly stoichiometric compounds, while Mg and Zn have very limited solubility in fcc-Al. The gamma and βAlMg phases are binary compounds, which exhibit very narrow ranges of stoichiometry in the Mg–Al binary system and in which Zn is very sparingly soluble. The Laves, Mg_2Zn_3 and MgZn phases are virtually stoichiometric binary compounds, in which Al is soluble to a few percent. Their ranges of stoichiometry are thus shown in **Figure 2** as very narrow lines. The Tau phase is a ternary phase with a small single-phase region of stoichiometry as shown. An examination of **Figure 2** will show that it is composed of the topological units of **Figure 29**.

An *extension rule*, a particular case of *Schreinemakers' Rule* (Sections 3.7.4 and 3.7.7.1), for ternary tie-triangles is illustrated in **Figure 29** at points a and b. At each corner, the extension of the boundaries of the single-phase regions, indicated by the broken lines, must either both project into the triangle as at

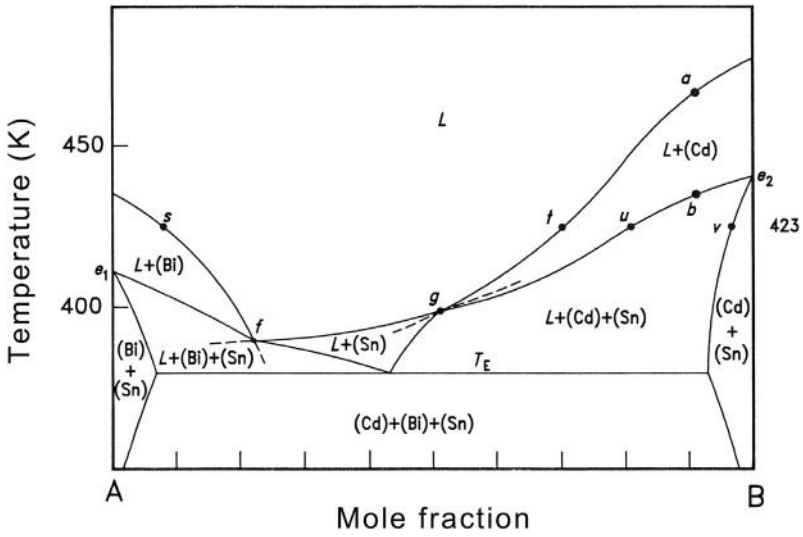

Figure 30 Isopleth (constant composition section) of the Bi–Sn–Cd system at $P = 1$ bar following the line AB of **Figure 24**. (Extents of solid solubility in the terminal solid solutions have been exaggerated for clarity of presentation.)

point *a*, or must both project outside the triangle as at point *b*. Furthermore, the angle between the boundaries must not be greater than 180°.

Another important rule of construction, whose derivation is evident, is that within any two-phase region tie-lines must never cross one another.

3.6.5 Ternary Isopleths (Constant Composition Sections)

A vertical *isopleth*, or constant composition section, through the space model of the Bi–Sn–Cd system, is shown in **Figure 30**. The section follows the line AB in **Figure 24**.

The phase fields in **Figure 30** indicate which phases are present when an alloy with an overall composition on the line AB is equilibrated at any temperature. For example, consider the cooling, from the liquid state, of an alloy of composition *a*, which is on the line AB (**Figure 24**). At $T \approx 465$ K, precipitation of the solid (Cd) phase begins at point *a* in **Figure 30**. At $T \approx 435$ K (point *b* in **Figures 24 and 30**), the solid (Sn) phase begins to appear. Finally, at the eutectic temperature T_E, the ternary reaction occurs, leaving solid (Cd) + (Bi) + (Sn) at lower temperatures. The intersection of the isopleth with the univariant lines in **Figure 24** occurs at points *f* and *g*, which are also indicated in **Figure 30**. The intersection of this isopleth with the isothermal section at 423 K is shown in **Figure 28**. The points *s*, *t*, *u* and *v* of **Figure 28** are also shown in **Figure 30**.

It is important to note that on an isopleth, the tie-lines do not, in general, lie in the plane of the diagram. Therefore, the diagram provides information only on which phases are present, not on their compositions or relative proportions. The boundary lines on an isopleth do not, in general, indicate the phase compositions or relative proportions, only the temperature at which a phase appears or disappears for a given overall composition. The lever-rule cannot be applied on an isoplethal section.

An isoplethal section of the Zn–Mg–Al system at 10 mol% Zn was shown in **Figure 3**a. The liquidus surface of the diagram may be compared to the liquidus surface along the line where $X_{Zn} = 0.1$ in

Figure 27 and to the section at $X_{Zn} = 0.1$ in the isothermal section at 25 °C in Figure 2. Point p on the two-phase (Tau + Gamma) field in Figure 3a at 25 °C corresponds to point p in Figure 2, where the equilibrium compositions of the Gamma and Tau phases are given by the ends of the tie-line. These individual phase compositions cannot be read from Figure 3a.

The geometrical rules that apply to isoplethal sections will be discussed in Section 3.7.

3.6.5.1 Quasibinary Phase Diagrams

The binary $CaO–SiO_2$ phase diagram in Figure 21 is actually an isopleth of the ternary Ca–Si–O system along the line $n_O = (n_{Ca} + 2n_{Si})$. However, all tie-lines in Figure 21 lie within (or virtually within) the plane of the diagram because $n_O = (n_{Ca} + 2n_{Si})$ in every phase. Therefore, the diagram is called a *quasibinary* phase diagram. Similarly, the $K_2CO_3–Na_2CO_3$ phase diagram in Figure 17 is a quasibinary isoplethal section of the quaternary K–Na–C–O system.

3.7 General Phase Diagram Sections

Phase diagrams involving temperature and composition as variables have been discussed in Sections 3.5 and 3.6 for binary and ternary systems. In the present section, we shall discuss the geometry of general phase diagram sections involving these and other variables such as total pressure, chemical potentials, volume, enthalpy, etc. for systems of any number of components. A few examples of such diagrams have already been shown in Figures 4–7, 9 and 10. It will now be shown that all these phase diagrams, although seemingly quite different geometrically, actually all obey one simple set of geometrical rules.

The rules which will be developed apply to two-dimensional phase diagram sections in which two thermodynamic variables are plotted as axes while other variables are held constant. We shall develop a set of sufficient conditions for the choice of axis variables and constants, which ensure that the phase diagram section is single-valued, with each point on the diagram representing a unique equilibrium state. Although these rules do not apply directly to phase diagram projections such as in Figures 24, 26 and 27, such diagrams can be considered to consist of portions of several phase diagram sections projected onto a common plane. Some geometrical rules specific to projections will be given in Section 3.7.13. Finally, since all single-valued phase diagram sections obey the same set of geometrical rules, one single algorithm can be used for their calculation as will be demonstrated in Section 3.7.4.1.

In Sections 3.7.1–3.7.6, we shall first present the geometrical rules governing general phase diagram sections without giving detailed proofs. Rigorous proofs will follow in Sections 3.7.7 and 3.7.9.

3.7.1 Corresponding Potentials and Extensive Variables

In a system with C components, we select the following $(C + 2)$ *thermodynamic potentials* (intensive variables): T, P, μ_1, μ_2, ……, μ_C. For each potential ϕ_i, there is a *corresponding extensive variable* q_i related by the equation:

$$\phi_i = (\partial U/\partial q_i)_{q_{j(j\neq i)}} \tag{153}$$

The corresponding pairs of potentials and extensive variables are listed in Table 1. The corresponding pairs are found together in the terms of the fundamental Equation 9 and in the Gibbs–Duhem Equation 75.

Table 1 Corresponding pairs of potentials ϕ_i and extensive variables q_i

ϕ_i:	T	P	μ_1	$\mu_2 \ldots$	μ_C
q_i:	S	$-V$	n_1	$n_2 \ldots$	n_C

When a system is at equilibrium, the potential variables are the same for all phases (all phases are at the same T, P, μ_1, μ_2, …) but the extensive variables can differ from one phase to the next (the phases can all have different volumes, entropies and compositions). In this regard, it is important to note the following. If the only variables which are held constant are potential variables, then the compositions of all phases will lie in the plane of the phase diagram section and the lever rule may be applied. Some examples are found in **Figures 1, 2 and 5**. However, if an extensive variable such as composition is held constant, then this is no longer necessarily true as was discussed, for example, in Section 3.6.5 regarding isoplethal sections such as **Figures 3, 4 and 30**.

3.7.2 The Law of Adjoining Phase Regions

The following *Law of Adjoining Phase Regions* (Palatnik and Landau, 1956) applies to all single-valued phase diagram sections: *"As a phase boundary line is crossed, one and only one phase either appears or disappears."*

This law is clearly obeyed in any phase diagram section in which both axis variables are extensive variables such as **Figures 2, 3b, 4 and 28**. When one axis variable is a potential, however, it may at first glance appear that the law is not obeyed for invariant lines. For instance, as the eutectic line is crossed in the binary T composition phase diagram in **Figure 19**, one phase disappears and another appears. However, the eutectic line in this figure is not a simple phase boundary, but rather an infinitely narrow three-phase region. This is illustrated schematically in **Figure 31**, where the three-phase region has been "opened up" to show that the region is enclosed by upper and lower phase boundaries which are coincident. In passing from the (β + L) to the (α + β) region, for example, we first pass through the (α + β + L) region. Hence, the Law of Adjoining Phase Regions is obeyed. The three-phase region is infinitely narrow because all three phases at equilibrium must be at the same temperature. Another example is seen in the isoplethal section in **Figure 30**. At the ternary eutectic temperature, T_E, there is an

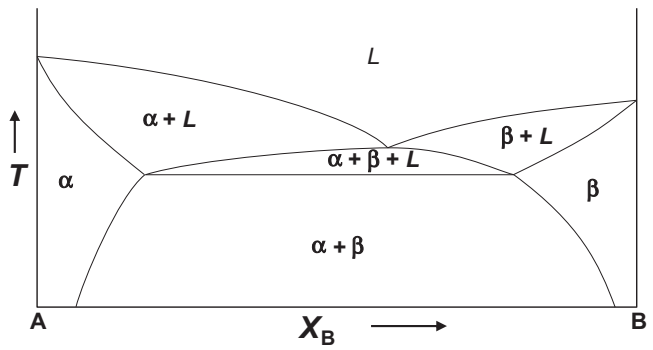

Figure 31 An isobaric temperature-composition phase diagram with the eutectic "opened up" to show that it is an infinitely narrow three-phase region. Reprinted with permission from Pelton (2001a).

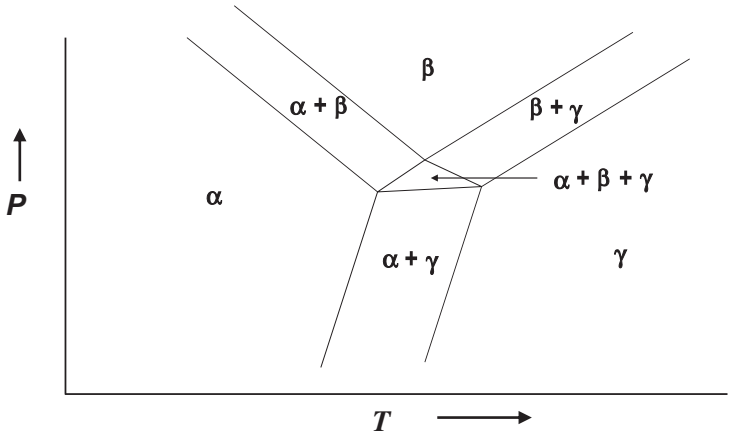

Figure 32 A *P*–*T* diagram in a one-component system "opened up" to show that the two-phase lines are infinitely narrow two-phase regions. Reprinted with permission from Pelton (2001a).

infinitely narrow horizontal four-phase invariant region (L + (Bi) + (Cd) + (Sn)). As yet another example, the *y*-axis of **Figure 5** is the chemical potential of oxygen, which is the same in all phases at equilibrium. This diagram exhibits two infinitely narrow horizontal three-phase invariant regions.

Similarly, if both axis variables are potentials, there may be several infinitely narrow univariant phase regions. For example, in the *P*–*T* diagram of **Figure 7**a, all lines are infinitely narrow two-phase regions bounded on either side by coincident phase boundaries as shown schematically in **Figure 32**, where all two-phase regions have been "opened up." The three-phase invariant triple point is then seen to be a degenerate three-phase triangle. Other examples of diagrams in which both axis variables are potentials are seen in **Figures 6, 9 and 10**. All lines in **Figures 9 and 10** are infinitely narrow two-phase univariant regions. In **Figure 6**, some lines are infinitely narrow three-phase univariant regions while others are simple phase boundaries.

3.7.3 Nodes in Phase Diagram Sections

All phase boundary lines in any single-valued phase diagram section meet at nodes where exactly four lines converge as illustrated in **Figure 33**. *N* phases ($\alpha_1, \alpha_2, \ldots, \alpha_N$), where $N \geq 1$, are common to all four regions. Two additional phases, β and γ, are disposed as shown in **Figure 33**, giving rise to two $(N + 1)$-phase regions and one $(N + 2)$-phase region. At every node, the generalized *Schreinemakers' Rule* requires that the extensions of the boundaries of the *N*-phase region must either both lie within the $(N + 1)$-phase regions as in **Figure 33**, or they must both lie within the $(N + 2)$-phase region.

Schreinemakers' Rule will be proven in Section 3.7.7.1.

An examination of **Figure 4**, for example, will reveal that all nodes involve exactly four boundary lines. Schreinemakers' Rule is illustrated on this figure by the dashed extensions of the phase boundaries at the nodes labeled *a*, *b* and *c* and in **Figure 30** by the dashed extension lines at nodes *f* and *g*.

For phase diagrams in which one or both axis variables are potentials, it might, at first glance, seem that fewer than four boundaries converge at some nodes. However, all nodes can still be seen to involve

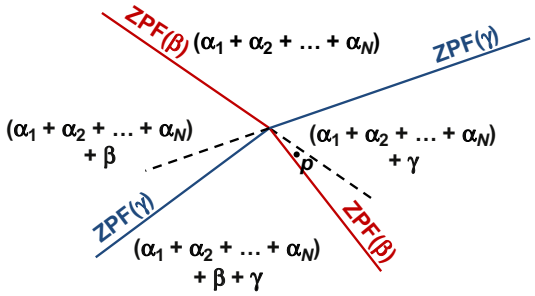

Figure 33 A node in a general phase diagram section showing the Zero Phase Fraction lines of the β and γ phases. Schreinemakers' Rule is obeyed. Reprinted with permission from Pelton (2001a). (For color version of this figure, the reader is referred to the online version of this book.)

exactly four phase boundary lines when all infinitely narrow phase regions are "opened up" as in **Figures 31 and 32**.

The extension rule illustrated in **Figure 29** for tie-triangles in ternary isothermal sections can be seemed to be a particular case of Schreinemakers' Rule, as can the extension rules shown in **Figure 23** for binary *T*-composition phase diagrams. Finally, an extension rule for triple points on *P*–*T* phase diagrams is illustrated in **Figure 7**a; the extension of each univariant line must pass into the opposite bivariant region. This rule, which can be seen to apply to **Figures 9 and 10** as well, is also a particular case of Schreinemakers' Rule.

An objection might be raised that a minimum or a maximum in a two-phase region in a binary temperature-composition phase diagram, as in **Figures 17, 21 and 22**, represents an exception to Schreinemakers' Rule. However, the extremum in such cases is not actually a node where four phase boundaries converge, but rather a point where two boundaries touch. Such extrema, in which two phase boundaries touch with zero slope, may occur for a *C*-phase region in a phase diagram of a *C*-component system when one axis is a potential. For example, in an isobaric temperature-composition phase diagram of a four-component system, we may observe a maximum or a minimum in a four-phase region separating two three-phase regions. A similar maximum or minimum in a (*C*-*n*)-phase region, where $n > 0$, may also occur along particular composition paths. This will be discussed in more detail in Section 3.9.4.

Other apparent exceptions to Schreinemakers' Rule (such as five boundaries meeting at a node) can occur in special limiting cases, as, for example, if an isoplethal section of a ternary system passes exactly through the ternary eutectic composition.

3.7.4 Zero Phase Fraction Lines

All phase boundaries on any single-valued phase diagram section are *Zero Phase Fraction (ZPF) Lines*, an extremely useful concept introduced by Gupta et al. (1986), which is a direct consequence of the Law of Adjoining Phase Regions. There is a ZPF line associated with each phase. On one side of its ZPF line, the phase occurs, while on the other side, it does not, as illustrated in **Figure 4**. There is a ZPF line for each of the five phases in **Figure 4**. The five ZPF lines account for all the phase boundaries on the two-dimensional section. Phase diagram sections plotted on triangular coordinates as in **Figures 2 and 28** similarly consist of one ZPF line for each phase.

With reference to **Figure 33**, it can be seen that at every node, two ZPF lines cross each other.

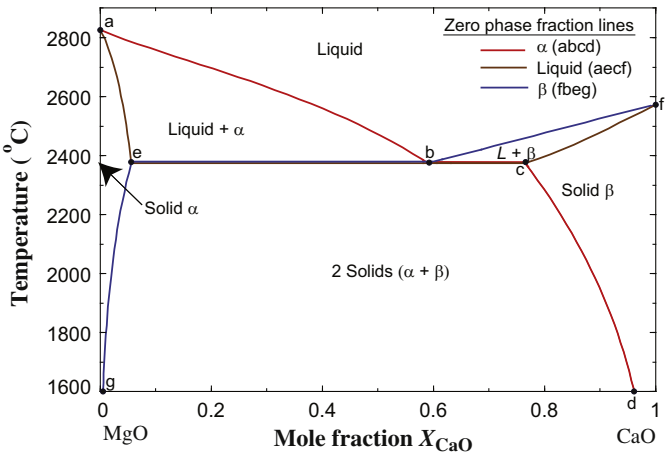

Figure 34 Binary *T*-composition phase diagram at $P = 1$ bar of the MgO–CaO system showing Zero Phase Fraction (ZPF) lines of the phases (see FactSage). (For color version of this figure, the reader is referred to the online version of this book.)

In the case of phase diagrams in which one or both axis variables are potentials, certain phase boundaries may be coincident as was discussed in Section 3.7.2. Hence, ZPF lines for two different phases may be coincident over part of their lengths as is illustrated in **Figure 34**. In **Figures 9 and 10**, every line in the diagram is actually two coincident ZPF lines.

3.7.4.1 General Algorithm to Calculate Any Phase Diagram Section

Since all single-valued phase diagram sections obey the same geometrical rules described in Sections 3.7.1–3.7.3, one general algorithm can be used to calculate any phase diagram section thermodynamically. As discussed in Section 3.2.3, the equilibrium state of a system (that is, the amount and composition of every phase) can be calculated for a given set of conditions (*T*, *P*, overall composition, chemical potentials, etc.) by software that minimizes the total Gibbs energy of the system, retrieving the thermodynamic data for each phase from databases. To calculate any phase diagram section, one first specifies the desired axis variables and their limits as well as the constants of the diagram. The software then scans the four edges of the diagram, using Gibbs energy minimization to find the ends of each ZPF line. Next, each ZPF line is calculated from one end to the other using Gibbs energy minimization to determine the series of points at which the phase is just on the verge of appearing. Should a ZPF line not intersect any edge of the diagram, it will be discovered by the program while it is tracing one of the other ZPF lines. When ZPF lines for all phases have been drawn, the diagram is complete. This is the algorithm used by the FactSage system software, which has been used to calculate most of the phase diagrams shown in this chapter (see FactSage).

3.7.5 Choice of Variables to Ensure that Phase Diagram Sections are Single-valued

In a system of *C* components, a two-dimensional phase diagram section is obtained by choosing two axis variables and holding $(C - 1)$ other variables constant. However, not every choice of variables will result in a single-valued phase diagram with a unique equilibrium state at every point. For example, on

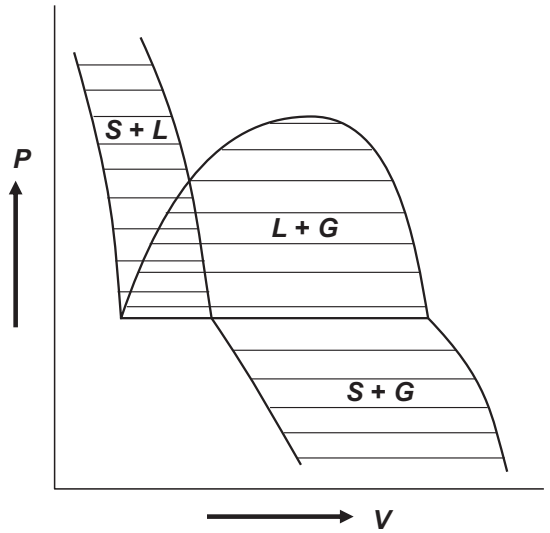

Figure 35 Schematic *P–V* diagram for H_2O. This is not a single-valued phase diagram section (reprinted with permission from Pelton (2001a)).

the *P–V* diagram for H_2O shown schematically in **Figure 35**, at any point in the area where the $(S + L)$ and $(L + G)$ regions overlap, there are two possible equilibrium states of the system. Similarly, the diagram of S_2 pressure versus the mole fraction of Ni at constant T and P in the Cu–Ni–S_2 system in **Figure 36** exhibits a region in which there are two possible equilibrium states.

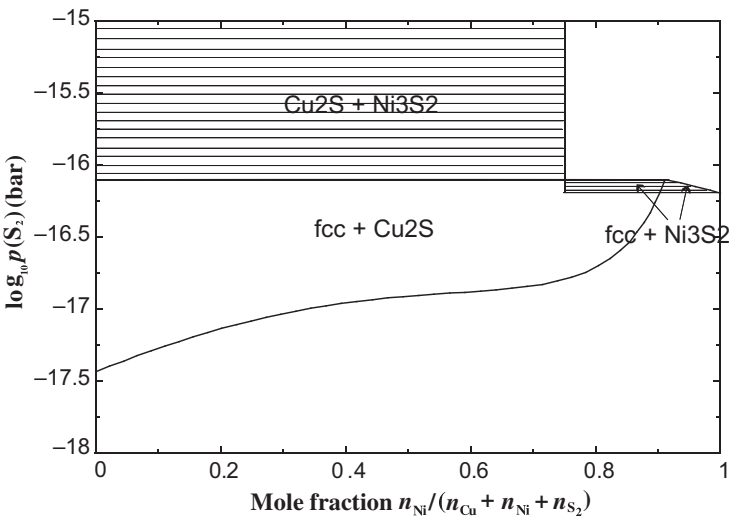

Figure 36 Equilibrium S_2 pressure versus mole fraction of Ni in the Cu–Ni–S_2 system at 427 °C. This is not a single-valued phase diagram (see FactSage).

In order to ensure that a phase diagram section is single-valued at every point, the following procedure for the choice of variables is sufficient:

(1) From each corresponding pair (ϕ_i, q_i) in **Table 1**, select either ϕ_i or q_i, but not both. At least one of the selected variables must be an extensive variable q_i.
(2) Define the size of the system as some function of the selected extensive variables (examples: $(n_1 + n_2) =$ constant; $n_2 =$ constant; $V =$ constant; etc.) and then normalize the chosen extensive variables.
(3) The chosen potentials and normalized extensive variables are then the $(C + 1)$ independent phase diagram variables. Two of these are selected as axes and the others are held constant.

Note that this procedure constitutes a set of sufficient (but not necessary) conditions for the diagram to be single-valued. That is, a diagram which violates these conditions may still be single-valued, but there is no assurance that this will be the case.

The procedure is illustrated by the following examples. In each example, the selected variables, one from each conjugate pair, are underlined.

System Fe–Mo (**Figure 1**):

$$\begin{aligned}
&\phi_i: \quad \underline{T} \quad \underline{P} \quad \mu_{Fe} \quad \mu_{Mo} \\
&q_i: \quad S \quad -V \quad \underline{n_{Fe}} \quad \underline{n_{Mo}} \\
&\text{Size}: (n_{Fe} + n_{Mo}) \\
&\text{Phase diagram variables}: T, P, n_{Mo}/(n_{Fe} + n_{Mo}) = X_{Mo}
\end{aligned}$$

System Fe–Cr–S_2–O_2 (**Figure 6**):

$$\begin{aligned}
&\phi_i: \quad \underline{T} \quad \underline{P} \quad \mu_{Fe} \quad \mu_{Cu} \quad \underline{\mu_{S_2}} \quad \underline{\mu_{O_2}} \\
&q_i: \quad S \quad -V \quad \underline{n_{Fe}} \quad \underline{n_{Cu}} \quad n_{S_2} \quad n_{O_2} \\
&\text{Size}: (n_{Fe} + n_{Cu}) \\
&\text{Phase diagram variables}: T, P, \mu_{O_2}, \mu_{S_2}, n_{Cr}/(n_{Fe} + n_{Cr})
\end{aligned}$$

System Zn–Mg–Al isopleth (**Figure 3**a):

$$\begin{aligned}
&\phi_i: \quad \underline{T} \quad \underline{P} \quad \mu_{Zn} \quad \mu_{Mg} \quad \mu_{Al} \\
&q_i: \quad S \quad -V \quad \underline{n_{Zn}} \quad \underline{n_{Mg}} \quad \underline{n_{Al}} \\
&\text{Size}: (n_{Mg} + n_{Al}) \\
&\text{Phase diagram variables}: T, P, n_{Al}/(n_{Mg} + n_{Al}), n_{Zn}/(n_{Mg} + n_{Al}) = X_{Zn}/(1 - X_{Zn})
\end{aligned}$$

System Al_2SiO_5 (**Figure 7**b):

$$\begin{aligned}
&\phi_i: \quad \underline{T} \quad \underline{P} \quad \mu_{Al_2SiO_5} \\
&q_i: \quad S \quad \underline{-V} \quad \underline{n_{Al_2SiO_5}} \\
&\text{Size}: n_{Al_2SiO_5} \\
&\text{Phase diagram variables}: T, V/n_{Al_2SiO_5}
\end{aligned}$$

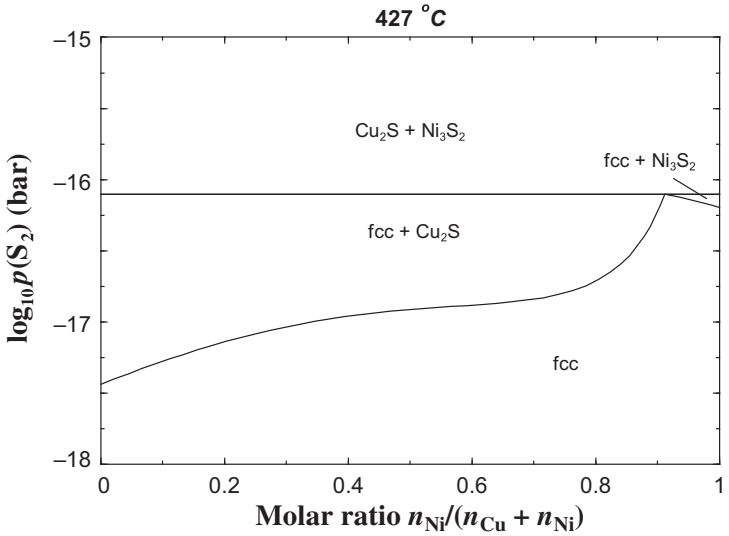

Figure 37 Equilibrium S_2 pressure versus molar ratio $n_{Ni}/(n_{Cu} + n_{Ni})$ in the Cu–Ni–S_2 system at 427 °C. This is a single-valued phase diagram (see FactSage).

System Cu–Ni–S_2 (**Figure 37**):

$$\begin{array}{lccccc} \phi_i: & \underline{T} & \underline{P} & \mu_{Cu} & \mu_{Ni} & \underline{\mu_{S_2}} \\ q_i: & S & -V & \underline{n_{Cu}} & \underline{n_{Ni}} & n_{S_2} \end{array}$$

$$\text{Size}: (n_{Cu} + n_{Ni})$$

$$\text{Phase diagram variables}: T, P, \mu_{S_2}, n_{Ni}/(n_{Cu} + n_{Ni})$$

This choice of variables for the Cu–Ni–S_2 system gives the single-valued phase diagram in **Figure 37**. For the same system in **Figure 36**, an incorrect choice of variables was made, leading to a diagram which is not single-valued. The x-axis variable of **Figure 36** contains the term n_{S_2}. That is, both variables (μ_{S_2}, n_{S_2}) of the same corresponding pair were selected, thereby violating the first selection rule. Similarly, the selection of both variables $(P, -V)$ from the same corresponding pair results in the diagram of **Figure 35**, which is not single-valued. Similar examples of phase diagrams that are not single-valued have been shown by Hillert (1997).

Other examples of applying the procedure for choosing variables will be given in Sections 3.7.8–3.7.10.

In several of the phase diagrams in this chapter, log p_i or RT ln p_i is substituted for μ_i as an axis variable or constant. From Eqn 86, this substitution can clearly be made if T is constant. However, even when T is an axis variable of the phase diagram as in **Figure 10**, this substitution is still permissible since μ_i^o is a monotonic function of T. The substitution of log p_i or RT ln p_i for μ_i results in a progressive expansion and displacement of the axis with increasing T that preserves the overall geometry of the diagram.

3.7.6 Corresponding Phase Diagrams

If a potential axis, ϕ_i, of a phase diagram section is replaced by its normalized conjugate variable q_i, then the new diagram and the original diagram may be said to be *corresponding phase diagrams*. An example is seen in **Figure 7**, where the P-axis of **Figure 7**a is replaced by the V-axis of **Figure 7**b. Another example is shown in **Figure 38** for the Fe–O system. Placing corresponding diagrams beside each other as in **Figures 7 and 38** is useful because the information contained in the two diagrams is complementary. Note how the invariant triple points of one diagram of each pair correspond to the invariant lines of the other. Note also that as ϕ_i, increases, q_i increases. That is, in passing from left to right at constant T across the two diagrams in **Figure 38**, the same sequence of phase regions is encountered. This is a general result of the thermodynamic stability criterion which will be discussed in Section 3.7.7.

A set of corresponding phase diagrams for a multicomponent system with components 1,2,3,……,C is shown in **Figure 39**. The potentials ϕ_4, ϕ_5, …, ϕ_{C+2} are held constant. The size of the system (in the sense of Section 3.7.5) is q_3. The invariant triple points of **Figure 39**b correspond to the invariant lines of **Figure 39**a and d and to the invariant tie-triangles of **Figure 39**c. The *critical points* of **Figure 39**b, where the two-phase regions terminate, correspond to the critical points of the "miscibility gaps" in **Figure 39**a, c and d.

A set of corresponding phase diagrams for the Fe–Cr–O_2 system at $T = 1300\,^{\circ}C$ is shown in **Figure 40**. **Figure 40**b is a plot of μ_{Cr} versus μ_{O_2}. **Figure 40**a is similar to **Figure 5**. **Figure 40**c is a plot of $n_O/(n_{Fe} + n_{Cr})$ versus $n_{Cr}/(n_{Fe} + n_{Cr})$, where the size of the system is defined by $(n_{Fe} + n_{Cr})$. The coordinates of **Figure 40**c are known as *Jänecke coordinates*.

Figure 40c may be "folded up" to give the more familiar isothermal ternary section of **Figure 40**d plotted on the equilateral composition triangle.

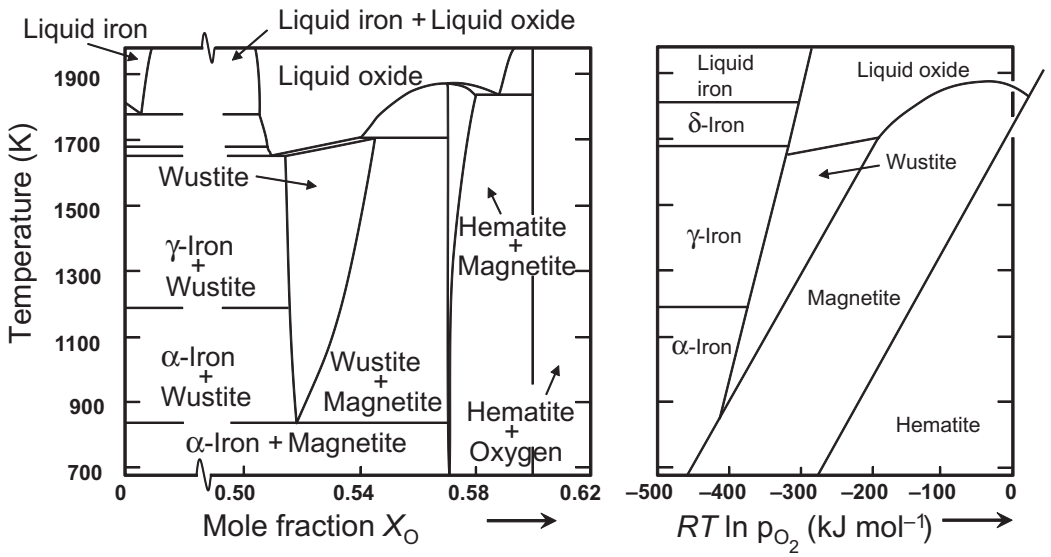

Figure 38 Corresponding T–X_O and $T - (\mu_{O_2} - \mu^0_{O_2})$ phase diagrams of the Fe–O system (after Muan and Osborn, 1965).

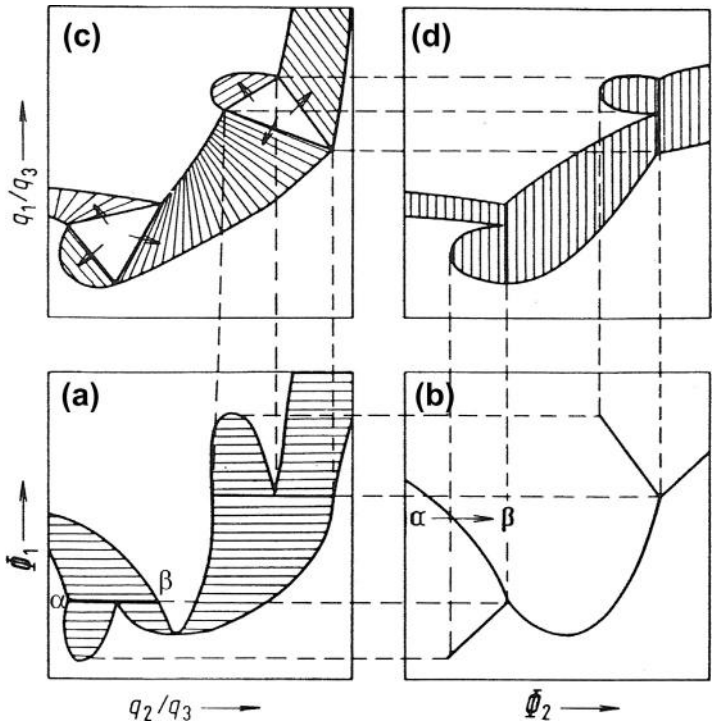

Figure 39 A corresponding set of phase diagrams for a *C*-component system when the potentials ϕ_4, ϕ_5, …, ϕ_{C+2} are constant (Pelton and Schmalzried, 1973).

3.7.6.1 Enthalpy-Composition Phase Diagrams

The *T*-composition phase diagram of the Mg–Si system is shown in **Figure 41**a. A corresponding phase diagram could be constructed by replacing the *T*-axis by the molar entropy because (*T*,*S*) is a corresponding pair, although such a diagram would not be of much practical interest. However, just as $(dS/dT) > 0$ at constant *P* and composition, so also is $(dH/dT) > 0$. Hence, an *H*-composition phase diagram will have the same geometry as an *S*-composition diagram. (This will be demonstrated more rigorously in Section 3.7.12.)

Figure 41b is the enthalpy-composition phase diagram corresponding to the *T*-composition diagram of **Figure 41**a. The *y*-axis is $(h - h_{25})$, where h_{25} is the molar enthalpy of the system in equilibrium at 25 °C. Referencing the enthalpy to h_{25} slightly distorts the geometry of the diagram because h_{25} is a function of composition. In particular, the tie-lines are no longer necessarily perfectly straight lines. However, this choice of reference renders the diagram more practically useful since the *y*-axis variable then directly gives the heat, which must be added, or removed, to heat, or cool, the system between 25 °C and any temperature *T*. The isothermal lines shown in **Figure 41**b are not part of the phase diagram but have been calculated and plotted to make the diagram more useful. It should be stressed that **Figure 41**b is a phase diagram section obeying all the geometrical rules of phase diagram sections discussed in Sections 3.7.1–3.7.4. It consists of ZPF lines and can be calculated using the same

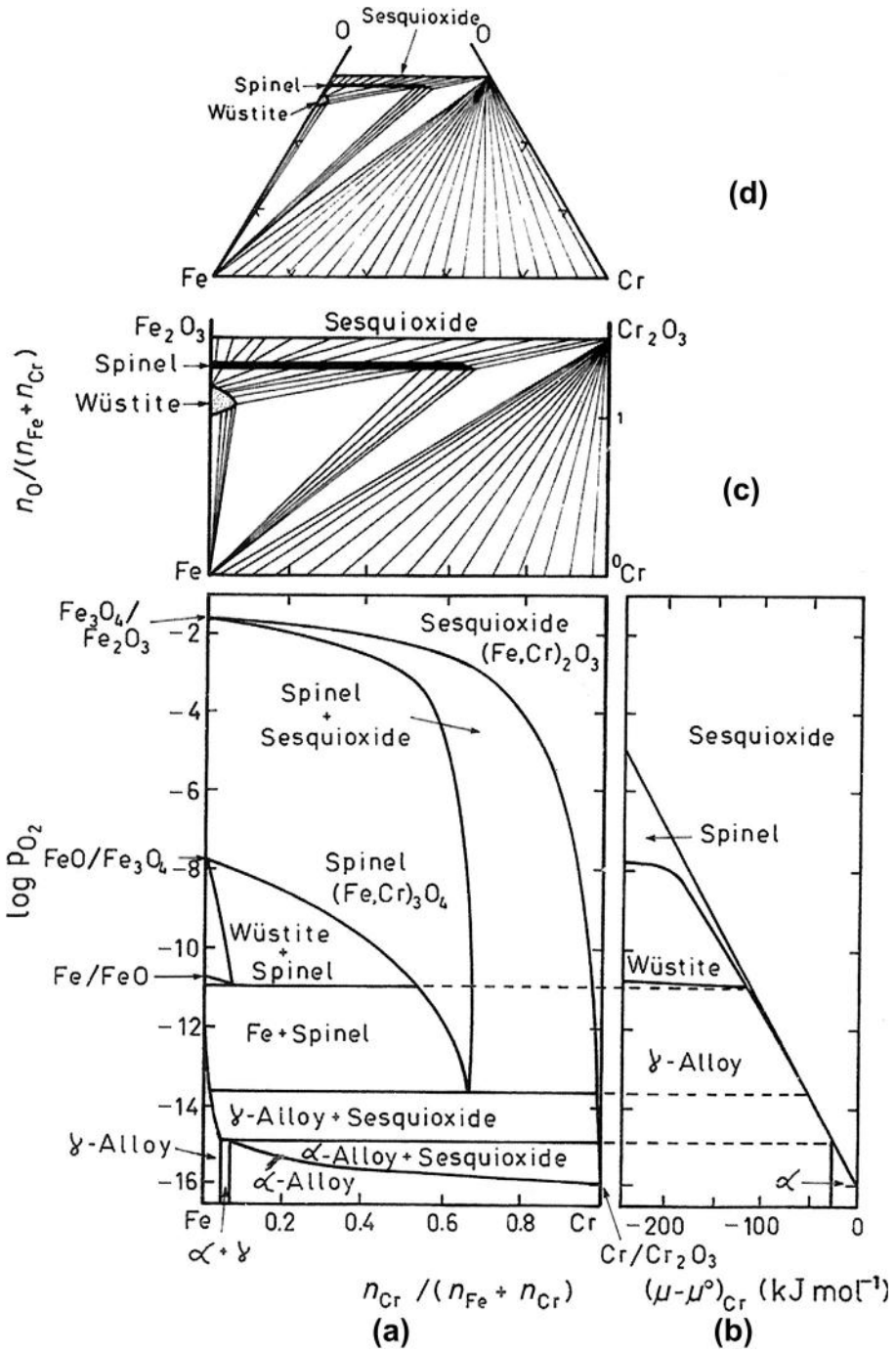

Figure 40 Corresponding phase diagrams of the Fe–Cr–O_2 system at 1300 °C (Pelton and Schmalzried, 1973).

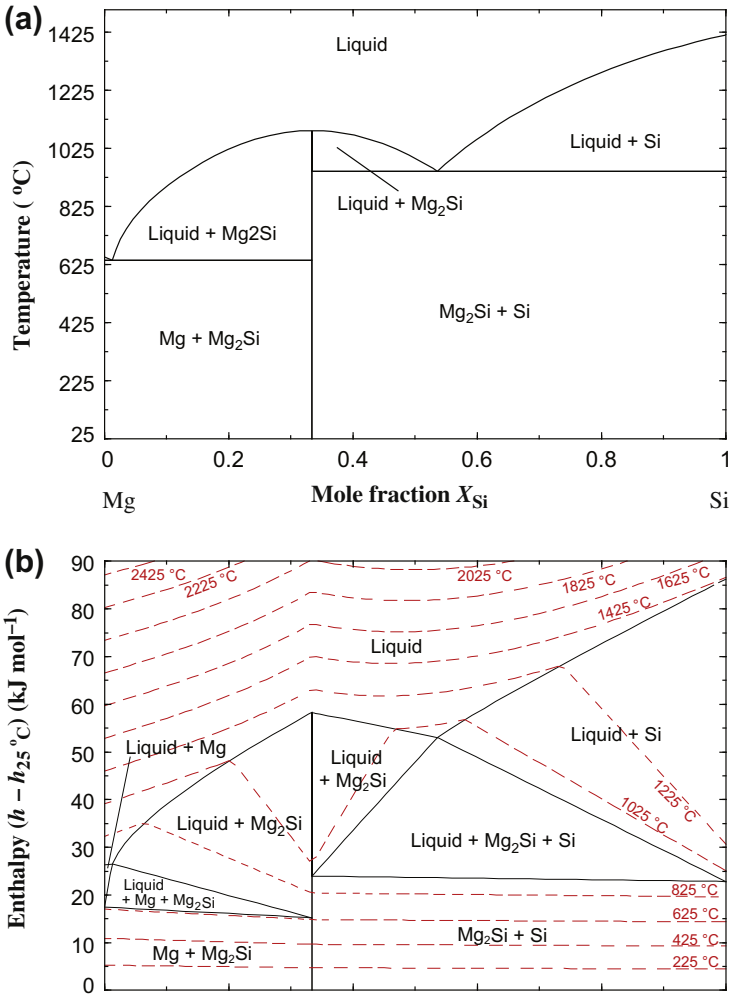

Figure 41 Corresponding *T*-composition and enthalpy-composition phase diagrams of the Mg–Si system at $P = 1$ bar. The enthalpy axis is referred to the enthalpy of the system at equilibrium at 25 °C (see FactSage). (For color version of this figure, the reader is referred to the online version of this book.)

algorithm as for any other phase diagram section as discussed in Section 3.7.4.1. Note that the three-phase tie-triangles are isothermal.

Another *H*-composition phase diagram is shown in **Figure 3**b for the Zn–Mg–Al system along the isoplethal section where $X_{Zn} = 0.1$.

3.7.7 The Thermodynamics of General Phase Diagram Sections

This section provides a more rigorous derivation of the geometry of general phase diagram sections that was discussed in Sections 3.7.2–3.7.6.

In Section 3.2.8.2, a general auxiliary function G' was introduced. Let us now define an even more general auxiliary function, B, as follows:

$$B = U - \sum_{i=1}^{m} \phi_i q_i \quad 0 \leq m \leq (C+2) \tag{154}$$

where the ϕ_i and q_i include all corresponding pairs in **Table 1** (if $m = 0$, then $B = U$). Following the same reasoning as in Section 3.2.8.2, we obtain for a system at equilibrium:

$$\mathrm{d}B = -\sum_{1}^{m} q_i \mathrm{d}\phi_i + \sum_{m+1}^{C+2} \phi_i \mathrm{d}q_i \tag{155}$$

and the equilibrium state at constant ϕ_i $(0 \leq i \leq m)$ and q_i $(m+1 \leq i \leq C+2)$ is approached by minimizing B:

$$\mathrm{d}B_{\phi_i(0\leq i\leq m),q_i(m+1\leq i\leq C+2)} \leq 0 \tag{156}$$

Figure 42 is a plot of the ϕ_1–ϕ_2–ϕ_3 surfaces of two phases, α and β, in a C-component system when ϕ_4, ϕ_5, …, ϕ_{C+2} are all held constant. For example, in a one-component system, **Figure 42** would be a plot of the P–T–μ surfaces. Let us now choose a pair of values ϕ_1 and ϕ_2 and derive the condition for equilibrium. Since all potentials except ϕ_3 are now fixed, the appropriate auxiliary function, from Eqns 154 and 70, is $B = q_3\phi_3$. (See also Eqns 73 and 76). Furthermore, let us fix the size of the system by setting q_3 constant. Then, from Eqn 156, the equilibrium state for any given pair of values of ϕ_1 and ϕ_2 is given by setting $\mathrm{d}B = q_3\mathrm{d}\phi_3 = 0$, that is by minimizing ϕ_3. This is illustrated in **Figure 42**, where the base plane of the figure is the ϕ_1–ϕ_2 phase diagram of the system at constant ϕ_4, ϕ_5, ……, ϕ_{C+2}. For example, in a one-component system, if ϕ_1, ϕ_2, ϕ_3 are P, T, μ, respectively, then the P–T phase diagram is given by minimizing μ, the molar Gibbs energy of the system. Clearly, therefore, a ϕ_1–ϕ_2 diagram at constant ϕ_4, ϕ_5, ……, ϕ_{C+2} is single-valued.

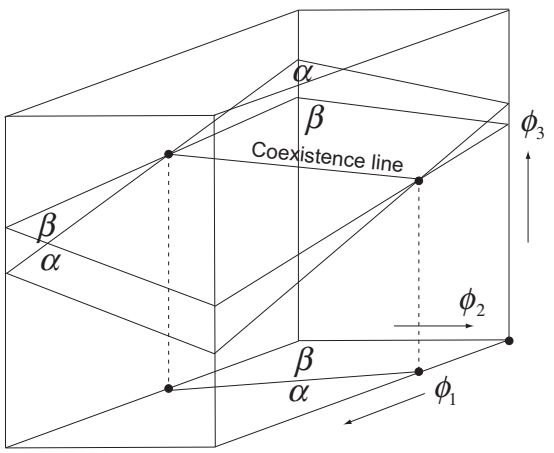

Figure 42 ϕ_1–ϕ_2–ϕ_3 surfaces of α and β phases in a C-component system when ϕ_4, ϕ_5, …, ϕ_{C+2} are constant (Reprinted with permission from Hillert, 2008).

As another example, consider the $T - \mu_{O_2}$ phase diagram of the Fe–O system at constant hydrostatic pressure in **Figure 38**. The potentials of the system are T, P, μ_{O_2} and μ_{Fe}. At constant P, and for any given values of T and μ_{O_2}, the equilibrium state of the system is given by minimizing μ_{Fe}. Similarly, the predominance diagram of the Cu–SO_2–O_2 system in **Figure 9** can be calculated by minimizing μ_{Cu}, which can be shown to be equivalent to the procedure described in Section 3.2.4.2.

A general ϕ_1–ϕ_2 phase diagram at constant ϕ_4, ϕ_5, ……, ϕ_{C+2} was shown in **Figure 39**b. The size of the system is defined by fixing q_3. We wish now to show that when **Figure 39**b is "opened up" by replacing ϕ_2 by q_2 to give the corresponding phase diagram in **Figure 39**a, the sequence of phase regions encountered in moving horizontally across **Figure 39**a is the same as in **Figure 39**b. For example, when the two-phase ($\alpha + \beta$) line in **Figure 39**b is "opened" up to form the two-phase ($\alpha + \beta$) region in **Figure 39**a, the α and β phases remain on the left and right sides, respectively, of the two-phase region.

We first derive the general *thermodynamic stability criterion* for a single-phase region. Imagine two bordering microscopic regions, I and II, within a homogeneous phase and suppose that a local fluctuation occurs in which an amount $dq_n > 0$ of the extensive property q_n is transferred from region I to region II at constant ϕ_i ($0 \le i \le m$) and constant q_i ($m + 1 \le i \le C + 2$), where $i \ne n$. Suppose that, as a result of the transfer, ϕ_n increases in region I and decreases in region II, that is, that $(d\phi_n/dq_n) < 0$. A potential gradient is thus set up with $\phi_n^{I} > \phi_n^{II}$. From Eqn 155, further transfer of q_n from region I to II then results in a decrease in $B : dB = (\phi^{II} - \phi^{I})dqn < 0$. From Eqn 156, equilibrium is approached by minimizing B. Hence, the fluctuation grows, with continual transfer from region I to II. That is, the phase is unstable. Therefore, the criterion for a phase to be thermodynamically stable is:

$$d\phi_n/dq_n > 0 \tag{157}$$

for any choice of constant ϕ_i or q_i constraints ($i \ne n$). Since $\phi_n = (\partial B/\partial q_n)$, the stability criterion can also be written as:

$$\left(\partial^2 B/\partial q_n^2\right)_{\phi_{i(0\le i\le m)},\, q_{i(m+1\le i\le C+2);i\ne n}} > 0 \tag{158}$$

An important example is illustrated in **Figure 18** for the solid phase of the Au–Ni system. In this case, the appropriate auxiliary function is the Gibbs energy, G. In the central composition regions of the Gibbs energy curves in **Figure 18**, between the spinodal points indicated by the letter s, $(\partial^2 G/\partial n_{Ni}^2)_{T,P,n_{Fe}} < 0$. Hence, at compositions between the spinodal points, microscopic composition fluctuations will grow since this leads to a decrease in the total Gibbs energy of the system. Hence, the phase is unstable and phase separation can occur by spinodal decomposition as discussed in Chapter 7 of this volume. Other well-known examples of the stability criterion are $(dT/dS) > 0$ (entropy increases with temperature), and $(dP/d(-V)) > 0$ (pressure increases with decreasing volume).

Returning now to **Figure 39**, it can be seen from Eqn 157 that moving horizontally across a single-phase region in **Figure 39**b corresponds to moving in the same direction across the same region in **Figure 39**a. Furthermore, in the two-phase ($\alpha + \beta$) region, suppose that ϕ_2 is increased by an amount $d\phi_2 > 0$ keeping all other potentials except ϕ_3 constant, thereby displacing the system into the single-phase β region. From the Gibbs–Duhem Equation 75:

$$d\phi_3^{\alpha} = -(q_2/q_3)^{\alpha} d\phi_2 \quad \text{and} \quad d\phi_3^{\beta} = -(q_2/q_3)^{\beta} d\phi_2 \tag{159}$$

where $(q_2/q_3)^{\alpha}$ and $(q_2/q_3)^{\beta}$ are the values at the boundaries of the two-phase region.

Since, as has just been shown, the equilibrium state is given by minimizing ϕ_3, it follows that:

$$\mathrm{d}(\phi_3^{\beta} - \phi_3^{\alpha})/\mathrm{d}\phi_2 = (q_2/q_3)^{\alpha} - (q_2/q_3)^{\beta} < 0 \tag{160}$$

Hence, the α-phase and β-phase region lie to the left and right, respectively, of the $(\alpha + \beta)$ region in **Figure 39**a, and **Figure 39**a is single-valued.

Since the stability criterion also applies when extensive variables are held constant, it can similarly be shown that when **Figure 39**a is "opened up" by replacing the ϕ_1 axis by q_1/q_3 to give **Figure 39**c, the sequence of the phase regions encountered as the diagram is traversed vertically is the same as in **Figure 39**a, and that **Figure 39**c is single-valued. Finally, it can be shown that the phase diagrams will remain single-valued if a constant ϕ_4 is replaced by q_4/q_3. **Figure 39**a, for example, is a section at constant ϕ_4 through a three-dimensional ϕ_1–ϕ_4–(q_2/q_3) diagram, which may be "opened up" by replacing ϕ_4 by (q_4/q_3) to give a ϕ_1–$(q_4/q_3) - (q_2/q_3)$ diagram, which is necessarily single-valued because of the stability criterion. Hence, sections through this diagram at constant (q_4/q_3) will also be single-valued.

Consider now the node in a general phase diagram section shown in **Figure 33**. At any point on either phase boundary of the $(\alpha_1 + \alpha_2 + \ldots + \alpha_N)$ region, one additional phase, β or γ, becomes stable. Since there is no thermodynamic reason why more than one additional phase should become stable at exactly the same point, the Law of Adjoining Phase Regions is evident. These phase boundaries intersect at the node, below which there must clearly be a region in which β and γ are simultaneously stable. If the *x*-axis of the diagram is an extensive variable, then this region will have a finite width since there is no thermodynamic reason for the β-phase to become unstable at exactly the same point that the γ-phase becomes stable. It then follows that exactly four boundaries meet at a node. Of course, if the *x*-axis is a potential variable, then the two-phase boundaries of the $(\alpha_1 + \alpha_2 + \ldots + \alpha_N + \beta + \gamma)$ region will necessarily be coincident.

3.7.7.1 Schreinemakers' Rule

Schreinemakers' Rule (Schreinemakers, 1915; Pelton, 1995), which was discussed in Section 3.7.4, will now be proven for the general case. Consider the point *p* in **Figure 33**, which lies in the $(\alpha_1 + \alpha_2 + \ldots + \alpha_N + \gamma)$ region arbitrarily close to the node. If precipitation of γ were prohibited by kinetic constraints, point *p* would lie in the $(\alpha_1 + \alpha_2 + \ldots + \alpha_N + \beta)$ region since it lies below the dashed extension of the phase boundary line as shown in the figure. Let *B* be the appropriate auxiliary function. If precipitation of γ is prohibited, then $\mathrm{d}B/\mathrm{d}n^{\beta} < 0$, where $\mathrm{d}n^{\beta}$ is the amount of β-phase (of fixed composition) which precipitates. That is, precipitation of β decreases *B*. If γ is permitted to precipitate, then precipitation of β is prevented. Therefore,

$$\frac{\mathrm{d}}{\mathrm{d}n^{\gamma}}\left(\frac{\mathrm{d}B}{\mathrm{d}n^{\beta}}\right) > 0 \tag{161}$$

Since the order of differentiation does not matter:

$$\frac{\mathrm{d}}{\mathrm{d}n^{\beta}}\left(\frac{\mathrm{d}B}{\mathrm{d}n^{\gamma}}\right) > 0 \tag{162}$$

Hence, the extension of the other boundary of the $(\alpha_1 + \alpha_2 + \ldots + \alpha_N)$ region must pass into the $(\alpha_1 + \alpha_2 + \ldots + \alpha_N + \beta)$ region as shown in **Figure 33**. Similarly, it can be shown that if the extension of

one boundary of the $(\alpha_1 + \alpha_2 + \ldots + \alpha_N)$ region passes into the $(\alpha_1 + \alpha_2 + \ldots + \alpha_N + \beta + \gamma)$ region, then so must be the extension of the other (Pelton, 1995).

3.7.8 Interpreting Oxide Phase Diagrams

Three phase diagrams for the Fe–Si–O_2 system are shown in **Figures 43–45**. Diagrams of these types are often a source of confusion.

Figure 43 is often called the "phase diagram of the Fe_3O_4–SiO_2 system." However, it is not a binary phase diagram, nor is it a quasibinary phase diagram. Rather, it is an isoplethal section across the

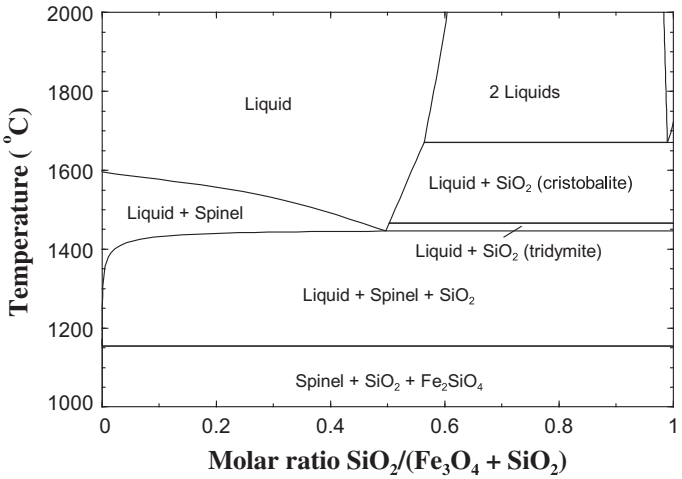

Figure 43 Isoplethal section across the Fe_3O_4–SiO_2 join of the Fe–Si–O_2 system. ($P = 1$ bar) (see FactSage).

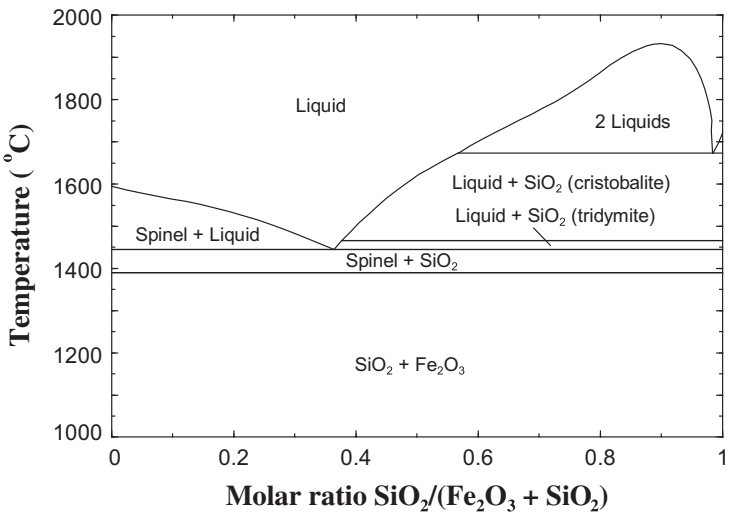

Figure 44 "Fe_2O_3–SiO_2 phase diagram in air ($p_{O_2} = 0.21$ bar)" (see FactSage).

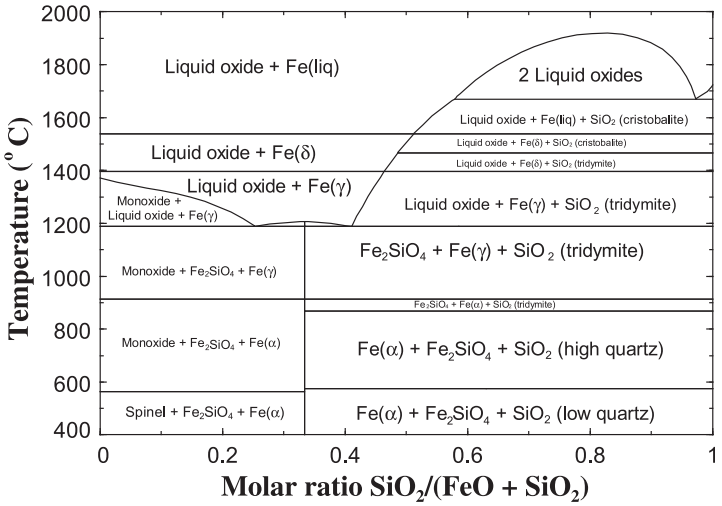

Figure 45 "FeO–SiO_2 phase diagram at Fe saturation" (see FactSage).

Fe_3O_4–SiO_2 joint of the Fe–Si–O_2 composition triangle. As with any isoplethal section, tie-lines in **Figure 43** do not necessarily lie in the plane of the diagram. That is, the *x*-axis gives only the overall composition of the system, not the compositions of individual phases. The lever rule does not apply. In the scheme of Section 3.7.5, **Figure 43** is described as follows:

$$\begin{aligned}
&\phi_i: \quad \underline{T} \quad \underline{P} \quad \mu_{Fe_3O_4} \quad \mu_{SiO_2} \quad \mu_{O_2} \\
&q_i: \quad S \quad -V \quad \underline{n_{Fe_3O_4}} \quad \underline{n_{SiO_2}} \quad \underline{n_{O_2}} \\
&\text{Size}: (n_{Fe_3O_4} + n_{SiO_2}) \\
&\text{Phase diagram variables}: T, P, n_{SiO_2}/(n_{Fe_3O_4} + n_{SiO_2}), n_{O_2}/(n_{Fe_3O_4} + n_{SiO_2})
\end{aligned}$$

with $n_{O_2}/(n_{Fe_3O_4} + n_{SiO_2}) = 0$. The components have been defined judiciously as Fe_3O_4–SiO_2–O_2 rather than Fe–Si–O_2. While this is not necessary, it clearly simplifies the description.

Figure 44 is often called the "Fe_2O_3–SiO_2 phase diagram at constant p_{O_2}." This diagram is actually a ternary section along a constant p_{O_2} line as shown schematically in **Figure 46**. Note that the position of this line for any given p_{O_2} will vary with temperature. At lower temperatures, the line approaches the Fe_2O_3–SiO_2 join. Since p_{O_2} is the same in all phases at equilibrium, the compositions of all phases, as well as the overall composition, lie along the constant p_{O_2} line. Hence, **Figure 44** has the same topology as binary *T*-composition phase diagrams. All tie-lines lie in the plane of the diagram as illustrated in **Figure 46**, and the lever rule applies. In the scheme of Section 3.7.5, **Figure 44** is described as

$$\begin{aligned}
&\phi_i: \quad \underline{T} \quad \underline{P} \quad \mu_{Fe_2O_3} \quad \mu_{SiO_2} \quad \underline{\mu_{O_2}} \\
&q_i: \quad S \quad P \quad \underline{n_{Fe_2O_3}} \quad \underline{n_{SiO_2}} \quad n_{O_2} \\
&\text{Size}: (n_{Fe_2O_3} + n_{SiO_2}) \\
&\text{Phase diagram variables}: T, P, n_{SiO_2}/(n_{Fe_2O_3} + n_{SiO_2}), \mu_{O_2}
\end{aligned}$$

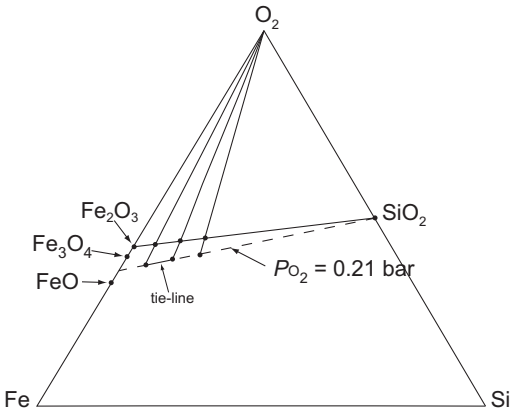

Figure 46 Constant p_{O_2} line in the Fe–Si–O_2 system illustrating the construction and interpretation of **Figure 44**.

The phase boundary lines in **Figure 44** give the ratio $n_{SiO_2}/(n_{Fe_2O_3} + n_{SiO_2})$ in the individual phases of the Fe_2O_3–SiO_2–O_2 system at equilibrium. However, they do not give the total composition of the phases, which may be deficient in oxygen. That is, some of the Fe may be present in a phase as FeO. The diagram may also be visualized as a projection of the equilibrium phase boundaries from the O_2-corner of the composition triangle onto the Fe_2O_3–SiO_2 join as illustrated in **Figure 46**. From an experimental standpoint, the x-axis represents the relative amounts of an initial mixture of Fe_2O_3 and SiO_2 that was charged into the apparatus at room temperature and that was subsequently equilibrated with air at higher temperatures.

Figure 45 is often called the "FeO–SiO_2 phase diagram at Fe saturation." Usually, this diagram is drawn without indicating the presence of Fe in each phase field although metallic Fe is always present as a separate phase. The horizontal lines in **Figure 45**, which indicate the allotropic transformation temperatures and melting point of Fe, are also generally not drawn. Diagrams such as **Figure 45** are best regarded and calculated as isoplethal sections with excess Fe. **Figure 45** was calculated by the following scheme:

$$\begin{aligned}
&\phi_i: \quad \underline{T} \quad \underline{P} \quad \mu_{FeO} \quad \mu_{SiO_2} \quad \mu_{Fe} \\
&q_i: \quad S \quad -V \quad \underline{n_{FeO}} \quad \underline{n_{SiO_2}} \quad \underline{n_{Fe}} \\
&\text{Size}: (n_{FeO} + n_{SiO_2}) \\
&\text{Phase diagram variables}: T, \quad P, n_{SiO_2}/(n_{FeO} + n_{SiO_2}), n_{Fe}/(n_{FeO} + n_{SiO_2})
\end{aligned}$$

with $n_{Fe}/(n_{FeO} + n_{SiO_2}) = 0.0001$. That is, the components of the system have been defined as FeO, SiO_2 and O_2 with a sufficient excess of Fe so as to always give a metallic phase at equilibrium. Note that the phase boundary compositions in **Figure 45** give only the ratio $n_{SiO_2}/(n_{FeO} + n_{SiO_2})$ in each phase but not the total compositions of the phases, which may contain an excess or a deficit of iron relative to the FeO–SiO_2 join. In this system, the solubility of Si in Fe is very small, and so has a negligible effect on the phase diagram. However, in other systems such as Fe–Zn–O_2, the equilibrium metal phase could actually contain more Zn than Fe, depending upon the conditions.

3.7.9 Choice of Components and Choice of Variables

As was discussed in Section 3.3, the components of a given system may be defined in different ways. A judicious selection can simplify the choice of variables for a phase diagram as has just been illustrated in Section 3.7.8. As another example, the selection of variables for the isothermal log p_{SO_2} − log p_{O_2} phase diagram of the Cu–SO_2–O_2 system in **Figure 9** according to the scheme of Section 3.7.5 is clearly simplified if the components are formally selected as Cu–SO_2–O_2 rather than, for example, as Cu–S–O.

In certain cases, different choices of variables can result in different phase diagrams. For the same system as in **Figure 9**, suppose that we wish to plot an isothermal predominance diagram with log p_{SO_2} as y-axis but with log a_{Cu} as the x-axis. The gas phase will consist principally of O_2, S_2 and SO_2 species. As the composition of the gas phase varies at constant total pressure from pure O_2 to pure S_2, the partial pressure of SO_2 passes through a maximum where the gas phase consists mainly of SO_2. Therefore, for the phase diagram to be single-valued, the log p_{SO_2} axis must encompass gaseous mixtures which consist either mainly of (O_2 + SO_2) or of (SO_2 + S_2), but not both. Let us define the components as Cu–SO_2–O_2 and choose the phase diagram variables as follows:

$$\begin{array}{lccccc} \phi_i: & \underline{T} & \underline{P} & \underline{\mu_{Cu}} & \underline{\mu_{SO_2}} & \mu_{O_2} \\ q_i: & S & -V & n_{Cu} & n_{SO_2} & \underline{n_{O_2}} \end{array}$$

$$\text{Size}: n_{O_2}$$

$$\text{Phase diagram variables}: T,\ P,\ \mu_{Cu},\ \mu_{SO_2},\ n_{O_2}$$

As p_{SO_2} increases at constant T, P and n_{O_2}, p_{O_2} decreases while p_{S_2} always remains small. The phase diagram then essentially encompasses only the Cu–SO_2–O_2 subsystem of the Cu–S_2–O_2 system. A phase field for Cu_2O will appear on the diagram, for example, but there will be no field for Cu_2S. If, on the other hand, we choose the components as Cu–SO_2–S_2 with the size of the system defined as n_{S_2} = constant, then p_{S_2} varies along the p_{SO_2} axis while p_{O_2} always remains small. The phase diagram then encompasses only the Cu–SO_2–S_2 subsystem. A phase field for Cu_2S appears, but there will be no field for Cu_2O.

This example serves to illustrate again how the procedure for choosing variables given in Section 3.7.5 provides sufficient conditions for a phase diagram to be single-valued.

3.7.10 Phase Diagrams of Reciprocal Systems

A section at $T = 750\ ^\circ C$ and $P = 1.0$ bar of the *reciprocal salt system*, NaCl–$CaCl_2$–NaF–CaF_2 is shown in **Figure 47**. A reciprocal salt system is one consisting of two or more cations and two or more anions. Since excess Na, Ca, F and Cl are virtually insoluble in the ionic salts, this system is, to a very close approximation, a quasi-ternary isoplethal section of the Na–Ca–Cl–F system in which:

$$(n_F + n_{Cl}) = (2n_{Ca} + n_{Na}) \tag{163}$$

That is, the total cationic charge is equal to the total anionic charge. The compositions of all phases lie in the plane of the diagram and the lever rule applies.

The corners of the composition square in **Figure 47** represent the pure salts, while the edges of the square represent compositions in common-ion quasi-binary systems. The choice of phase diagram

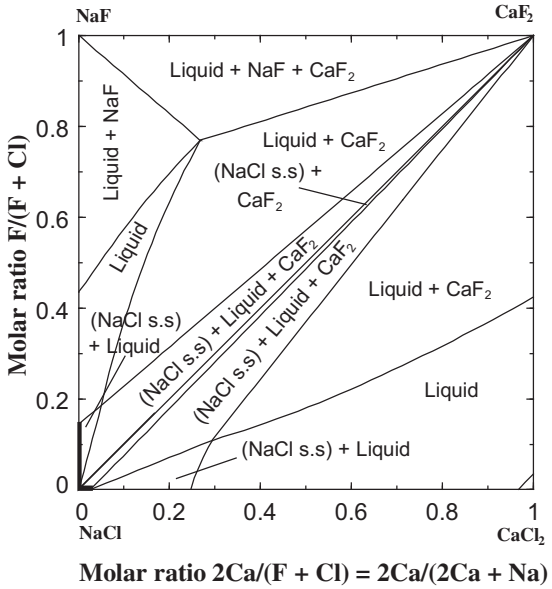

Figure 47 Phase diagram at $T = 750\ ^{\circ}C$ and $P = 1$ bar of the reciprocal system NaCl–$CaCl_2$–NaF–CaF_2 (see FactSage).

variables is most simply formulated, using the procedure of Section 3.7.5, as follows:

$$\phi_i: \quad \underline{T} \quad \underline{P} \quad \mu_{Na} \quad \mu_{Ca} \quad \mu_F \quad \mu_{Cl}$$

$$q_i: \quad S \quad -V \quad \underline{n_{Na}} \quad \underline{n_{Ca}} \quad \underline{n_F} \quad \underline{n_{Cl}}$$

$$\text{Size}: (n_F + n_{Cl}) = (2n_{Ca} + n_{Na})$$

$$\text{Phase diagram variables}: T, \ P, n_F/(n_F + n_{Cl}), 2n_{Ca}/(2n_{Ca} + n_{Na}), (2n_{Ca} + n_{Na})/(n_F + n_{Cl}) = 1$$

The axis variables of **Figure 47** are sometimes called "equivalent ionic fractions", in which the number of moles of each ion is weighted by its absolute charge. (Note that if Na, Ca, F or Cl were actually significantly soluble in the salts, the diagram could still be plotted as in **Figure 47**, but it would then no longer be a quasi-ternary section and tie-lines would not necessarily lie in the plane of the diagram, nor would the lever rule apply.)

3.7.11 Choice of Variables to Ensure Straight Tie-lines

Figure 47 could be drawn with the axis variables chosen instead as $n_F/(n_F + n_{Cl})$ and $n_{Ca}/(n_{Ca} + n_{Na})$, that is, as molar ionic fractions rather than equivalent ionic fractions.

In this case, the diagram would be a distorted version of **Figure 47**, but would still be a valid phase diagram obeying all the geometrical rules. However, tie-lines in two-phase regions would no longer be straight lines. That is, a straight line joining the compositions of two phases at equilibrium would not pass through the overall composition of the system. It is clearly desirable from a practical standpoint that tie-lines be straight.

It can be shown through simple mass balance considerations (Pelton and Thompson, 1975) that the tie-lines of a phase diagram, in which both axes are composition variables, will only be straight lines if the denominators of the two composition variable ratios are the same. This is the case in **Figure 47** where the denominators are the same because of the condition of Eqn 163. For another example, see **Figure 39**c. It can thus be appreciated that the procedure of Section 3.7.5 provides a sufficient condition for tie-lines to be straight by the stratagem of normalizing all composition variables with respect to the same system "size."

It can also be shown (Pelton and Thompson, 1975) that ternary phase diagram sections plotted on a composition triangle always have straight tie-lines.

3.7.12 Other Sets of Corresponding Variable Pairs

The set of corresponding variable pairs in **Table 1**, Section 3.7.1 is only one of the several possible sets.

Substituting S from Eqn 71 into the Gibbs–Duhem Equation 75 and rearranging terms yields:

$$-H\mathrm{d}(1/T) - (V/T)\mathrm{d}P + \sum n_i \mathrm{d}(\mu_i/T) = 0 \qquad (164)$$

Hence, another set of corresponding variable pairs is that given in **Table 2**.

With this set of conjugate variable pairs replacing those in **Table 1**, the same procedure as described in Section 3.7.5 can be used to choose variables to construct single-valued phase diagrams. For example, the procedure for the H-composition phase diagram in **Figure 41**b is as follows:

$$\begin{aligned}
&\phi_i: \quad 1/T \quad \underline{P} \quad \mu_{\mathrm{Mg}}/T \quad \mu_{\mathrm{Si}}/T \\
&q_i: \quad \underline{-H} \quad -V/T \quad \underline{n_{\mathrm{Mg}}} \quad \underline{n_{\mathrm{Si}}} \\
&\text{Size}: \left(n_{\mathrm{Mg}} + n_{\mathrm{Si}}\right) \\
&\text{Phase diagram variables}: H,\ P,\ n_{\mathrm{Mg}}/\left(n_{\mathrm{Mg}} + n_{\mathrm{Si}}\right)
\end{aligned}$$

This demonstrates that **Figure 41**b is, in fact, a single-valued phase diagram. Although, in this particular case, an S-composition phase diagram would also be single-valued, and very similar in form to **Figure 41**b, H cannot simply be substituted for S in **Table 1** in all cases.

Many other sets of conjugate variable pairs can be obtained through appropriate thermodynamic manipulation. The set shown in **Table 2** and many other such sets have been discussed by Hillert (1997). For example, $(-A/T,T/P)$, $(-TU/P,1/T)$, $(\mu_i/T,n_i)$ is one such set. In conjunction with the selection rules of Section 3.7.5, all these sets of conjugate pairs can be used to construct single-valued phase diagram sections. However, these diagrams would probably be of very limited practical utility.

Table 2 Corresponding pairs of potentials ϕ_i and extensive variables q_i

ϕ_i:	$1/T$	P	μ_i/T	μ_2/T	…	μ_C/T
q_i:	$-H$	$-V/T$	n_1	n_2	…	n_C

3.7.13 Extension Rules for Polythermal Projections

An extension rule for the univariant lines on polythermal projections is illustrated in **Figure 27** at point A. At any intersection point of three univariant lines, the extension of each univariant line passes between the other two. The proof, although straightforward, is rather lengthy and so will not be reproduced here.

3.8 Thermodynamic Databases for the Computer Calculation of Phase Diagrams

As discussed in Section 3.1, the past 25 years have witnessed a rapid development of large evaluated optimized thermodynamic databases and of software that accesses these databases to calculate phase diagrams by Gibbs energy minimization.

The databases for multicomponent solution phases are prepared by first developing an appropriate mathematical model, based upon the structure of the solution, which gives the thermodynamic properties as functions of temperature and composition for every phase of a system. Next, all available thermodynamic data (calorimetric data, activity measurements, etc.) and phase equilibrium data from the literature for the entire system are evaluated and simultaneously "optimized" to obtain one set of critically evaluated self-consistent parameters of the models for all phases in two-component, three-component and, if available, higher order systems. Finally, the models are used to estimate the properties of multicomponent solutions from the databases of parameters of lower order subsystems. Recently, experimental data are being supplemented by "virtual data" from first principles calculations; for a review, see Turchi et al. (2007).

The optimized model equations are consistent with thermodynamic principles and with theories of solutions. The phase diagrams can be calculated from these thermodynamic equations, and so one set of self-consistent equations describes simultaneously all the thermodynamic properties and the phase diagrams. This technique of analysis greatly reduces the amount of experimental data needed to fully characterize a system. All data can be tested for internal consistency. The data can be interpolated and extrapolated more accurately. All the thermodynamic properties and the phase diagram can be represented and stored by means of a relatively small set of coefficients.

This technique permits the estimation of phase diagrams of multicomponent systems based only upon data from lower order subsystems and allows any desired phase diagram section or projection to be calculated and displayed rapidly. In **Figure 48** is a calculated phase diagram section for a six-component system, which might be of interest in the design of new Mg alloys. This diagram was calculated on a laptop computer in approximately 2 min. Hence, many sections of a multicomponent system can be quickly generated for study.

The computer calculation of phase diagrams present many advantages. For example, metastable phase boundaries can be readily calculated by simply removing one or more stable phases from the calculation. An example is shown in **Figure 49** where the metastable liquid miscibility gap was calculated. Other metastable phase boundaries such as the extension of a liquidus below the eutectic temperature can be calculated similarly. Another advantage is the possibility of calculating phase compositions at points on an isoplethal section. For instance, compositions of individual phases at equilibrium cannot be read directly from **Figure 48**. However, with the calculated diagram on the computer screen, and with appropriate software (see FactSage), one can simply place the cursor at any desired point on the diagram and "click" in order to calculate the amounts and compositions of all phases in equilibrium at that point. Other software can follow the course of equilibrium cooling or of nonequilibrium "Scheil–Gulliver cooling" as will be discussed in Section 3.9. And, of course, the thermodynamic databases permit the

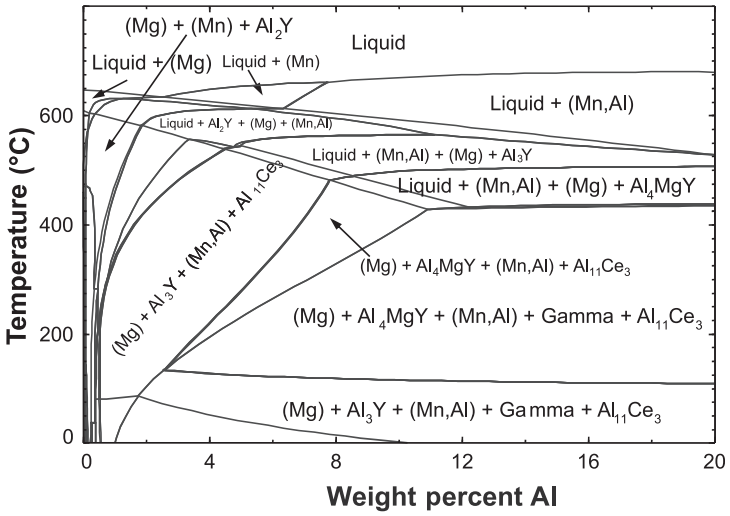

Figure 48 Isoplethal section of the Mg–Al–Ce–Mn–Y–Zn system at 0.05% Ce, 0.5% Mn, 0.1% Y and 1.0% Zn (weight percentage) at $P = 1$ bar (see FactSage).

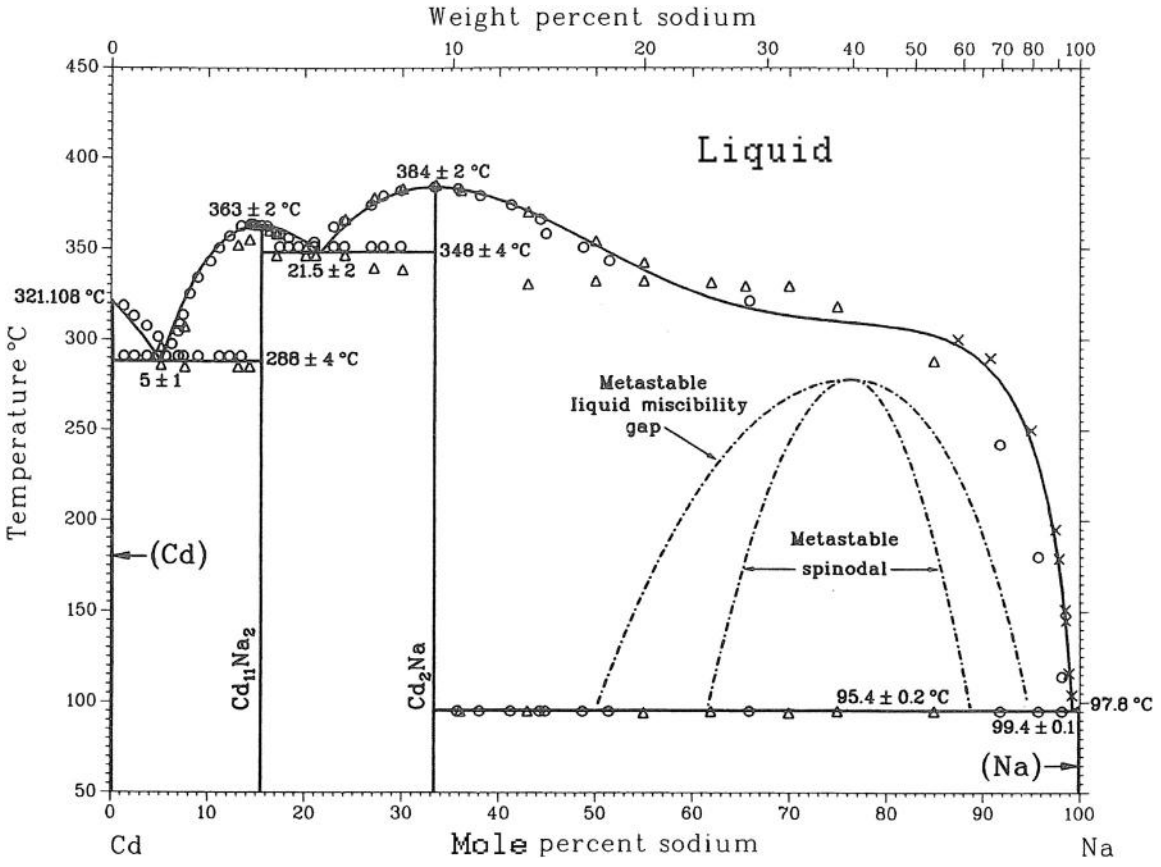

Figure 49 Cd–Na phase diagram at $P = 1$ bar calculated from optimized thermodynamic parameters showing experimental data points: ○ Kurnakow and Kusnetzow (1907), △ Mathewson (1906), X Weeks and Davies (1964).

calculation of chemical potentials, which are essential for calculating kinetic phenomena such as diffusion. Coupling thermodynamic databases and software with databases of diffusion coefficients and software for calculating diffusion (as with the Dictra program of Thermocalc (see Thermocalc)) provides a powerful tool for the study of the heat treatment of alloys for instance.

Among the largest integrated database computing systems with applications in metallurgy and material science are Thermocalc, FactSage, MTDATA and Pandat (see list of websites). These systems all combine large evaluated and optimized databases with advanced Gibbs energy minimization software. As well, the SGTE group (see SGTE) has developed a large database for metallic systems.

All these databases are extensive. For example, the SGTE alloy database contains optimized data for 78 components, involving hundreds of solution phases and stoichiometric compounds, 350 completely assessed and optimized binary systems and 120 optimized ternary systems. Equally extensive optimized databases have been developed for systems of oxides, salts, etc.

It is beyond the scope of this chapter to give a detailed account of the techniques of thermodynamic evaluation, optimization and modeling. The following sections are intended only to provide a general idea of what is involved in order to permit an appreciation of the advantages of the technique and of its limitations.

3.8.1 Thermodynamic/Phase Diagram Optimization of a Binary System

As a simple example of the optimization/evaluation of a binary system, we shall consider the Cd–Na system. The phase diagram, with points measured by several authors (Mathewson, 1906; Kurnakow and Kusnetzow, 1907; Weeks and Davies, 1964) is shown in **Figure 49**. From electromotive force measurements on alloy concentration cells, several authors have measured the activity coefficient of Na in liquid alloys. The data are shown in **Figure 50** at 400 °C. From the temperature dependence of $\mu^E_{Na} = RT\ln\gamma_{Na}$, the partial enthalpy of Na in the liquid was obtained via Eqn 114. The results are shown in **Figure 51**. Also, h^E of the liquid has been measured by Kleinstuber (1961) by direct calorimetry.

The system contains four solid phases, Cd, Na, $Cd_{11}Na_2$ and Cd_2Na, which are all assumed to be stoichiometric compounds. We seek expressions for the Gibbs energy of every solid phase and the liquid phase as functions of T and, in the case of the liquid, of composition. An expression for the Gibbs energy of a phase as a function of T and composition constitutes a complete thermodynamic description of the phase since all other thermodynamic properties can be calculated from G by taking the appropriate derivatives.

For pure solid elemental Cd, $h^o_{298} = 0.0$ by convention. From third law measurements (see Section 3.2.5.3), $s^o_{298} = 51.800$ J mol^{-1} K^{-1} (see SGTE). The heat capacity has been measured as a function of T and can be represented by the empirical equation:

$$c_P = 22.044 + 0.012548\ T + 0.139\left(10^5\right)T^{-2} \quad \text{J mol}^{-1}\text{K}^{-1} \tag{165}$$

Hence, from Eqns 18, 19 and 57, the following expression is obtained for the molar Gibbs energy of solid Cd:

$$\mu^{o(s)}_{Cd} = -7083 + 99.506\ T - 6.274\left(10^{-3}\right)T^2 - 6966\ T^{-1} - 22.044\ T\ \ln\ T \quad \text{J mol}^{-1} \tag{166}$$

(where T is in Kelvin). A similar expression is obtained for $\mu^{o(s)}_{Na}$. The Gibbs energies of $Cd_{11}Na_2$ and Cd_2Na have not been measured and are obtained from the optimization procedure.

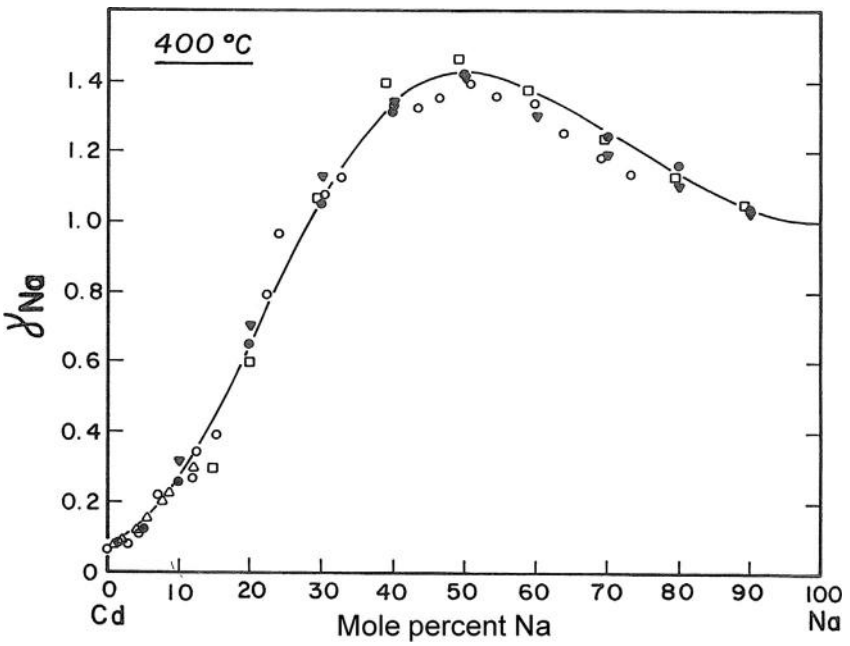

Figure 50 Sodium activity coefficient in liquid Cd–Na alloys at 400 °C. Line is calculated from optimized thermodynamic parameters. □ Hauffe (1940), ● Lantratov and Mikhailova (1971), △ Maiorova et al. (1976), ▼ Alabyshev and Morachevskii (1957), O Bartlett et al. (1970).

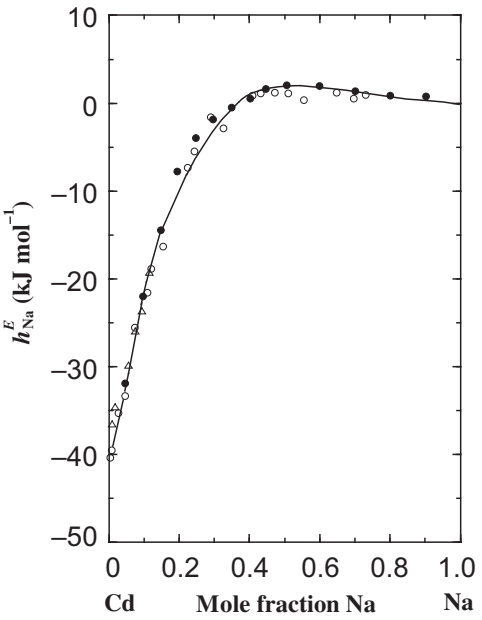

Figure 51 Partial excess enthalpy of sodium in liquid Cd–Na alloys. Line is calculated from optimized thermodynamic parameters. ● Lantratov and Mikhailova (1971), △ Maiorova et al. (1976), O Bartlett et al. (1970).

We now require an expression for the Gibbs energy of the liquid phase. From Eqns 88, 107 and 111,

$$g^{\mathrm{l}} = X_{\mathrm{Cd}}\mu_{\mathrm{Cd}}^{\mathrm{o(l)}} + X_{\mathrm{Na}}\mu_{\mathrm{Na}}^{\mathrm{o(l)}} + \mathrm{RT}(X_{\mathrm{Cd}}\ln\ X_{\mathrm{Cd}} + X_{\mathrm{Na}}\ln\ X_{\mathrm{Na}}) + \left(h^{\mathrm{E}} - Ts^{\mathrm{E}}\right) \tag{167}$$

Expressions similar to Eqn 166 can be obtained for $\mu_{\mathrm{Cd}}^{\mathrm{o(l)}}$ and $\mu_{\mathrm{Na}}^{\mathrm{o(l)}}$ from measurements of the melting points, enthalpies of fusion and heat capacities of the liquid phase of the pure elements. For many simple binary substitutional solutions, good representations of h^{E} and s^{E} are obtained by expanding the functions as polynomials in the mole fractions X_{A} and X_{B} of the components:

$$h^{\mathrm{E}} = X_{\mathrm{A}}X_{\mathrm{B}}\left[h_0 + h_{\mathrm{l}}(X_{\mathrm{B}} - X_{\mathrm{A}}) + h_2(X_{\mathrm{B}} - X_{\mathrm{A}})^2 + h_3(X_{\mathrm{B}} - X_{\mathrm{A}})^3 + \ldots\right] \tag{168}$$

$$s^{\mathrm{E}} = X_{\mathrm{A}}X_{\mathrm{B}}\left[s_0 + s_{\mathrm{l}}(X_{\mathrm{B}} - X_{\mathrm{A}}) + s_2(X_{\mathrm{B}} - X_{\mathrm{A}})^2 + s_3(X_{\mathrm{B}} - X_{\mathrm{A}})^3 + \ldots\right] \tag{169}$$

where the h_i and s_i are empirical parameters to be obtained during optimization. As many parameters are used as are required to represent the data in a given solution. For most solutions, it is a good approximation to assume that the coefficients h_i and s_i are independent of temperature.

If the series are truncated after the first term, then

$$g^{\mathrm{E}} = h^{\mathrm{E}} - Ts^{\mathrm{E}} = X_{\mathrm{A}}X_{\mathrm{B}}(h_0 - Ts_0) \tag{170}$$

This is the equation for a regular solution discussed in Section 3.5.5. Hence, the polynomial representation can be considered to be an extension of regular solution theory. When the expansions are written in terms of the composition variable $(X_{\mathrm{B}} - X_{\mathrm{A}})$, as in Eqns 168 and 169, they are said to be in *Redlich–Kister form.*

Differentiation of Eqns 168 and 169 and substitution into Eqns 116 and 114 yields the following expansions for the partial excess enthalpies and entropies:

$$h_{\mathrm{A}}^{\mathrm{E}} = X_{\mathrm{B}}^2 \sum_{i=0} h_{\mathrm{i}}\left[(X_{\mathrm{B}} - X_{\mathrm{A}})^i - 2i\,X_{\mathrm{A}}(X_{\mathrm{B}} - X_{\mathrm{A}})^{i-1}\right] \tag{171}$$

$$h_{\mathrm{B}}^{\mathrm{E}} = X_{\mathrm{A}}^2 \sum_{i=0} h_i\left[(X_{\mathrm{B}} - X_{\mathrm{A}})^i - 2i\,X_{\mathrm{B}}(X_{\mathrm{B}} - X_{\mathrm{A}})^{i-1}\right] \tag{172}$$

$$S_{\mathrm{A}}^{\mathrm{E}} = X_{\mathrm{B}}^2 \sum_{i=0} S_i\left[(X_{\mathrm{B}} - X_{\mathrm{A}})^i - 2i\,X_{\mathrm{A}}(X_{\mathrm{B}} - X_{\mathrm{A}})^{i-1}\right] \tag{173}$$

$$S_{\mathrm{B}}^{\mathrm{E}} = X_{\mathrm{A}}^2 \sum_{i=0} S_i\left[(X_{\mathrm{B}} - X_{\mathrm{A}})^i - 2i\,X_{\mathrm{B}}(X_{\mathrm{B}} - X_{\mathrm{A}})^{i-1}\right] \tag{174}$$

Equations 168, 169 and 171–174 are linear in terms of the coefficients. Through the use of these equations, all integral and partial excess properties (g^{E}, h^{E}, s^{E}, μ_i^E, h_i^E, s_i^E) can be expressed by linear equations in terms of the one set of coefficients $\{h_i, s\}$. It is thus possible to include all available experimental data for a binary phase in one simultaneous linear optimization.

Several algorithms have been developed to perform such optimizations using least-squares, Bayesian, and other techniques. See, for example, Bale and Pelton (1983), Lukas et al. (1977), Dörner et al. (1980) and Köningsberger and Eriksson (1995).

All the data points shown in **Figures 49–51** along with the enthalpy of mixing data for the liquid (Kleinstuber, 1961) were optimized in one simultaneous operation (Pelton, 1988) to obtain the following expressions for h^{E} and s^{E} of the liquid:

$$h^{E(l)} = X_{Cd}X_{Na}\left[-12\,508 + 20\,316(X_{Na} - X_{Cd}) - 8\,714(X_{Na} - X_{Cd})^2\right] \text{J mol}^{-1} \tag{175}$$

$$\begin{aligned} s^{E(l)} = X_{Cd}X_{Na}\Big[&-15.452 + 15.186(X_{Na} - X_{Cd}) - 10.062(X_{Na} - X_{Cd})^2 \\ &- 1.122(X_{Na} - X_{Cd})^3\Big] \text{J mol}^{-1}\ \text{K}^{-1} \end{aligned} \tag{176}$$

During the same simultaneous optimization procedure, the optimized Gibbs energies of fusion of the two compounds were determined:

$$\Delta g^{o}_{f(1/13Cd_{11}Na_2)} = 6\,816 - 10.724\ T \quad \text{J mol}^{-1} \tag{177}$$

$$\Delta g^{o}_{f(1/3Cd_2Na)} = 8\,368 - 12.737\ T \quad \text{J mol}^{-1} \tag{178}$$

The above equations can be combined to give the Gibbs energies of formation of the two compounds from the solid elements. (See **Figure 21** for an illustration of the relation between the Gibbs energy of formation and the Gibbs energy of fusion of a compound.)

Equation 175 reproduces the calorimetric data within 200 J mol^{-1}. Equations 114, 119, 172 and 174 can be used to calculate h^{E}_{Na} and γ_{Na}. The calculated curves are compared to the measured points in **Figures 50 and 51**. The optimized enthalpies of fusion of the compounds of 6816 and 8368 J mol^{-1} agree within error limits with the values of 6987 and 7878 J mol^{-1} measured by Roos (1916).

The phase diagram in **Figure 49** was calculated from the optimized thermodynamic expressions. Complete details of the analysis of the Cd–Na system are given by Pelton (1988).

It can thus be seen that one simple set of equations can simultaneously and self-consistently describe all the thermodynamic properties and the phase diagram of a binary system.

The exact optimization procedure will vary from system to system depending upon the type and accuracy of the available data, the number of phases present, the extent of solid solubility, etc. A large number of optimizations have been published since 1977 in the *Calphad Journal* (Pergamon).

3.8.2 Solution Models

As discussed in Section 3.8.1, the polynomial model, Eqns 168 and 169, is an extension of regular solution theory (Section 3.5.5). Hence, the polynomial model can be expected to provide an acceptable description of the properties of a solution only if the physical assumptions of regular solution theory are approximately valid, that is, if the solution is approximately a random substitutional solution of atoms or molecules on a single sublattice with relatively weak interactions.

3.8.2.1 Short-Range-Ordering (sro) and the Quasichemical Model

Consider a binary solution of components A–B with a single sublattice (or quasilattice in the case of a liquid) and consider the formation of two nearest-neighbor A–B pairs from an A–A and a B–B pair by the following "quasichemical reaction":

$$(\mathrm{A}-\mathrm{A})_{\mathrm{pair}} + (\mathrm{B}-\mathrm{B})_{\mathrm{pair}} = 2(\mathrm{A}-\mathrm{B})_{\mathrm{pair}} \tag{179}$$

Let the molar Gibbs energy change for this reaction be $(\omega - \eta T)$. This term has essentially the same interpretation in terms of bond energies as the regular solution parameter as in Eqns 136–138.

If $(\omega - \eta T)$ is negative, then reaction in Eqn 179 is displaced to the right, and at equilibrium, the fraction of (A−B) pairs will be greater than in an ideal randomly mixed solution. Conversely, if $(\omega - \eta T)$ is positive, reaction in Eqn 179 is shifted to the left and clustering of A and B particles occurs; if it is sufficiently positive, a miscibility gap will be observed. This sro can be modeled by the quasichemical model in the pair approximation (Guggenheim, 1935; Fowler and Guggenheim, 1939), which has been modified by Pelton and Blander (1984) and Blander and Pelton (1987). For the most recent and complete development of the modified quasichemical model (MQM) in the pair approximation, see Pelton et al. (2000) and Pelton and Chartrand (2001a).

In the MQM, expressions for the enthalpy and entropy of a solution are written in terms of the numbers of (A−A), (B−B) and (A−B) pairs. The expression for the entropy is obtained via the Helmholtz Equation 2 by randomly distributing the pairs over pairs of lattice sites rather than by distributing the atoms or molecules over lattice sites as in the regular solution theory. The parameter of the model, $(\omega - \eta T)$, can be expanded as an empirical polynomial in the component mole fractions similar to Eqns 168 and 169 or as a polynomial in the pair fractions. The numbers of each type of pair at equilibrium are then obtained by minimizing the Gibbs energy. This results in an equilibrium constant for the quasichemical reaction in Eqn 179. In the limit as $(\omega - \eta T)$ approaches zero, the MQM and the polynomial model become identical (Pelton et al, 2000). When $(\omega - \eta T)$ differs significantly from zero, the shapes of the curves of h^{E} and s^{E} versus composition predicted by the MQM differ significantly from the approximately parabolic shape (Eqn 133) predicted by the polynomial model, and generally correspond more closely to experimental data. The MQM has been used successfully (see FactSage) to model a large number of solutions, particularly liquid solutions, of metals, salts, sulfides and oxides.

Quasichemical theory has been further extended beyond the pair approximation to account for clusters of more than two particles. This model is known as the Cluster Variation Method (CVM). For a review of the CVM, see Inden (2001). A somewhat simplified version of the CVM, which is mathematically more tractable, is the Cluster Site Approximation (CSA) proposed by Oates and Wenzl (1996); see also Inden (2001).

3.8.2.2 Long-Range-Ordering (lro) and Sublattice Models

lro is generally treated by models which involve two or more sublattices. Ionic salts, for example, are modeled with one sublattice for cations and another for anions. As another example, in the spinal structure of certain ceramic oxides, the oxygen ions occupy one sublattice while some metal ions are distributed on a second sublattice with tetrahedral coordination and other metal ions are distributed on a third sublattice with octahedral coordination. Intermetallic solutions, such as Laves phases, are described by sublattice models. Interstitial solutions are modeled by introducing an interstitial sublattice on which some sites are occupied while others are vacant. Nonstoichiometric compounds $\mathrm{A}_x\mathrm{B}_y$ with a range of homogeneity, as, for example, the compounds β′ and ε in

Figure 22, are modeled as containing point defects such as substitutional defects (some A atoms on B-sublattice sites and B atoms on A-sublattice sites), interstitial atoms, or vacancies on one or more sublattices.

The simplest implementation of sublattice modeling is the Compound Energy Formalism (CEF) (Barry et al., 1992; Hillert, 2008), in which species are distributed randomly over each sublattice. The parameters of the model are, essentially, the site energies for the species on the different sublattices and the interaction energies between pairs of species on different sublattices and on the same sublattice. The equilibrium distribution of species among the sublattices is calculated as that which minimizes the Gibbs energy of the solution. The CEF has been applied successfully to model a very large number of solutions of metals, salts, oxides, sulfides, etc.

The CEF model accounts for lro, but not for sro. In some solutions, a satisfactory representation of the properties can only be obtained by modeling both lro and sro simultaneously. The CVM and CSA models permit this as does an extension of the MQM to systems with two sublattices (Pelton and Chartrand, 2001b). An approximate correction term for relatively small degrees of sro can also be added to the CEF equations (Hillert, 2008).

3.8.3 Estimating Thermodynamic Properties of Ternary and Multicomponent Solutions

Among 70 metallic elements, $70!/3!67! = 54\,740$ ternary systems and 916 895 quaternary systems are formed. In view of the amount of work involved in measuring even one isothermal section of a relatively simple ternary phase diagram, it is very important to have a means of estimating ternary and higher order phase diagrams.

For a solution phase in a ternary system with components A–B–C, one first performs evaluations/optimizations on the three binary subsystems A–B, B–C and C–A as discussed in Section 3.8.1 in order to obtain the binary model parameters. Next, the model is used, along with reasonable assumptions, to estimate the thermodynamic properties of the ternary solution.

Suppose that a phase, such as a liquid phase or an fcc phase, has been modeled in all three binary subsystems with the simple polynomial model of Eqns 168 and 169. The Gibbs energy of the ternary solution could then be estimated by the following equation first suggested by Kohler (1960):

$$g^{\mathrm{E}} = (1 - X_{\mathrm{A}})^2 g^{\mathrm{E}}_{\mathrm{B/C}} + (1 - X_{\mathrm{B}})^2 g^{\mathrm{E}}_{\mathrm{C/A}} + (1 - X_{\mathrm{C}})^2 g^{\mathrm{E}}_{\mathrm{A/B}} \tag{180}$$

In this equation, g^{E} is the excess molar Gibbs energy at a composition point in the ternary liquid phase and $g^{\mathrm{E}}_{\mathrm{B/C}}, g^{\mathrm{E}}_{\mathrm{C/A}}$ and $g^{\mathrm{E}}_{\mathrm{A/B}}$ are the excess Gibbs energies in the three binary systems at the same ratios $X_{\mathrm{B}}/X_{\mathrm{C}}$, $X_{\mathrm{C}}/X_{\mathrm{A}}$ and $X_{\mathrm{A}}/X_{\mathrm{B}}$ as at the ternary point. If the ternary liquid phase as well as the three binary liquid phases are all regular solutions, then Eqn 180 is exact. In the general case, a physical interpretation of Eqn 180 is that the contribution to g^{E} from pair interactions between A and B species is constant at a constant ratio $X_{\mathrm{A}}/X_{\mathrm{B}}$, apart from the dilutive effect of the C species which is accounted for by the term $(1 - X_{\mathrm{C}})^2$ taken from regular solution theory.

Ternary phase diagrams estimated in this way are often quite acceptable. The agreement between the experimental and calculated diagrams can be markedly improved by the inclusion of one or more "ternary terms" with adjustable parameters in the interpolation equations for g^{E}. For example, ternary terms $a_{ijk} X_{\mathrm{A}}^i X_{\mathrm{B}}^j X_{\mathrm{C}}^k$ $(i \geq 1, j \geq 1, k \geq 1)$, which are zero in all three binary subsystems, could be added to Eqn 180 and the values of the parameters a_{ijk}, which gives the "best" fit to experimental ternary thermodynamic or phase equilibrium data could be found by optimization. This, of course, requires that ternary measurements be made, but only a few experimental points will generally suffice rather

than the large number of measurements usually required for a fully experimental determination. In this way, the coupling of the thermodynamic approach with a few well-chosen experimental measurements greatly reduces the experimental effort involved in determining multicomponent phase diagrams.

Other equations, similar to the Kohler Equation 180 are often used to estimate the thermodynamic properties of ternary solutions from the model parameters of the binary subsystems when the polynomial model is used. For a discussion, and for extensions to estimating the thermodynamic properties of multicomponent solutions from binary and ternary model parameters, see Pelton (2001b). These equations, like the Kohler equation, are based on the polynomial model, which is an extension of regular solution theory, and they can only be expected to yield good estimates when the physical assumptions of the model are valid; that is, when the solution can reasonably be approximated as a random substitutional solution on a single sublattice with relatively weak interactions. For more complex solutions, involving sro or lro, a good estimate can only be expected when a proper physical model is employed. Therefore, if the solution in question is a liquid with appreciable sro, a model which takes sro into account must be used for the multicomponent solution, including all three binary subsystems, even though it might be possible to force fit a binary solution with a simpler model such as the polynomial model. If the solution exhibits lro, then an appropriate sublattice model must be used. As an example of the prediction of ternary phase diagrams from optimized model parameters for the binary subsystems, the liquid phase of the Zn–Mg–Al system was modeled using the MQM, and binary model parameters were obtained by evaluation/optimization of the three binary subsystems (see FactSage). The thermodynamic properties of the ternary liquid phase were then estimated with the MQM by assuming that the binary parameters remain constant in the ternary solution along lines of constant X_{Zn}/X_{Mg}, X_{Mg}/X_{Al} and X_{Al}/X_{Zn}. When the ternary liquidus projection was then calculated, based only on the binary parameters, a liquidus surface was calculated, which deviates from that shown in **Figure 27** by no more than 8° and 2 mol%. Since experimental data are available for this system, they were used to evaluate one small ternary model parameter. The resultant calculated diagram in **Figure 27** agrees with the available experimental data within the experimental error limits.

Such agreement is not exceptional. Phase diagrams calculated from the best thermodynamic databases generally agree with experimental measurements within or nearly within experimental error limits. In this regard, it may be noted that estimating the properties of a C-component system from the optimized parameters of its $(C - 1)$-component subsystems becomes increasingly more exact as C becomes larger. For example, if all the ternary subsystems of a four-component system have been experimentally investigated and optimized ternary model parameters have been obtained, then the estimation of the properties of the four-component solution are generally good.

For a general discussion of many solution models, see Hillert (2008). A great many models and their applications have been published since 1977 in the *Calphad Journal* (Pergamon).

3.9 Equilibrium and Nonequilibrium Solidification

3.9.1 Equilibrium Solidification

The course of equilibrium solidification can be followed through the use of isoplethal sections, such as that for the six-component Mg alloy shown in **Figure 48**. Polythermal liquidus projections are also useful in this respect. Consider an alloy with composition 80 mol% Mg, 15% Al and 5% Zn at point B in **Figure 27**. As this alloy is cooled at equilibrium, solid-hcp Mg begins to precipitate at the liquidus

temperature, which is just below 500 °C. The liquid composition then follows the crystallization path shown in **Figure 27** until it attains a composition on the univariant line. The liquid composition then follows the univariant line toward the point P' with coprecipitation of hcp and the gamma phase. (For a discussion of equilibrium crystallization paths, see Section 3.6.3.) At point P', a quasiperitectic reaction occurs. All the foregoing information can be deduced from **Figure 27**. However, from this diagram alone, it is not possible to determine the amounts and compositions of the various phases at equilibrium because the extent of the solid solutions are not shown nor, for the same reason, is it possible to determine whether solidification is complete at the point P' or whether the liquid persists to lower temperatures.

However, with thermodynamic calculations, this information is readily obtained. Software is available, with tabular or graphical display, to calculate the amounts and compositions of every phase during equilibrium solidification as well as to display the sequence of reactions during solidification. In the current example, the reaction sequence, calculated using the FactSage software and databases, is

$$\text{Liq.} \rightarrow \text{hcp}\,(498^\circ - 405\,^\circ\text{C};\ \text{bivariant})$$

$$\text{Liq.} \rightarrow \text{hcp} + \gamma\,(405^\circ - 364\,^\circ\text{C};\ \text{univariant})$$

$$\gamma + \text{Liq.} \rightarrow \phi + \text{hcp}(364\,^\circ\text{C};\ \text{invariant})$$

The solidification is calculated to terminate at 364 °C with complete consumption of the liquid by the quasiperitectic reaction. A graphical display of the calculated amounts of all phases during equilibrium cooling is shown in **Figure 52**.

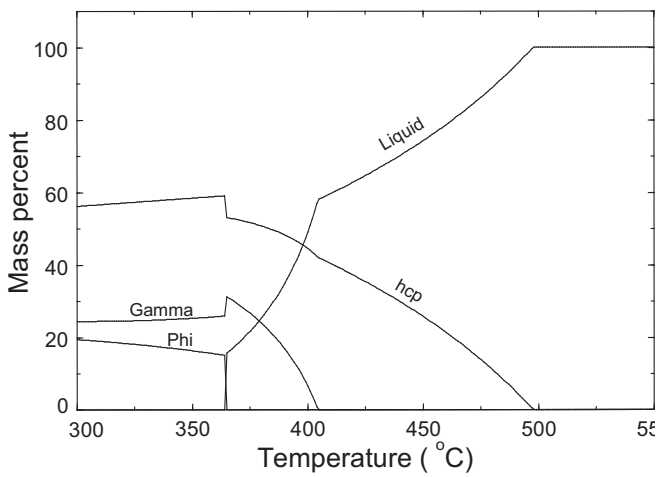

Figure 52 Calculated amounts of phases present during equilibrium cooling of an alloy of composition 85 mol% Mg, 15% Al, 5% Zn (point B in **Figure 27**) (see FactSage).

3.9.2 Nonequilibrium Scheil–Gulliver Solidification

Throughout equilibrium cooling, every solid-solution phase remains homogeneous with no concentration gradients. As was described in Section 3.3.1, during the equilibrium cooling of a Bi–Sb alloy (**Figure 11**) with $X_{Sb} = 0.6$, the first solid precipitate appears at 526 °C with a composition $X_{Sb} = 0.89$. As cooling continues, the composition of the solid phase follows the solidus to point D, at which its composition is $X_{Sb} = 0.60$, and solidification terminates at 349 °C. For all this to happen, diffusion must continually occur in the solid grains in order for their composition to remain uniform. Since solid-state diffusion is a relatively slow process, equilibrium cooling conditions are realized only for very slow cooling rates.

Consider now the limiting case of extremely rapid cooling such that no diffusion whatsoever takes place in the solid phase. However, the liquid is still assumed to be homogeneous, and equilibrium is assumed at the solid/liquid interface. Consequently, there will be a concentration gradient within the grains, with the concentration of Sb decreasing from a maximum of $X_{Sb} = 0.89$ at the points of initial nucleation. When the temperature has decreased to 349 °C, the concentration of Sb at the surface of the solid grains will be $X_{Sb} = 0.60$, but the average composition of the solid will lie between $X_{Sb} = 0.60$ and $X_{Sb} = 0.89$. Hence, a liquid phase is still present at 349 °C and will, in fact, persist down to the melting point of pure Bi, 271.4 °C.

This limiting case is called *Scheil–Gulliver cooling*. As another example, consider the cooling of the hypothetical ternary liquid with composition at point b in **Figure 26**. As discussed in Section 3.6.3, under equilibrium cooling conditions, solidification terminates at point P, where the liquid is completely consumed in the ternary peritectic reaction: Liquid + ε + β → ζ. During Scheil–Gulliver cooling, on the other hand, peritectic reactions (or any reactions involving solid reactants) cannot occur. Hence, the liquid continues to lower temperatures, its composition following the univariant lines past point P_3' to the ternary eutectic composition E_3, where it is finally consumed in the ternary eutectic reaction. (The liquid does not follow the other path from P to P_1' because tie-triangles $\varepsilon\zeta X$, where X is any point on the line PP_1', do not contain the liquid composition at point P. That is, ε and ζ cannot coprecipitate from a liquid of composition P because of mass-balance considerations.)

Similarly, for the Zn–Mg–Al system, it was shown in Section 3.9.1 that a liquid of initial composition at point B in **Figure 27**, when cooled under equilibrium conditions, is completely consumed by the quasiperitectic reaction at point P′. Under Scheil–Gulliver cooling conditions, on the other hand, the liquid will continue to lower temperatures, following the univariant lines to the eutectic point E. Furthermore, the path followed by the composition of the liquid along the liquidus during precipitation of the primary hcp phase (shown by the small arrows in **Figure 27**) will be different in the cases of equilibrium and Scheil–Gulliver cooling, as will the compositions and relative amounts of the phases at any temperature. The course of Scheil–Gulliver cooling is easily followed through thermodynamic calculations using the following algorithm. The temperature is reduced from the initial liquid state in incremental steps, typically of the order of 1°–10°. At each step, the equilibrium state is calculated and then all solid phases are removed from the calculation, leaving only the liquid, which is then cooled by another incremental step and the process is repeated. At any temperature, the amount and average composition of every phase can thereby be calculated and presented in tabular or graphical form similar to **Figure 52**. The calculated (FactSage) reaction sequence in the present example is

$$\text{Liq.} \rightarrow \text{hcp}\,(498^\circ - 405\,^\circ\text{C};\ \text{bivariant})$$

$$\text{Liq.} \rightarrow \text{hcp} + \gamma\,(405\,^\circ - 364\,^\circ\text{C};\ \text{univariant})$$

$$\text{Liq.} \rightarrow \text{hcp} + \text{Phi}\,(364\,^{\circ} - 343\,^{\circ}\text{C};\ \text{univariant})$$

$$\text{Liq.} \rightarrow \text{hcp} + \text{Tau}\,(343\,^{\circ} - 341\,^{\circ}\text{C};\ \text{univariant})$$

$$\text{Liq.} \rightarrow \text{hcp} + \text{Tau} + \text{MgZn}\,(341\,^{\circ}\text{C};\ \text{invariant})$$

This reaction sequence may be compared to that given in Section 3.9.1 for equilibrium cooling of the same alloy.

3.9.3 General Nomenclature for Invariant and Other Reactions

As discussed in Section 3.5.9, in a binary isobaric temperature-composition phase diagram, there are two possible types of invariant reactions: "eutectic-type" ($\beta \rightarrow \alpha + \gamma$) and "peritectic type" ($\alpha + \gamma \rightarrow \beta$). In a ternary system, there are "eutectic-type" ($\alpha \rightarrow \beta + \gamma + \delta$), "peritectic-type" ($\alpha + \beta + \gamma \rightarrow \delta$), and "quasi-peritectic-type" ($\alpha + \beta \rightarrow \gamma + \delta$) invariants (Section 3.6.3). In a system of C components, the number of types of isobaric invariant reactions is equal to C. A reaction with one reactant, such as ($\alpha \rightarrow \beta + \gamma + \delta$) is clearly a "eutectic-type" invariant reaction but, in general, there is no standard terminology. These reactions may be conveniently described according to the numbers of reactants and products (in the direction which occurs upon cooling). Hence, the reaction ($\alpha + \beta \rightarrow \gamma + \delta + \varepsilon$) is a *2 → 3 reaction*; the reaction ($\alpha \rightarrow \beta + \gamma + \delta$) is a *1 → 3 reaction*; and so on.

A similar terminology can be used for univariant, bivariant, etc. isobaric reactions. For example, a *1 → 2* reaction ($\alpha \rightarrow \beta + \gamma$) is invariant in a binary system, but univariant in a ternary system. The ternary peritectic-type *3 → 1 reaction* ($\alpha + \beta + \gamma \rightarrow \delta$) is invariant in a ternary system, univariant in a quaternary system, bivariant in a quinary system, etc.

3.9.4 Quasi-Invariant Reactions

According to the Phase Rule, an invariant reaction occurs in a C-component system when $(C + 1)$ phases are at equilibrium at constant pressure. Apparent exceptions are observed where an isothermal reaction occurs even though fewer than $(C + 1)$ phases are present. However, these are just limiting cases.

An example was shown in **Figure 17**. A liquid with a composition exactly at the liquidus/solidus minimum in a binary system will solidify isothermally to give a single solid phase of the same composition. Similarly, at a maximum in a two-phase region in a binary system, the liquid solidifies isothermally to give a single solid phase, as, for example, at the congruent melting points of the β' phase in **Figure 22** and of the Ca_2SiO_4 and $CaSiO_3$ compounds in **Figure 21**. Such maxima are also associated with congruently melting compounds in ternary and higher order systems as, for example, the compound η in **Figure 26**.

In a ternary system, a minimum point may be observed on a univariant line as shown in **Figure 53**. In this hypothetical system, there are two solid phases, pure stoichiometric A and a solid solution of B and C, in which A is only slightly soluble. The A–B and C–A binary subsystems, thus, have simple eutectic phase diagrams, while the B–C system resembles **Figure 11**. A liquid with a composition at the minimum point m on the univariant line joining the two binary eutectic points e_1 and e_2 will solidify isothermally to give solid A (α) and a solid solution (β) of composition at point p. Point m is a local liquidus minimum, but the isothermal solidification at point m is not a ternary eutectic reaction since the latter involves three solid phases. Similar quasi-invariant reactions can also occur at liquidus minima in higher order systems.

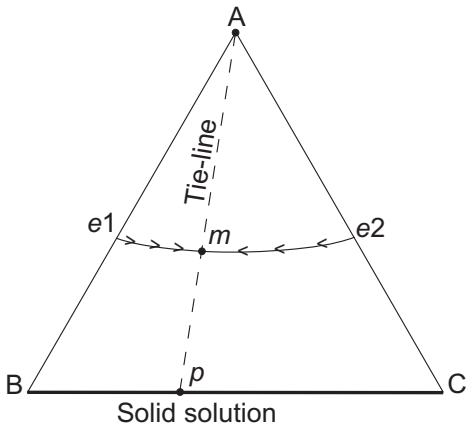

Figure 53 Liquidus projection of a system A–B–C with a minimum on the univariant line joining the binary eutectic points e_1 and e_2. Solid phases are stoichiometric A (α) and a binary solid solution B–C (β).

At point m in **Figure 53**, the eutectic quasi-invariant reaction Liq $\rightarrow \alpha + \beta$ occurs isothermally. A line joining two binary peritectic points p_1 and p_2 in a ternary system can also pass through a minimum at which an isothermal peritectic quasi-invariant reaction occurs: Liq $+ \alpha \rightarrow \beta$.

Another example of a quasi-invariant reaction is that which occurs at saddle points such as the point s in **Figures 26 and 27**. Saddle points occur at maxima on univariant lines. A ternary liquid with a composition exactly at a saddle point will solidify isothermally, at constant composition, to give the two solid phases with which it is in equilibrium. Higher order saddle points can be found in systems where $C \geq 4$.

3.10 Second-Order and Higher-Order Transitions

All the transitions discussed until now have been *first-order transitions*. When a first-order phase boundary is crossed, a new phase appears with extensive properties which are discontinuous with the other phases.

An example of a transition that is not first order is the ferromagnetic-to-paramagnetic transition of Fe, Co, Ni and other ferromagnetic materials that contain unpaired electron spins. Below its Curie temperature, $T_{\text{curie}} = 1043$ K, Fe is ferromagnetic since its spins tend to be aligned parallel to one another. This alignment occurs because it lowers the internal energy of the system. At 0 K at equilibrium, the spins are fully aligned. As the temperature increases, the spins become progressively less aligned since this disordering increases the entropy of the system, until at T_{curie}, the disordering is complete and the material becomes paramagnetic. There is never a two-phase region and no abrupt change occurs at T_{curie}, which is simply the temperature at which the disordering becomes complete.

The following model is vastly oversimplified and is presented only as the simplest possible model illustrating the essential features of a second-order phase transition.

Suppose that we may speak of localized spins and, furthermore, that a spin is oriented either "up" or "down." Let the fraction of "up" and "down" spins be ξ and $(1 - \xi)$. Suppose further that when two neighboring spins are aligned, a stabilizing internal energy contribution $\varepsilon < 0$ results. Assuming that the

spins are randomly distributed, the probability of two "up" spins being aligned is ξ^2 and of two "down" spins being aligned is $(1-\xi)^2$. The resultant contribution to the molar Gibbs energy is

$$g = RT(\xi \ln \xi + (1-\xi)\ln(1-\xi)) + \left[\xi^2 + (1-\xi)^2\right]\varepsilon \tag{181}$$

The equilibrium value of ξ is that which minimizes g. Setting $\mathrm{d}g/\mathrm{d}\xi = 0$ gives

$$\xi/(1-\xi) = \exp(2(1-2\xi)\varepsilon/RT) \tag{182}$$

At $T = 0$ K, $\xi = 0$ (or, equivalently, $\xi = 1$). That is, the spins are completely aligned. A plot of ξ versus T from Eqn 182 shows that ξ increases with T, attaining the value $\xi = 1/2$, when $T = -\varepsilon/R$. At all higher temperatures, $\xi = 1/2$ is the only solution of Eqn 182 above $T_{\text{curie}} = -\varepsilon/R$. As the spins become progressively more disordered with increasing temperature below T_{curie}, energy is absorbed, thereby increasing the heat capacity. Most of the disordering occurs over a fairly small range of temperature just below T_{curie}. This can be seen in **Figure 8** where the slope of the enthalpy curve increases just below T_{curie} and then quite abruptly decreases again above this temperature.

In this extremely simple model, there is a discontinuity in the slope $c_P = \mathrm{d}h/\mathrm{d}T$ at T_{curie}, that is, a discontinuity in the second derivative of the Gibbs energy. Such a transition is called a *second-order transition*.

For proper models of magnetism, see Chapter 19, Volume II. In reality, some ordering persists above T_{curie}, and the transformation is not exactly second order. Transitions involving discontinuities in the third, fourth, etc. derivatives of G are called third-order, fourth-order, etc. transitions.

The T-composition phase diagram of the Fe–Ni system is shown in **Figure 54**. The Curie temperature varies with composition as it traverses the bcc phase field as a line. Nickel also undergoes a magnetic

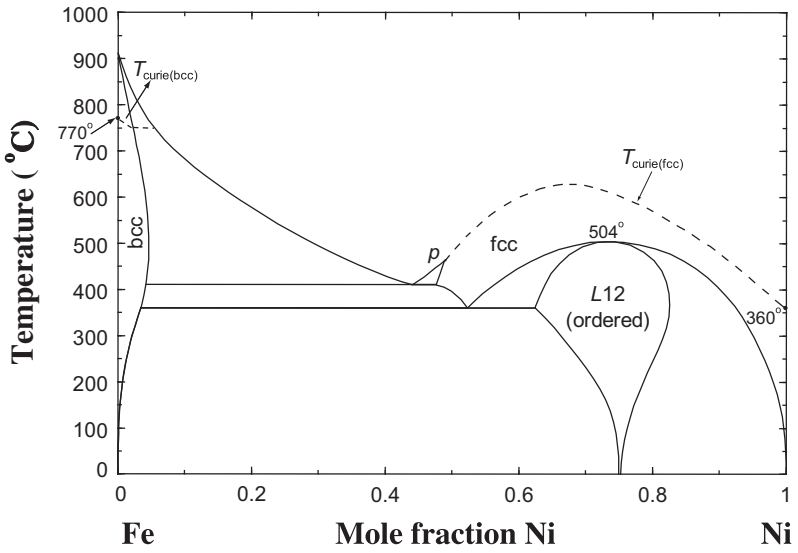

Figure 54 Temperature-composition phase diagram of the Fe–Ni system at $P = 1$ bar showing the magnetic transformations (see FactSage; SGTE; Massalski et al., 2001).

transition at its Curie temperature of 360 °C. The second-order transition line crosses the fcc phase field as shown.

At point *P* in **Figure 54**, the second-order transition line widens into a two-phase miscibility gap and the magnetic transition becomes first order. Point P is called a *tri-critical point*. (Other versions of the Fe–Ni phase diagram do not show a tri-critical point (Massalski et al., 2001).)

The magnetic transition is an example of an *order–disorder transition*. Another important type of order–disorder transition involves an ordering of the crystal structure. An example is seen in the Al–Fe system in **Figure 55**. At low temperatures, the body-centered phase exhibits lro. Two sublattices can be distinguished, one consisting of the corner sites of the unit cells and the other of the body-centered sites. The Al atoms preferentially occupy one sublattice while the Fe atoms preferentially occupy the other. This is the ordered B2 (CsCl) structure. As the temperature increases, the phase becomes progressively disordered, with more and more Al atoms moving to the Fe-sublattice and *vice versa* until, at the transition line, the disordering becomes complete with the Al and Fe atoms distributed equally over both sublattices. At this point, the two sublattices become indistinguishable, the lro disappears, and the structure becomes the A2 (bcc) structure. As with the magnetic transition, there is no two-phase region and no abrupt change at the transition line, which is simply the temperature at which the disordering becomes complete. As with the magnetic transition, most of the disordering takes place over a fairly small range of temperature just below the transition line. The heat capacity, thus, increases as the transition line is approached from below and then decreases sharply as the line is crossed. The transition is thus second order, or approximately second order.

The B2/A2 transition line may terminate at a tri-critical point like point P of **Figure 54**. Although it is not shown in **Figure 55**, there is most likely a tri-critical point near 660 °C.

Order–disorder transitions need not necessarily be of second- or higher order. In **Figure 54**, the L12 phase has an ordered face-centered structure with the Ni atoms preferentially occupying the

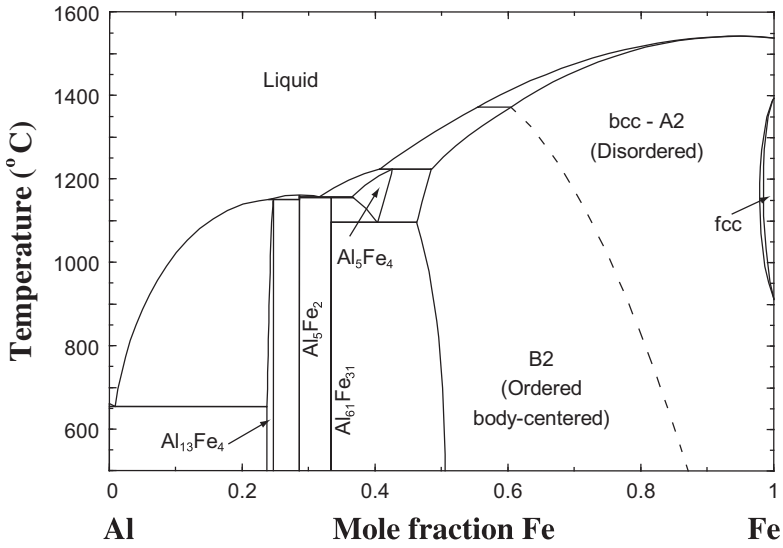

Figure 55 Temperature-composition phase diagram of the Al–Fe system at $P = 1$ bar showing the B2 → A2 order–disorder transition (see FactSage; SGTE).

face-centered sites of the unit cells and the Fe atoms in the corner sites. This structure transforms to the disordered fcc (A1) structure by a first-order transition with a discontinuous increase in enthalpy at the congruent point (504 °C). There is some controversy as to whether or not many reported second-order transition lines may actually be very narrow two-phase regions.

Although there is no lro in the high-temperature disordered structures, appreciable sro remains. For example, in the disordered A2 phase in the Al–Fe system, nearest neighbor (Fe–Al) pairs are still preferred as in the reaction in Eqn 179. Modeling of ordered phases and the order–disorder transition is a complex subject with a large literature. The CEF (Section 3.8.2.2) has been used with some success, but only through the introduction of a large number of adjustable parameters. A quantitative model most likely requires that the coupling of sro and lro be taken into account; the CVM and CSA models (Section 3.8.2.2) have been applied to this end. Ordered phases and order–disorder transitions are treated in Chapter 8 of this volume. See also Inden (2001).

3.11 Bibliography

3.11.1 Phase Diagram Compilations

From 1979 to the early 1990s, the American Society for Metals undertook a project to evaluate critically all binary and ternary alloy phase diagrams. All available literature on phase equilibria, crystal structures and, often, thermodynamic properties were critically evaluated in detail by international experts. Many evaluations have appeared in the *Journal of Phase Equilibria* (formerly *Bulletin of Alloy Phase Diagrams)*, (ASM Intl., Materials Park, OH), which continues to publish phase diagram evaluations. Condensed critical evaluations of 4700 binary alloy phase diagrams have been published in three volumes (Massalski et al., 2001). The ternary phase diagrams of 7380 alloy systems have also been published in a 10-volume compilation (Villars et al., 1995). Both binary and ternary phase diagrams from these compilations are available on the website of the ASM alloy phase diagram center. Many of the evaluations have also been published by ASM as monographs on phase diagrams involving a particular metal as a component.

The SGTE (Scientific Group Thermodata Europe) group has produced several subvolumes within volume 19 of the Landolt–Börnstein series (SGTE, 1999–2009) of compilations of thermodynamic data for inorganic materials and of phase diagrams and integral and partial thermodynamic quantities of binary alloys.

Phase diagrams for over 9000 binary, ternary and multicomponent ceramic systems (including oxides, halides, carbonates, sulfates, etc.) have been compiled in the 14-volume series, *Phase Diagrams for Ceramists* (Levin et al, 1964–2005). Earlier volumes were noncritical compilations. However, more recent volumes included critical commentaries. See also the Am. Ceram. Soc./NIST website for the online version.

Hundreds of critically evaluated and optimized phase diagrams of metallic, oxide, salt and sulfide systems may be downloaded from the FactSage website.

3.11.2 Further Reading

A recent text by Hillert (2008) provides a thorough thermodynamic treatment of phase equilibria as well as solution modeling and thermodynamic/phase diagram optimization.

A classical discussion of phase diagrams in metallurgy was given by Rhines (1956). Prince (1966) presents a detailed treatment of the geometry of multicomponent phase diagrams. A series of five

volumes edited by Alper (1970–1978) discusses many aspects of phase diagrams in materials science. Bergeron and Risbud (1984) give an introduction to phase diagrams, with particular attention to applications in ceramic systems.

In the *Calphad Journal*, (Pergamon) and in the *Journal of Phase Equilibria*, (ASM Intl., Materials Park, OH) are to be found many articles on the relationships between thermodynamics and phase diagrams.

The SGTE Casebook (Hack, 2008) illustrates, through many examples, how thermodynamic calculations can be used as a basic tool in the development and optimization of materials and processes of many different types.

Acknowledgments

It would have been impossible to write this chapter without the FactSage software. I am indebted to my colleagues Chris Bale, Gunnar Eriksson and Patrice Chatrand. Financial assistance over many years from the Natural Sciences and Engineering Research Council of Canada is gratefully acknowledged.

References

Alabyshev, A.F., Morachevskii, A.G., 1957. Z. Neorg. Khim. 2, 669.
Alper, A.M. (Ed.), 1970-1978. Phase Diagrams –J. Materials Science and Technology, vols. 1–5. Academic, New York.
Bale, C.W., Pelton, A.D., 1983. Metall. Trans. B 14, 77.
Bale, C.W., Pelton, A.D., Thompson, W.T., 1986. Canad. Metall. Quart. 25, 107.
Barry, T.I., Dinsdale, A.T., Gisby, J.A., Hallstedt, B., Hillert, M., Jansson, B., Jonsson, J., Sundman, B., Taylor, J.R., 1992. J. Phase Equilib. 13, 459.
Bartlett, H.E., Neethling, A.J., Crowther, P., 1970. J. Chem. Thermo. 2, 523.
Bergeron, C.J., Risbud, S.H., 1984. Introduction to Phase Equilibria in Ceramics. Columbus. Amer. Ceramic Soc, Ohio.
Blander, M., Pelton, A.D., 1987. Geochim. Cosmochim. Acta 51, 85.
Bray, H.F., Bell, F.D., Harris, S.J., 1961-1962. J. Inst. Metals 90, 24.
Dinsdale, A.T., 1991. Calphad J. 15, 317.
Dörner, P., Henig, E.-Th., Krieg, H., Lucas, H.L., Petzow, G., 1980. Calphad J. 4, 241.
Fowler, R.H., Guggenheim, E.A., 1939. Statistical Thermodynamics. Cambridge Univ. Press, Cambridge. p. 350.
Guggenheim, E.A., 1935. Proc. Roy. Soc. A148, 304.
Gupta, H., Morral, J.E., Nowotny, H., 1986. Scripta Metall. 20, 889.
Hack, K. (Ed.), 2008. SGTE Casebook-thermodynamics at Work, second ed. CRC Press, Boca Raton FL.
Hansen, M., 1958. Constitution of Binary Alloys, second ed. McGraw-Hill, New York.
Hauffe, K., 1940. Z. Elektrochem. 46, 348.
Hillert, M., 1997. J. Phase Equilib. 18, 249.
Hillert, M., 2008. Phase Equilibria, Phase Diagrams and Phase Transformations–their Thermodynamic Basis, second ed. Cambridge Univ. Press, Cambridge.
Hultgren, R., Desai, P.D., Hawkins, D.T., Gleiser, M., Kelly, K.K., Wagman, D.D., 1973. Selected Values of the Thermodynamic Properties of the Elements and Binary Alloys. Am. Soc. Metals, Metals Park, Ohio.
Inden, G., 2001. Atomic ordering. ch. 8. In: Kostorz, G. (Ed.), Phase Transformations in Materials. Wiley-VCH, Weinheim.
Kleinstuber, T., 1961. Ph.D. Thesis, Univ. Munich, Germany.
Kohler, F., 1960. Monatsh. Chem. 91, 738.
Königsberger, E., Eriksson, G., 1995. A new optimization routine for ChemSage. CALPHAD J. 19, 207–214.
Kurnakow, N.S., Kusnetzow, A.N., 1907. Z. Anorg. Chem. 52, 173.
Lantratov, M.R., Mikhailova, A.G., 1971. Zh. Prikl. Khimii 44, 1778.
Levin, E.M., Robbins, C.R., McMurdie, H.F., 1964-2005. Phase Diagrams for Ceramists. Am. Ceramic Soc., Columbus, Ohio.
Lukas, H.L., Henig, E.-Th., Zimmermann, B., 1977. Calphad J. 1, 225.
Maiorova, E.A., Morachevskii, A.G., Kovalenko, S.G., 1976. Elektrokhimiya 12, 313.
Massalski, T.B., Okamoto, H., Subramanian, P.R., Kacprzak, L., 2001. Binary Alloy Phase Diagrams, second ed. Am. Soc. Metals, Metals Park, OH.

Mathewson, C.H., 1906. Z. Ang. Chem. 50, 180.
Muan, A., Osborn, F., 1965. Phase Equilibria Among Oxides in Steeimaking. Addison Wesley, Reading, MA.
Oates, W.A., Wenzl, H., 1996. Scripta Master. 35, 623.
Palatnik, L.S., Landau, A.I., 1956. Zh. Fiz. Khim. 30, 2399.
Pelton, A.D., 1988. Bull. Alloy Phase Diag. 9, 41.
Pelton, A.D., 1995. J. Phase Equilib. 16, 501.
Pelton, A.D., 2001a. Thermodynamics and phase diagrams of materials. ch. 1. In: Kostorz, G. (Ed.), Phase Transformations in Materials. Wiley-VCH, Weinheim.
Pelton, A.D., 2001b. A general geometric thermodynamic model for multicomponent solutions. Calphad J. 25, 319–328.
Pelton, A. D., Blander, M. 1984. Proc. AIME Symp. Molten Salts Slags. Warrendale, Pa.: The Metall. Soc.AIME, p. 281.
Pelton, A.D., Chartrand, P., 2001a. The modified quasichemical model II – multicomponent solutions. Met. Mat. Trans. 32A, 1355–1360.
Pelton, A.D., Chartrand, P., 2001b. The modified quasichemical model IV – two sublattice quadruplet approximation. Met Mat. Trans. 32A, 1409–1416.
Pelton, A.D., Degterov, S.A., Eriksson, G., Robelin, C., Dessureault, Y., 2000. The modified quasichemical model I binary solutions. Met. Mat. Trans. 31B, 651–660.
Pelton, A.D., Schmalzried, H., 1973. Metall. Trans. 4, 1395–1403.
Pelton, A.D., Thompson, W.T., 1975. Prog. Solid State Chem. 10 (3), 119.
Prince, A., 1966. Alloy Phase Equilibria. Elsevier, Amsterdam.
Rhines, F.N., 1956. Phase Diagrams in Metallurgy. McGraw-Hill, New York.
Roos, G.D., 1916. Z. Anorg. Chem. 94, 329.
Schreinemakers, F. A. H., 1915. Proc. K. Akad. Wetenschappen. Amsterdam (Section of Sciences) 18,116.
SGTE group 1999–2009, (Ed.), Lehrstuhl für Werkstoffchemie, RWTH, Aachen, Thermodynamic Properties of Inorganic Materials, Landolt-Börnstein Group IV, vol. 19. Springer, Berlin.
Turchi, P.E., Abrikosov, I.A., Burton, B., Fries, S.G., Grimvall, G., Kaufman, L., Korzhavyi, P., Manga, V.R., Ohno, M., Pisch, A., Scott, A., Zhang, W., 2007. Interface between quantum-mechanical-based approaches, experiments, and CALPHAD methodology. Calphad J. 31, 4–27.
Van Laar, J.J., 1908. Z. Phys. Chem. 63, 216, 64, 257.
Villars, R., Prince, A., Okamoto, H., 1995. Handbook of Ternary Alloy Phase Diagrams. Am. Soc. Metals, Metals Park, OH.
Weeks, J. R., Davies, H. A., 1964. AEC Report, Conf. 660712–1, BNL-10372.

List of Websites

American Ceramic Society/NIST, phase.ceramics.org
American Society for Metals, alloy phase diagram center, www1.asminternational.org/asmenterprise/apd/
FactSage, Montreal, www.factsage.com
NPL-MTDATA, www.npl.co.uk/advancedmaterials/measurement-techniques/modelling/mtdata
Pandat, www.computherm.com/pandat.html
SGTE, Scientific Group Thermodata Europe, www.sgte.org
Thermocalc, Stockholm, www.thermocalc.com

Biography

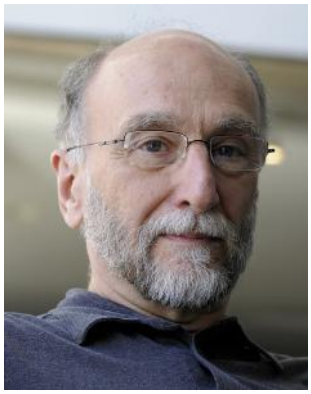

Arthur D. Pelton is Professor Emeritus in the Dep't.of Chemical Engineering and co-director of the Center for Computational Thermochemistry (CRCT) at the Ecole Polytechnique in Montreal, Quebec, Canada.

Dr. Pelton received his undergraduate and graduate degrees from the Dep't. of Metallurgy and Materials Science at the University of Toronto (PhD in 1970). Following post-doctoral studies at the Technical University in Clausthal, Germany and at MIT, he joined the faculty of the Ecole Polytechnique in the Dep't. of Materials Engineering in 1973. Dr. Pelton has co-authored over 250 technical papers and 14 book chapters. He is a Fellow of the Royal Society of Canada, the Canadian Academy of Engineering and of ASM. He is a recipient of the J. Willard Gibbs Phase Equilibria Award from ASM, the Hume-Rothery Prize for work in phase equilibria from the Institute of Metals, UK, and the Gibbs Triangle Award of Calphad. His primary field of interest is chemical thermodynamics in materials science. He is a co-founder of the FactSage thermodynamic database computing system.